The Search for High-Frequency Gravitational Waves with a Modified Axion Detector

by

Kaliroë Mabelle West Pappas

B.S., University of Illinois at Urbana-Champaign (2018)

Submitted to the Department of Physics
in partial fulfillment of the requirements for the degree of

Doctor of Philosophy in Physics

at the

MASSACHUSETTS INSTITUTE OF TECHNOLOGY

September 2024

©2024 Kaliroe M. W. Pappas. The author hereby grants to MIT a nonexclusive, worldwide, irrevocable, royalty-free license to exercise any and all rights under copyright, including to reproduce, preserve, distribute and publicly display copies of the thesis, or release the thesis under an open-access license.

Author .....
Kaliroë Mabelle West Pappas
Department of Physics
August 16, 2024

Certified by .....
Lindley Winslow
Professor of Physics, Associate Department Head
Thesis Supervisor

Accepted by .....
Lindley Winslow
Professor of Physics, Associate Department Head

The Search for High-Frequency Gravitational Waves with a Modified Axion Detector

by

Kaliroë Mabelle West Pappas

Submitted to the Department of Physics
on August 16, 2024, in partial fulfillment of the
requirements for the degree of
Doctor of Philosophy in Physics

Abstract

ABRACADABRA-10cm has had great success as a lumped-element axion dark matter pathfinder experiment, with two published axion searches and an extensive background investigation. Now, using the electrodynamics of gravitational waves and a simple change of pickup structures, we are using the ABRACADABRA detector to search for high-frequency gravitational waves in the kHz to MHz range. These higher frequencies may indicate signs of in-spiraling primordial black holes, or other beyond the standard model phenomena. With careful calibration used to distinguish between the two signals, we introduce the first simultaneous search for both axions and gravitational waves using a lumped-element axion detector. In this thesis I will present on the high-frequency cryogenic ABRACADABRA-10cm detector, the background investigations of the detector and the design and first data from the ABRACADABRA-10cm high-frequency gravitational wave search.

Thesis Supervisor: Lindley Winslow
Title: Professor of Physics, Associate Department Head

Acknowledgments

I would like to thank my advisor Lindley Winslow, for teaching me not only how to do good science but also how run an experiment at every level. I would also like to thank Jon Ouellet for helping me to hone my experimental instincts and teaching me how to ask good questions. Thank you to Reyco Henning for teaching me how to think critically about experimental designs and how to just plain get things to work. Thank you to both my office mates Jessica Fry and Chiara Salemi for being amazing scientist and good friends, much of this work benefited greatly from their contributions. Thank you to my academic twin Daniel Mayer and my academic advisor Christoph Paus, who both helped me at many crossroads and supported me throughout the whole PhD experience. Thank you to my collaborators in both theory and experiment all over the world, for meeting at odd times but still offering the most critical insight. Thank you to all the undergrads that worked with me throughout the years, I learned as much from you as you hopefully did from me. And finally, I'd like to thank my friends and family, work-life balance is difficult in graduate school but all of you made it worth the effort.

Contents

List of Figures

List of Tables

Chapter 1

Introduction

There are many ways to romanticize the science we do, from looking to the stars to pondering the inner workings of the smallest particles in front of a chalkboard. But the truth of it, at least for me, is idle curiosity and the inability to let something go. Why? That's the unanswerable question of the universe. As physicists we never grow out of that childish questioning, we just arm ourselves with the tools to go out and find the answer for ourselves.

There are several open questions in physics: where is all the mass and energy in the universe? What is the neutrino mass? Why does particle physics have a different expectation value for the cosmological constant as compared inference from cosmology? Why is there more matter than antimatter? Why is there no CP violation in the QCD Lagrangian? And many more. This thesis aims to discuss two of these open questions: what happened to the CP violation in QCD, and what is the majority of the mass in the universe?

The problem of CP violation in QCD is explored in Chapter 2, the core issue falls into the category of a fine-tuning problem. The concept of a fine-tuning problem is a question of unbelievable odds. If someone had launched a ball off the empire state building and it landed perfectly balanced on the tip of the Statue of Liberty's torch, would it be impossible? Maybe not, but watching the video you would assume there was more than likely foul play involved. As physicists we are skeptics, luck has no identifiable force carrier.

The first half of Chapter 3 explores the missing matter in the universe, how we know it's missing and what we are doing to try and find it. We call the missing mass "dark matter" since it does not directly interact with photons, and we have so far not been able to observe it directly. Dark matter and dark energy (the missing energy in the universe which drives expansion) make up around 95% of the universe, with visible matter making up the remaining 5%. The second half of Chapter 3 is on gravitational waves, ripples in the fabric of spacetime which propagate at the speed of light, and how we can detect them in different frequency ranges.

Chapter 4 is a characterization of the ABRACADABRA-10cm detector, which was

originally built to detect the axion, a dark matter particle candidate, and Chapter 5 describes the analysis methods used in the first two results of ABRACADABRA-10cm along with a discussion of noise in the detector. Chapter 6 is on the modification of ABRACADABRA-10cm for the detection of high-frequency gravitational waves, relating directly to the title of this thesis.

Chapter 2

The Standard Model and What is Missing

The standard model (SM) is governed by three major symmetries, charge, parity and time. Through experiment we have proven that none of these symmetries are conserved alone. The symmetries are additionally not conserved in pairs, the only symmetric conservation that has not been disproven thus far is the three symmetries together as CPT symmetry. CP violation has been observed in the weak sector, the forces that govern nuclear interactions, and is expected in the strong sector, the forces that hold protons and neutrons together. However, there has been no CP violation observed in the strong sector, contrary to expectation. Peccei-Quinn (PQ) symmetry was created to solve the strong CP problem, and as a consequence the resulting field quanta of the broken symmetry, the axion, can also be a solution to the missing matter in the universe.

This chapter explains the strong CP problem and a possible solution with PQ symmetry breaking, followed by a discussion of the resulting axion and detection methods for finding the axion.

2.1 Strong CP Problem

The Lagrangian which describes quantum chromodynamics (QCD) has a CP violating term that is a function of $\bar{\theta}$,

$$\mathcal{L}_{\bar{\theta}} = -\bar{\theta}\frac{\alpha_s}{8\pi}G\tilde{G} \tag{2.1}$$

where α_s is the strong coupling constant, and G and $\tilde{G}$ are the gluon color field strength tensor and its dual. $\bar{\theta}$ is the effective θ parameter (the phase parameter of the QCD vacuum) after diagonalizing the quark masses,

$$\bar{\theta} = |\theta + \arg(\det(M_q))|. \tag{2.2}$$

$\bar{\theta}$ has the freedom to take a value anywhere from $-\pi$ to π, therefore it is expected to be roughly on the order of 1. However, if we look at measurements of the neutron electric dipole moment (EDM), we find $\bar{\theta}$ is quite small [1].

The neutron dipole moment is a function of $\bar{\theta}$,

$$d_n \simeq \frac{e\,\bar{\theta}\,m_q}{m_N^2}. \tag{2.3}$$

The coefficients of the EDM come out to around 10^{-16}, and recent measurements of the neutron EDM have given it an upper limit of 1.8×10^{-26} [eV cm] [2]. Solving for $\bar{\theta}$, we find that it is approximately less than or equal to 10^{-10}, which is significantly less than a number on the order of one.

Aside on the neutron electric dipole moment

The neutron EDM violates parity and time reversal symmetry, meaning it does not flip direction under a time reversal transformation, while the spin and the magnetic dipole moment (MDM) do flip direction. The MDM is a pseudo-vector, so it will not change sign under parity, but the EDM is a vector, so it does change sign. Time reversal symmetry is violated by the neutron EDM as a result of the construction of the EDM, which is a simple distribution of charges within the neutron. A violation of time reversal symmetry is equivalent to CP symmetry violation, therefore by construction an observation of the neutron EDM would be an observation of CP violation in QCD.

There have been many experiments which have placed limits on the neutron EDM, the Paul Scherrer Institute used ultra-cold neutrons (UCN) with Ramsey's method of separating oscillating fields to achieve their limit on the neutron EDM quoted above. To find their limit, they first polarized their UCNs and measured the spin of those UCNs, and then selected a spin in the z-direction. Using ^{199}Hg as a co-magnetometer, next they rotated the spin to the x direction ("$\pi/2$ flip"). The spins were allowed to precess for time $T = 180$s at a frequency given by the Larmor precession frequency which would be affected by the presences of a permanent EDM,

$$\hbar f_n = \frac{1}{\pi}|\mu_n \overrightarrow{B_0} + d_n \overrightarrow{E}|. \tag{2.4}$$

Where $|\overrightarrow{B_0}| = 1036$ nT is the collinear magnetic field, μ_n is the MDM, d_n is the EDM and $|\overrightarrow{E}| = 11$ kV/cm is the change of polarity of the electric field. Finally the spins were rotated back to the z direction and measured [2].

From limits on the neutron EDM, we can see the CP violating term in the QCD Lagrangian is essentially zero. We call a result this coincidentally precise a fine-tuning problem, and we refer to this particular fine-tuning problem as the strong CP problem.

2.1.1 PQ Symmetry Breaking

To solve the strong CP problem, Roberto Peccei and Helen Quinn introduced an additional global chiral U(1) symmetry, $U(1)_{PQ}$ [3].

We start with a field in a potential that has a U(1) symmetry. We then go through the PQ phase transition which turns the potential into a wine-bottle potential as a results of spontaneous symmetry breaking. The spontaneously broken $U(1)_{PQ}$ symmetry creates a new field which corresponds to the angular degree of freedom, moving the field around the bottom of the wine bottle potential.

If we assume that the new field ϕ_a, interacts with the SM through a term that looks like

$$\mathcal{L} = \frac{\phi_a}{f_a}\frac{\alpha_s}{4\pi}G\tilde{G}, \tag{2.5}$$

with f_a as the decay constant, then interactions with the gluon fields will tip the wine bottle potential, explicitly breaking the symmetry and creating a minimum at $\bar{\theta}$. The field will oscillate about the minimum at $\bar{\theta}$, and the coefficient in front of the strong CP violating Lagrangian will be driven to (or time averaged to) zero,

$$\mathcal{L} = \left(\frac{\phi_a}{f_a} - \bar{\theta}\right)\frac{\alpha_s}{8\pi}G\tilde{G}. \tag{2.6}$$

The oscillations of the field are the result of a misalignment of the initial field with the minimum of the potential [4]. The resulting pseudo-Nambu-Goldstone boson from the spontaneous symmetry breaking is massive as a result of instanton effects which create the non-zero vacuum expectation value and are the cause of that spontaneous symmetry breaking. That massive particle is called the "axion" [5, 6].

The timing of the PQ symmetry breaking poses constraints on the axion decay constant. The ratio ϕ_a/f_a is approximately constant over scales smaller than the horizon size, the length scale over which particles/events are causally connected. If PQ symmetry breaks before or during inflation, the size of causally connected region is much greater (see Chapter 3 for more details on inflation) and f_a is allowed to take a much larger range of values. These pre-inflationary axions can have decay constants ranging to and past the grand unification (GUT) scale, resulting in low-mass axions which can constitute wave-like dark matter (DM) [7].

The vacuum expectation value of the scalar fields carrying PQ charge introduced by the axion field are expected to be on a scale much larger than the weak scale. There are two main theories for the QCD axion which explain these high vacuum expectation values, the Kim [8] and Shifman, Vainshtein and Zakharov [9] (KSVZ) model and the Dine, Fischler and Srednicki [10] and Zhitnishy [11] (DFSZ) model. The KSVZ model introduces two fields carrying PQ charge, a scalar field on the scale of f_a and a massive quark with $M_Q \sim f_a$. The DFSZ model is a grand unification model with ordinary quarks and leptons carrying PQ charge, and requires at least two Higgs doublets [1, 12].

A particle is only called an axion if that particle results from the PQ symmetry breaking which solves the strong-CP problem. However, there is a larger class of particles with similar characteristics to the axion which we call axion-like particles (ALPs). Many versions of string theory produce ALPs, and they have the similar couplings to the SM as the axion, which means they can be searched for using the same methods. Axions and ALPs are very promising particles, not only because the axion could solve the strong CP problem, but also because an axion or ALP could constitute DM. DM and axions/ALPs in the context of DM are explored in more detail in Chapter 3. Throughout the following chapters the term axion is often broadly applied to axions and ALPs, when it is important a distinction should be made ALPs are called by name and the true axion is referred to as the QCD axion.

2.2 The Axion

The axion is a pseudo-scalar particle, the implication being that the axion is spin-0 and does not change sign under parity transformations. The axion gets its mass by the misalignment mechanism, under which oscillating fields generate massive particles. The axion mass is found from diagonalizing the 4×4 squared mass matrix of the four Goldstone Bosons, and can be approximated as

$$m_a \approx \frac{f_\pi m_\pi}{f_a} = 5.691(51) \left(\frac{10^9 \text{GeV}}{f_a} \right), \tag{2.7}$$

where m_π is the pion mass and f_π is the pion decay constant [5, 12].

To understand axion interactions with the SM we look at the effective axion Lagrangian,

$$\mathcal{L} \supset \frac{g_s^2}{32\pi^2} \frac{\phi_a}{f_a} G_{\mu\nu} \widetilde{G}^{\mu\nu} + \frac{C_{a\gamma\gamma} \alpha_{\text{EM}}}{2\pi f_a} \frac{\phi_a F \widetilde{F}}{4} + \frac{C_{aee}}{2f_a} (\partial_\mu \phi_a) \bar{e} \gamma^\mu \gamma_5 e + \frac{C_{aqq}}{2f_a} (\partial_\mu \phi_a) \bar{q} \gamma^\mu \gamma_5 q - \frac{1}{2} m_a^2 \phi_a^2, \tag{2.8}$$

where the terms in order are the axion coupling to gluons, photons, electrons, quarks and the axion mass term.

2.2.1 Axion electrodynamics

The axion interacts with many SM particles, but the most commonly used interaction for detection is the two-photon interaction. This vertex of an axion converting to two photons is a simplification of a more complicated diagram with a loop and the two photons emitting from vertices on the loop as seen in Figure 2-1. The contents of the

loop are dependent on the axion model, for example, the KSVZ model depicts heavy quarks as the loop moderators.

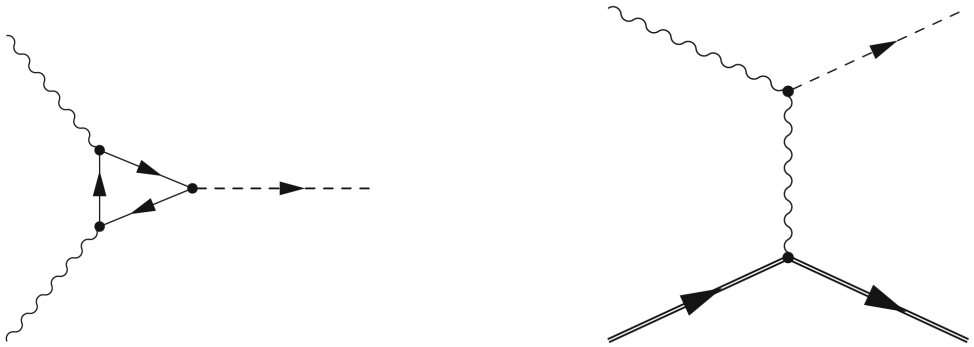

(a) (b)

Figure 2-1: Reproduced from [1]. Left: axion interaction with two photons mitigated by a model-dependent loop. Right: Primakoff effect of an axion converting to a photon in the presents of a Coulomb field of a charged particle.

The Lagrangian for the two-photon interaction is given by

$$\mathcal{L}_{a\gamma\gamma} = \frac{C_{a\gamma\gamma}\alpha_{\rm EM}}{8\pi f_a}\phi_a F\tilde{F} = \frac{g_{a\gamma\gamma}}{4}\phi_a F\tilde{F}, \tag{2.9}$$

where F and $\tilde{F}$ are the electromagnetic field-strength tensor and its dual, and $g_{a\gamma\gamma}$ is the axion coupling constant to two photons which is given by

$$g_{a\gamma\gamma} = \frac{\alpha_{\rm EM}}{2\pi f_a}\left(\frac{E}{N} - 1.92(4)\right)[\text{GeV}^{-2}]. \tag{2.10}$$

Here E and N are the electromagnetic and color anomalies of the axion axial current, their values are determined by the model use, with DFSZ having $E/N = 8/3$ and KSVZ having $E/N = 0$ for an electrically neutral massive quark [12].

The two-photon Lagrangian can be re-written in terms of electric and magnetic fields,

$$\mathcal{L} = g_{a\gamma\gamma}\phi_a \mathbf{E}\cdot\mathbf{B}. \tag{2.11}$$

The coupling of the axion field to the electric and magnetic fields modifies Maxwell's equations to include the axion field. Specifically, we can look at Ampere's law,

$$\nabla\times\mathbf{B} = \frac{dE}{dt} = J_{\rm eff}, \tag{2.12}$$

which is modified by the presence of an axion to include new terms proportional to $g_{a\gamma\gamma}$,

$$\nabla \times \mathbf{B} = \frac{dE}{dt} - g_{a\gamma\gamma}(\mathbf{E} \times \nabla\phi_a - \frac{d\phi_a}{dt}\mathbf{B}) = J_{\text{eff}}. \tag{2.13}$$

In the remaining Maxwell's equations, the divergence of $\mathbf{B}$ is still zero, and the curl of the electric field is still the negative derivative of the magnetic field, but the divergence of the electric field is changed,

$$\nabla \cdot \mathbf{E} = \rho - g_{a\gamma\gamma}\mathbf{B}\nabla\phi_a. \tag{2.14}$$

Note equations (1-13) and (1-14) are dependent on the gradient of the axion field, which is negligible. The axion's de Broglie wavelength is about 3 orders of magnitude larger than the oscillation wavelength, and thus the spatial gradient terms are suppressed [13].

2.2.2 Axion detection

There are many different methods used to search for the axion using the two-photon interaction, three of the most well-known are cavity searches, solar axion searches and light-shining through walls searches. In recent years a new method of using a lumped-element method has gained traction. Figure 2-2 is a diagram of the major current and upcoming axion experiments and the axion characteristics which correspond to their search range.

Cavity searches

Pierre Sikivie was the first to suggest the "invisible" axion could be searched for. This "invisible" axion existed in energy ranges below what could be seem in beam dump experiments or other existing experiments, Sikivie proposed a new method of resonantly converting the axions to photons in an electromagnetic cavity at a frequency proportional to the axion mass in new experiments he called "axion haloscopes" [15]. The full axion mass is converted into photons with a frequency

$$\omega_a = E_a = m_a + \frac{1}{2}m_a\nu^2 \approx m_a\left(1 + \mathcal{O}(10^{-6})\right), \tag{2.15}$$

for the energy of an axion E_a traveling at velocity ν, for a cold DM axion this is the velocity of the standard halo model (SHM) [16]. In a resonant cavity the power of the conversion of axions to photons is

$$P_a = g_{a\gamma\gamma}^2 V B_0^2 \rho_a C_{lmn} \frac{1}{m_a} \min[Q_L, Q_a], \tag{2.16}$$

where V is the volume of the cavity, B_0 the magnetic field in the cavity, ρ_a is the local density of axions, C_{lmn} is the form factor of the transverse magnetic (TM_{lmn}) mode of the cavity, and Q_L and Q_a are the loaded quality factor of the cavity and

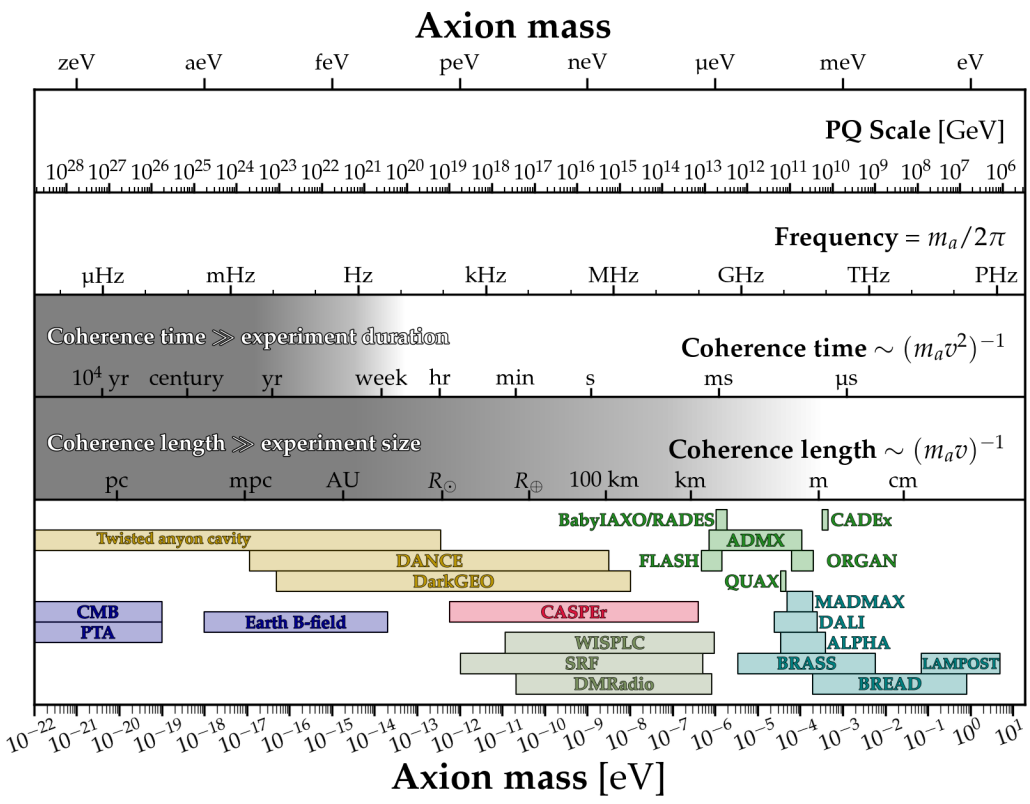

Figure 2-2: Reproduced from [14]

the quality factor of the axion signal respectively [17, 18, 15, 1]. Cylindrical cavities are the most commonly used for axion detection and have the largest form factor for the TM_{010} mode.

Cavities are built with resonant frequencies matching that of the axion mass of interest, with tuning rods which could be used to adjust the resonant frequency and broaden the searchable mass range. The signal-to-noise ratio (SNR) for cavity experiments is given by the Dicke radiometer equation

$$\text{SNR} = \frac{P_a}{\bar{P}_N}\sqrt{Bt} = \frac{P_a}{k_B T_S}\sqrt{\frac{t}{B}}, \tag{2.17}$$

where $\bar{P}_N = k_B T_S$ is the average noise power for the total system noise temperature T_S, B is the bandwidth of the axion signal, and t is the total signal integration time [19, 1]. Many experiments have successfully used this cavity technique to set limits down to the QDC axion, with ADMX reaching the DFSZ limit for axions of mass $2.66 - 3.31$ μeV [20]. Figure 2-3 is a subsection of the axion-to-two-photon parameter space focusing on the cavity experiments. These cavity searches are used primarily to search for DM axions, meaning they source their axions from the SHM of the Milky way.

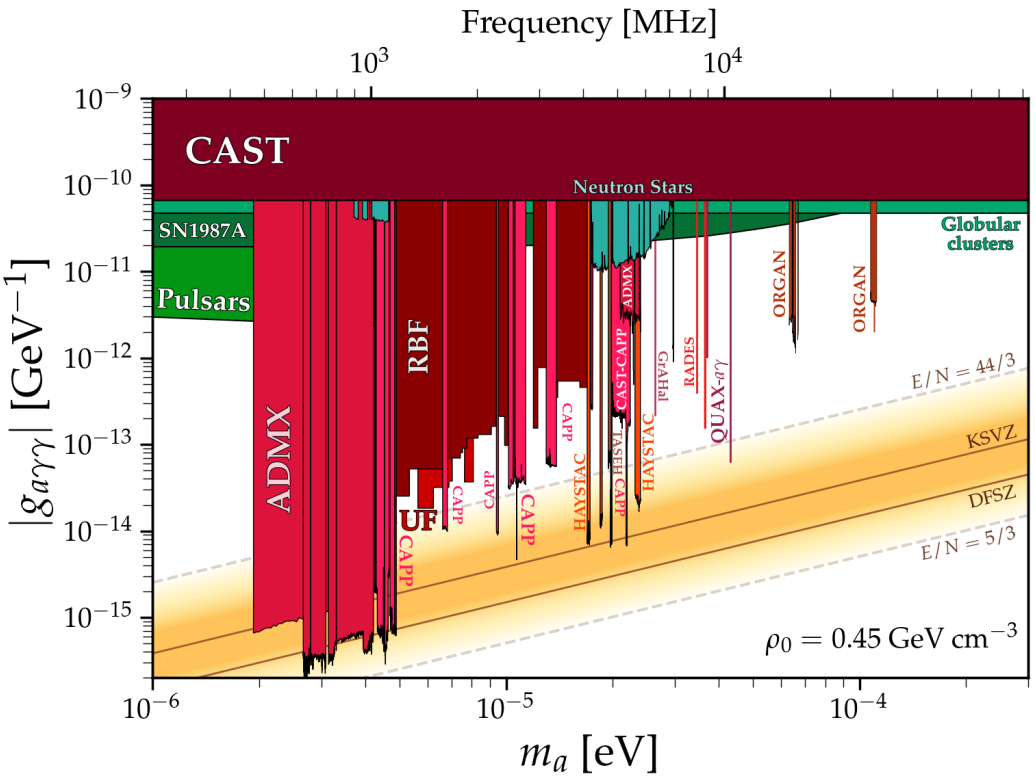

Figure 2-3: Reproduced from [14]. A subsection of the axion-photon coupling limits for cavity searches in radio frequencies.

Solar-axion searches

Axions are produced in the Sun through the Primakoff process, in which an axion in the electromagnetic field of the Sun's plasma is converted to a photon. Axion luminosity in the Sun is given by

$$L_a = g_{10}^2 \times 1.85 \times 10^{-3} L_\odot \qquad g_{10} = |g_{a\gamma\gamma}| \times 10^{10}\text{GeV}, \tag{2.18}$$

which was fixed by the results from the Solar Neutrino Observatory (SNO) and the standard solar model to $L_a \lesssim 0.10 L_\odot$ [12, 21]. The flux of these solar axions on Earth was found to be

$$\frac{d\Phi_a}{dE} = \frac{6.0 \cdot 10^{10}}{\text{cm}^2\text{sec keV}} \left(\frac{g_{a\gamma\gamma}}{10^{-10}\text{GeV}^{-1}}\right)^2 \left(\frac{E}{\text{keV}}\right)^{2.481} \exp\left(-\frac{E}{1.205\text{keV}}\right) \tag{2.19}$$

by [22]. Sivikie suggested in 1983 that these solar axions could be searched for directly with a similar method as the DM axion search with cavities, converting the solar axions into photons for measurement with the use of a magnetic field. He dubbed

these detectors "axion helioscopes" [15]. For these helioscopes the number of photons measured in the detector is estimated to be

$$N = \int \frac{d\Phi_a}{dE} P_{a\to\gamma}\, S\, t\, dE, \tag{2.20}$$

where $P_{a\to\gamma}$ is the conversion probability of an axion to convert to a photon in the magnetic field of the detector, S is area of the magnetic bore and t is the total measurement time. For a vacuum magnetic field volume,

$$P_{a\to\gamma} = \left(\frac{B g_{a\gamma\gamma}}{2}\right)^2 2L^2 \frac{1-\cos(qL)}{(qL)^2} \tag{2.21}$$

with magnetic field strength B, magnetic field length L and longitudinal momentum transfer $q = m_a^2/2E_\gamma$. $P_{a\to\gamma}$ is only at a maximum for an in-phase axion and photon, adding the constraint $ql < \pi$. From this constraint and equations (1.20) and (1.21), it can be seen that the number of photons measured are limited by the mass of the axion. However, the detectable mass can be extended with the use of a mediating gas giving the photon an effective mass $m_\gamma = \omega_{plasma}$, and the momentum transfer is now

$$q = \left|\frac{m_\gamma^2 - m_a^2}{2E_a}\right|. \tag{2.22}$$

With the phase constraints the mass range of the detectable axion is given by

$$\sqrt{m_\gamma^2 - \frac{2\pi E_a}{L}} < m_a < \sqrt{m_\gamma^2 + \frac{2\pi E_a}{L}} \tag{2.23}$$

for a gas-filled magnetic volume [1, 12]. As a result of this range in detectable axion masses, the helioscope experiments are able to set limits over a large spectrum of masses, however a confirmed measurement from a helioscope experiment would not be able to identify the exact mass of the solar axion found, only the value of the coupling constant $g_{a\gamma\gamma}$.

There have been many helioscope experiments which have set world-leading limits, such as the CERN Axion Solar Telescope (CAST) experiment, a portion of the limits CAST has set can be seen in Figure 2-3. The CAST experiment uses a decommissioned LHC dipole magnet mounted to a movable platform to track the path of the Sun and increase the measurement time t which increases the expected number of photons as seen in equation (2.20). The chamber of the magnet is filled with a pressurized helium gas and x-ray optics to focus the signal. CAST has had multiple searches with different gases and pressures to extend their detection range, resulting in a limit of $|g_{a\gamma\gamma}| < 6.6 \times 10^{-11}\,\mathrm{GeV}^{-1}$ at a 95% confidence level over ALP masses above 0.02 eV [23, 24]. The International Axion Observatory (IAXO) will set the strongest limits from an axion helioscope yet, with the goal to set limits 4-5 times

stronger than the CAST limits [25]. In addition to the helioscopes, solar axions can be searched for indirectly from stellar evolution observations (see Chapter 3), as axions would be produced most stellar objects.

Light-shining-through-walls searches

Axions originating from DM or produced in the Sun are inherently source-model dependent, however an axion created in the lab could be made without these source dependencies. The principle idea of these lab-production experiments is to convert photons into axions that can pass through an optically opaque obstacle then convert the axions back into photons to be detected [26]. These experiments are referred to as "light shining through walls" experiments.

In a light-shining-through-walls experiment, a polarized laser is used to generate the initial photons which are then converted to axions in a magnetic field with probability

$$P_{\gamma\to a} \propto \frac{1}{4}(g_{a\gamma\gamma}BL)^2\frac{1-\cos(qL)}{(qL)^2}. \tag{2.24}$$

Similarly to the axion helioscopes, here the coherence of the axion beam is constrained by $m_a^2L/2\omega \ll 2\pi$ for the energy of the photon ω over the length of the B field L [1, 12]. These axions are then converted back to photons with the same probability, resulting in a total probability of detection of

$$P_{\gamma\to a\to\gamma} = P_{\gamma\to a}^2. \tag{2.25}$$

The probability of detection is now suppressed by $g_{a\gamma\gamma}^4$, while solar axion and DM axion experiments are only suppressed by $g_{a\gamma\gamma}^2$. To increase the number of expected detection photons, these light-shining-through-walls experiments use high-powered lasers and optical Fabry-Perót (FP) cavities. The lasers and FP cavities can function on the production side, the rate of expected detection photon counts is directly proportional to the average power of the laser, and the FP cavity allows that laser to reflect back and forth coherently, with each pass through the magnetic field photons are converted to axions. The FP cavity uses partially reflective lenses, only letting through light at the resonance frequency of the cavity and can be used on both the production and detection side. On the detection side the FP cavity locks coherently to the FP cavity on the production side, and the total effect is an enhancement of $P_{\gamma\to a\to\gamma}$ by $\mathcal{F}\mathcal{F}'/\pi^2$, where $\mathcal{F}$ is the finesse of the production cavity and $\mathcal{F}'$ is the finesse of the detection cavity [27, 28, 29, 30, 12]. The light-shining-though-walls experimental setup can be seen in Figure 2-4, for both the simplest model and with FP cavities. The ALPS II experiment is using a 150 kW laser, 24 superconducting magnets and 122 m long FP cavities to search for laboratory ALPs, and they expect to have sensitivity down to $g_{a\gamma\gamma} = 2\times10^{-11}\text{GeV}^{-1}$ [1, 31, 16].

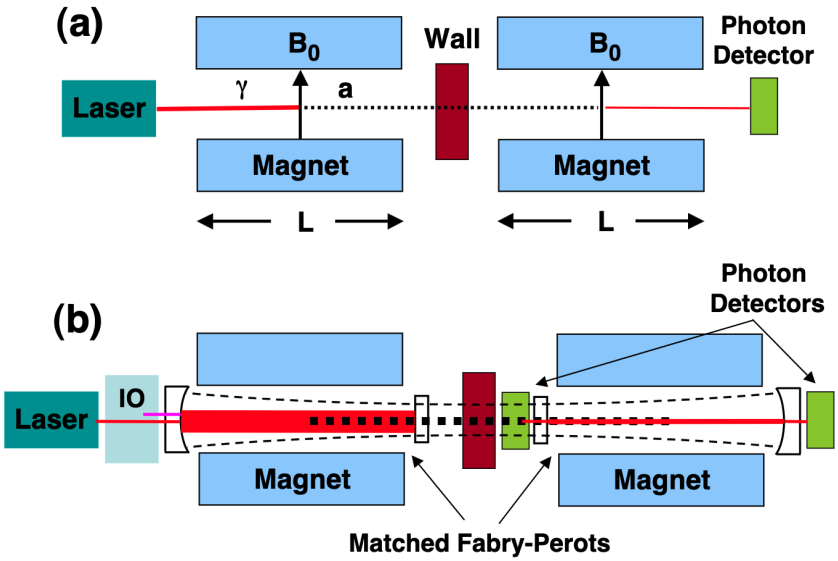

Figure 2-4: Reproduced from [27]. (a) is the some simple version of the light shining through walls detector, while (b) shows the experiment modified with FP cavities.

Lumped-element searches

For an axion of a smaller mass, entering the neV range, cavity searches become impractical. For axions in the mass range of 10^{-14} to 10^{-6} eV the Compton wavelength of the axion is much larger than the size of a practical detector, and we enter the magnetoquasistatic regime. In this regime the displacement current is small enough that we can ignore the time derivative of the electric field [32]. Starting from equation (2.14) and taking the spatial axion gradient to be effectively zero we can solve for the effective current,

$$J_{\text{eff}} = g_{a\gamma\gamma}\frac{d\phi_a}{dt}\mathbf{B}. \tag{2.26}$$

The axion field is given by

$$\phi_a = \frac{\sqrt{2\rho_{\text{DM}}}}{m_a}\sin(m_a\, t), \tag{2.27}$$

plugging the field into equation (2.26), the effective current is now

$$J_{\text{eff}} = g_{a\gamma\gamma}\sqrt{2\rho_{\text{DM}}}\cos(m_a\, t)\mathbf{B}. \tag{2.28}$$

To detect axions in this low-mass/long wavelength regime a lumped-element technique can be used. Lumped-element searches describe measuring the axion signal by coupling the axion current to circuit components like inductors and capacitors. Figure 2-5 shows the two basic circuit options for lumped-element detection, a broadband

and a resonant search. ABRACADABRA-10 cm was the first experiment to demonstrate the lumped-element technique with a toroidal magnet [33], and the SHAFT experiment demonstrated the implementation of the technique with ferromagnets [34]. There have been more experiments using the lumped-element method since the first ABRACADABRA-10cm run, and the DMRadio collaboration is constructing experiments to reach the QCD axion at GUT scales using a resonant lumped-element construction (see Appendix A). Chapters 4,5 and 6 focus on the ABRACADABRA-10cm experiment.

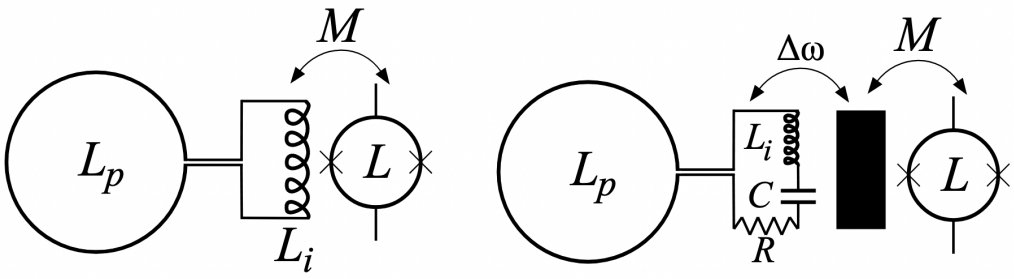

Figure 2-5: Reproduced from [35]. Right: broadband lumped-element circuit. Left: resonant lumped-element circuit.

The field of axions is relatively young, but has been picking up considerable traction in the last few decades. Novel techniques such using dish-antenna haloscopes by the BREAD collaboration [36] are being proposed and built, and the axion parameter space will be considerably better searched in the next few decades, hopefully resulting in a discovery.

Chapter 3

Dark Matter, the Universe and Gravitational Waves

Dark matter (DM) composes 85% of matter in the universe, yet its nature remains largely unknown. The strongest evidence for DM comes from astronomical and cosmological observations dating back to the 1930s. Zwicky observed in 1933 that galaxies in the Coma cluster were moving as if the clusters contained 10 times more mass than was observable [37]. Later, in the 1970s Vera Rubin's observations of galaxy rotation curves showed the radial velocity distribution in a spiral galaxy did not match calculations which were dependent on the mass of luminous matter contained within those galaxies [38]. Other evidence came from gravitational lensing [39], x-ray gases in galaxy clusters [40], the amplitude of peaks in the power spectrum of the cosmic microwave background (CMB) [41] and more. These observations lead scientists to believe there must be some matter that interacts gravitationally yet is otherwise unobservable in the universe.

The following chapter begins with evidence of DM in the formation of the present-day universe from the time of recombination to cluster and galaxy dynamics, which leads into a discussion of DM criteria and possible DM candidates. The last part of this chapter is on gravitational waves (GWs), production, sources and detection, for both GWs in the typical frequency range (below 10 kHz) and the high frequency range (above 10 kHz).

3.1 Evidence of Dark Matter

The evidence of DM can be seen throughout the history of the universe, with notable examples from the CMB, the formation of large-scale structures, velocity distribution in galaxy rotation curves and most recently observations of matter dynamics in the Bullet Cluster.

3.1.1 Recombination and the Formation of Large Scale Structures

Recombination

Recombination describes the time when the thermal energy of the universe exceeded the ionization potential of hydrogen. The minimum energy a photon needs to ionize hydrogen is 13.6 eV, as the universe expands and cools the interactions between hydrogen and photons at this critical energy decrease. At this point, the universe became fully ionized, characterized by 50 % of electrons are free/bound, and this time is referred to as "the surface of last scattering". Photons from the surface of last scattering make up the cosmic microwave background (CMB) and the temperature of the CMB has been measured today to be $T(0) = 2.73$ K. Using this temperature, the criteria for full ionization and the relationship between temperature and red shift, $T = T(0)(1 + z)$, we find the red shift for recombination to be $z = 1090$.

Formation of Large Scale Structures

Before Recombination, matter and radiation were coupled through Thompson scattering and pressure in the universe was dominated by radiation. After Recombination the universe behaved approximately as an ideal gas, and structure formation could begin. At the time of Recombination we can assume ideal conditions, with the universe as relatively "smooth" (as seen from the CMB), gravity behaving linearly before Recombination, and gravity behaving non-linearly after Recombination when the force of gravity is stronger than the expansion of the universe.

The age of the universe before Recombination was shorter than the sound crossing time in the matter-radiation plasma ($t_s = r/\nu_s$, with r as the distance and ν_s as the speed of sound), the implications being that if a sound wave cannot cross a cloud before it collapses then the pressure in that cloud cannot stabilize. This destabilization leads to perturbations of matter gravitationally collapsing and then expanding from excess pressure. The DM in the universe at that time does not face the same stabilization issues as it is mostly non-interactive with the matter and radiation, and DM is allowed to continuously collapse while the matter oscillates. After the universe has expanded and cooled enough for over-densities[1] to start to form, the densities oscillate until Recombination, when $t > t_s$, at which point matter is allowed to fall into gravitational potentials which were pre-made by DM. These oscillations are referred to as Baryon Acoustic Oscillations (BAO), and they form the peaks in the CMB. Signs of the BAO have also been observed in large-scale correlation functions over large regions of space [42].

While the exact nature of DM is unknown, the temperature of DM can be deduced from its clumping behavior and the formation of structures in the universe. There

[1] An over-density is defined as $\delta(\mathbf{x}) = \frac{\bar{\rho}(\mathbf{x})-\rho}{\bar{\rho}}$ where $\delta(0)$ marks the mean density.

are two main theories for structure formation: top-down and bottom-up. Top-down refers to large scale structures of smoothed-out matter forming first and establishing formations like clusters, with small scale structures such as galaxies and later stars forming later as a result of collapses in the matter densities. Bottom-up reverses the order, small scale structures first form, then clump into larger structures. The temperature of DM affects which scenario occurred [43].

It should be noted that here that the word "temperature" refers to the relative relationship between the temperature at which freeze-out in the early universe occurred and the mass of the particle, which affects the relativistic nature of that particle. Therefore, a "hot" DM candidate is relativistic, a "warm" DM candidate is semi-relativistic, and a "cold" DM candidate is non-relativistic. However, there are many DM models which were never in thermal equilibrium, and therefore their mass does not affect their velocity, but the same temperature terms are still used to describe their relativistic nature [12].

A hot DM candidate would smooth out structures and would not clump together as a result of its relativistic speed, which supports the top-down theory of structure formation, but simulations of hot DM fail to create all the observed small structures of the universe, such as satellite galaxies. A cold DM (CDM) candidate does clump, and therefore supports the bottom-up structure formation, CDM does face a few challenges which are addressed later in the text. Stuck in the middle, warm DM describes a candidate that is semi-relativistic and supports some in-between theory, warm DM struggles to reproduce small-scale structures and requires some model alterations. Figure 3-1 shows a simulation of structure formation with the inclusion of warm DM and of CDM, where it is clear the small structures are blurred in the warm DM model. Stars 10-14 billion years old have been observed in galaxies, while many clusters have been observed to be in the process of formation, suggesting a bottom-up approach and favoring CDM as the most likely candidate.

CMB

The CMB is characterized by the angular power spectrum. The sky is decomposed into spherical harmonics with

$$\frac{\Delta T}{T} = \sum_{l=0}^{\infty} \sum_{m=l}^{l} a_{lm} Y_{lm}(\theta, \phi). \tag{3.1}$$

The power for each multipole moment is given by

$$\mathcal{D}_l^{TT} = \frac{l(l+1)C_l}{2\pi} \tag{3.2}$$

where $C_l = \langle |a_{lm}|^2 \rangle$ and the units are given in μK^2. The TT in the superscript is in reference to the temperature-temperature power spectrum, as opposed to the

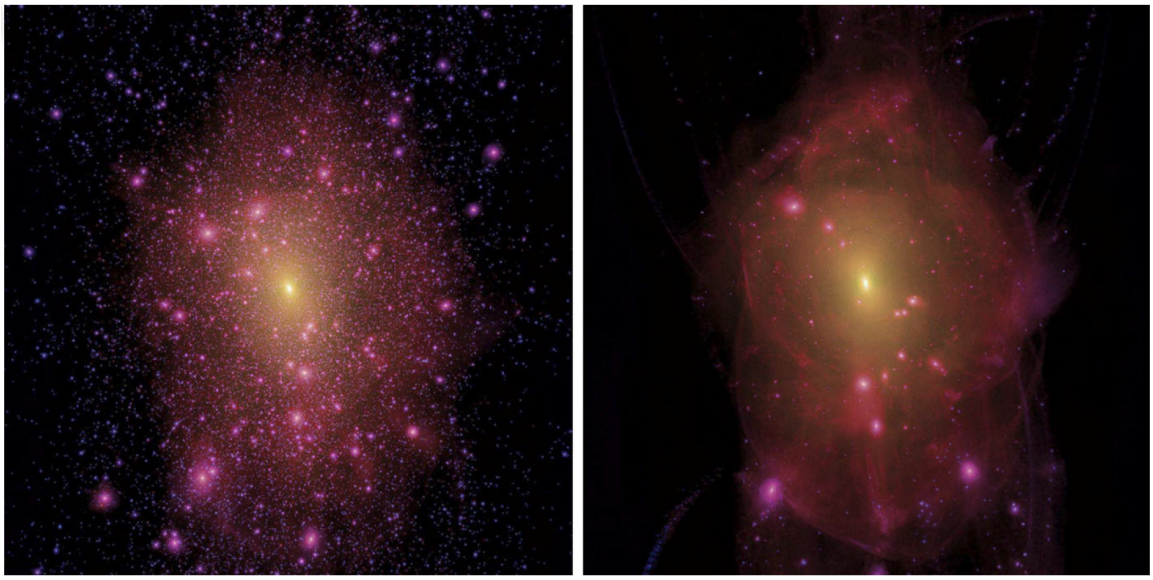

Figure 3-1: Reproduced from [44]. Simulation of structure formation with cold dark matter (left) and warm dark matter (right).

E-mode polarization (electric component of the polarization) power spectrum or the temperature-E-mode power spectrum. We look at temperature measurements that are in excess of the mean temperature to find the over-densities.

Each peak in the CMB power spectrum represents either maximum compression or maximum expansion when recombination occurs, alternating with the odd peaks as compression. As seen in Figure 3-2, the height of the first peak is an indicator of the total matter density Ω_m, the relative heights of the first and second peaks indicate the total baryon mass density Ω_b, the position of the first peak indicates the curvature of the universe Ω_k (the experimentally determined position indicates k = 0, a closed universe). The presents of DM can be seen in the difference between Ω_m and Ω_b, and in addition by the relative height of the first peak which is driven by baryon loading, more DM increases the baryon loading effects and raises the relative height of the third peak to the first two peaks.

The discovery and measurement of the CMB brought with it a few major puzzles. The first being an effect of how "smooth" the CMB is, i.e. homogeneous in temperature to 1 part in 10^5, but the size of the horizon [2] at the time of last scattering was much smaller than the universe, giving rise to the Horizon problem. Additionally, the CMB presents the issue of "flatness" which describes the fine-tuning problem of the conditions of a flat universe being met today, requiring the energy density to take a value very close to the critical density, where the critical density is the density needed for a flat universe. The ratio of density to critical density is closely tied to the expansion of the universe, and extrapolating back to the time of big bang nucle-

[2]The size of the horizon describes the largest distance that is causally connected by light.

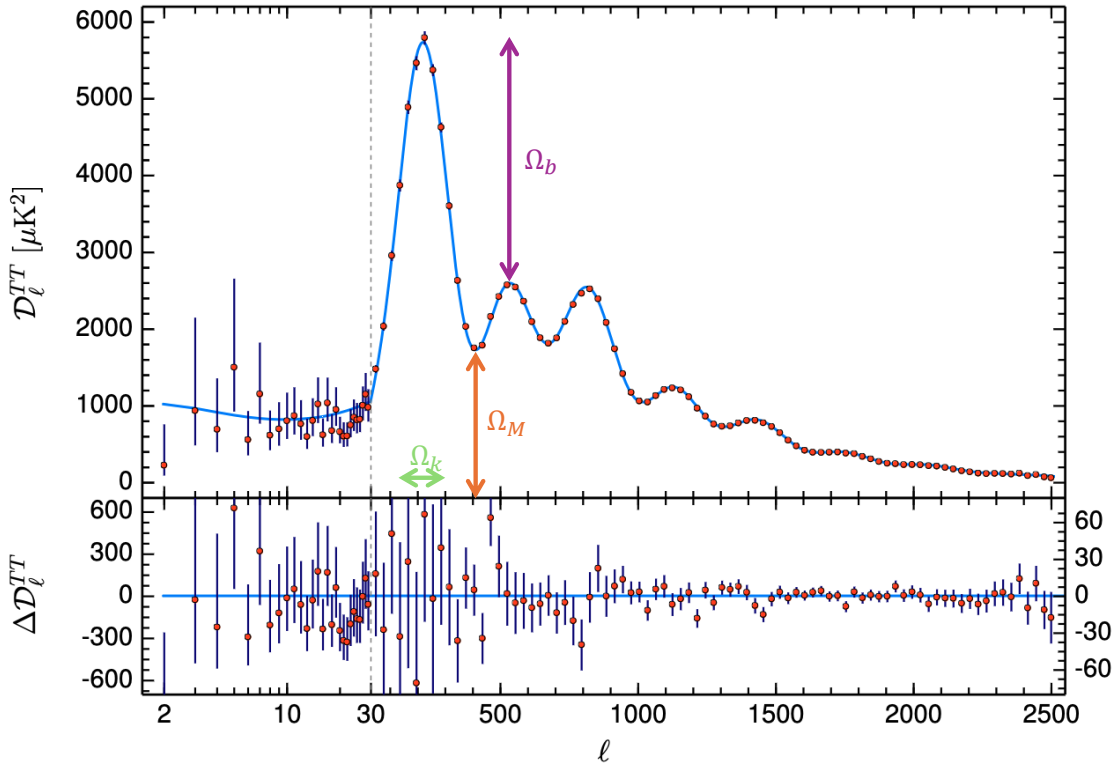

Figure 3-2: Adapted from [45]. The TT power spectrum with the indicators of the densities of mass, baryons and curvature marked in orange, purple and green respectively.

osynthesis necessitates that ratio to be $\rho_{\text{crit}}/\rho - 1 \approx 10^{-60}$, an extremely finely-tuned value. The last major puzzle posed by the CMB was the magnetic monopole, there is reason to believe that monopoles should have formed early in the universe, yet they are unobserved today. The theory of Inflation solves all three of these problems.

Inflation is the concept the universe underwent a period of rapid expansion shortly after the Big Bang. This rapid expansion would allow all points to have been causally connected just before it occurred, solving the Horizon problem, and the Flatness problem is solved by an asymptotical approach to flatness from the rapid expansion. The lack of magnetic monopole detection can also be explained if they were formed before Inflation and then became heavily diluted after the universe expanded [46]. Signs of inflation would be present in B-mode polarizations in the CMB caused by gravitational waves (GWs) from inflation, more on this signature in section 3.3.

3.1.2 Galaxy Rotation Curves

Galaxy rotation curves are generally the most reference evidence for DM. The concept is quite simple, from the estimated luminous mass in a galaxy the rotation speed of the

outer objects can be determined. However, observations showed that the outer objects in galaxies were traveling at far greater speeds than estimated, leading scientists to believe there had to be some sort of hidden mass in the galaxy that is more massive than the luminous matter and extends beyond the observed galaxy.

Vera Rubin and colleagues measured 21 spiral galaxies of varying masses (10^{10} to $2\times10^{12}M_{\odot}$) and luminosities (3×10^{9} to $2\times10^{11}L_{\odot}$) in 1978 and found the majority of the galaxies had rising velocities out to the furthest objects from the nuclei, and the largest galaxies had flat rotation curves. The lack of a falling rotation curve suggests that the majority of the mass must be contained past the outer-most measured object [38]. These observations also could have been indicative of a misunderstanding of gravity, leading to theories of modified Newtonian dynamics (MOND).

3.1.3 The Bullet Cluster

Analysis of 1E 0657-56, the Bullet Cluster, provided one of the strongest pieces of evidence for DM to-date. The Bullet Cluster is at a redshift of $z = 0.296$ and contains a pair of galaxy clusters which are in the process of merging, with the smaller of the two moving away at 4700 km/hr. X-ray detections observed the intra-cluster plasma slowed in the collision by ram pressure and the gas in the merger also slowed by the ram pressure[3], gases make up the majority of luminous mass in a cluster. The luminous mass was accounted for in the collision, and weak gravitational lensing was used to find the center of mass of each individual cluster. Weak gravitational lensing refers to the observation of the distortion of objects caused by a large mass between the observer and the objects [47]. They observed that the peaks of the gravitational potentials were ahead of the centers of luminous mass, as would be expected of a cluster dominated in mass by DM. The DM in a cluster is not slowed by the ram pressure of the plasma, and with minimal self-interactions the DM is essentially only affected by the gravity. The Bullet Cluster presents proof of DM that is independent of cosmological model parameters at high significance [48].

The analysis of the Bullet Cluster discredited may theories of MOND, as the trajectory of the center of masses of the two galaxy clusters suggests a particle-like DM candidate and are difficult to model with a modification to gravity. Many of the remaining MOND theories were mostly disproved with the discovery of GWs by the LIGO/Virgo collaborations in 2016, when it was verified that GWs travel at the speed of light [49].

[3]Ram pressure is the force exerted on a stable point contained in a fluid caused by the movement of the fluid.

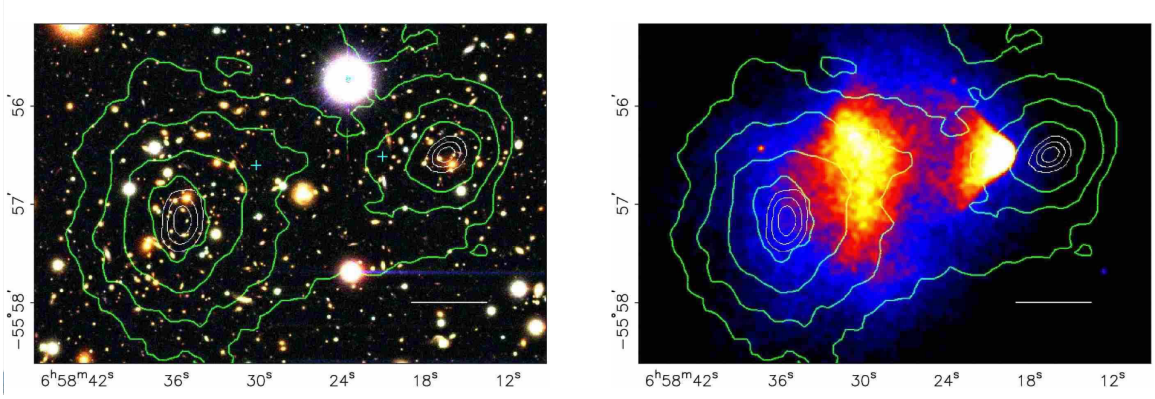

Figure 3-3: Reproduced from [48]. The image on the right is from the Magellan telescope of 1E 0657-56, and the image on the left is from the Chandra x-ray observatory. The green contour lines showing the weak gravitational lensing constrains on the gravitational potential.

3.2 Dark Matter Candidates

There are many theories of what could compose DM, from compact objects to sub-neV particles, yet there are common features all viable DM candidates must have. First, the candidate must be color charge and electric charge neutral, meaning DM cannot interact directly through the strong force or the electromagnetic (EM) force. Direct interactions with photons, the force carrier for the EM force, would show in astronomical observation, while direct interactions with gluons, the force carriers for the strong force, would show in the existence of exotic isotopes which are not observed. Additionally, if the DM particle were to carry charge, Recombination could be affected and the baryon acoustic peak structure in the CMB would be altered. Second, DM must have been created in the early universe before the transition from radiation domination to matter domination, to allow large scale structures to form. Regardless of the production mechanism, the DM candidate must produce in the correct relic abundance. Third, based on observations of the Milky Way Galaxy, DM must still be around today. Fourth, DM must have the ability to cluster in order to explain large- and small-scale structures in the universe. An inability to cluster leads to a more "fuzzy" universe, where galaxies do not group together to form the structures that are observed [43]. Finally, DM must be non-baryonic. Besides the obvious quality that if DM was baryonic it would interact with the standard model (SM) and thus be observable, DM being baryonic in nature would change the power spectrum of the CMB, leading to large fluctuations of the amplitudes of the peaks and very large CMB anisotropies [50].

While the CDM model is preferred to hot and warm DM models, it is also imperfect. There are three major issues with CDM that have arisen since it's conception: the cusp-core problem, the missing satellite problem, and the too-big-to-fail prob-

lem. The cusp-core problem describes the tension between how CDM is theorized to peak sharply in the radial center of the distribution of matter within a halo, and the observations of rotational velocity that show a flat constant core profile of the DM halo. To get around the cusp-core problem without changing to the warm DM model (which is flawed in and of itself) elastic scatting from small self-interactions can be added to the CDM model to smooth out the density profile of DM halos. The missing satellite problem states that from the clumping properties of CDM, it is expected that many satellite galaxies should have formed around large galaxies, specifically, the Milky Way galaxy should have somewhere between 50-200 satellite galaxies which were previously unobserved. SDSS and other surveys have found some of these satellite galaxies in their coverage of the sky, and it is likely that as the full sky is mapped the necessary number satellites will be found, lessening tension in the CDM model from the missing satellite problem. The last major issue with CDM is the too-big-to-fail problem, which describes CDM predictions of massive DM sub-halos which are not observed. Self-interacting DM can also pose as a solution to the too-big-to-fail problem[43].

There are many candidates for DM that fit the self-interacting CDM model, many are particle candidates though notably primordial black holes (PBHs) which are a non-particle candidate have gained traction in recent years.

3.2.1 Thermal Dark Matter: the WIMP

By far the most popular DM candidate in the last few decades has been the weakly interacting massive particle (WIMP). A WIMP refers to a very general class of thermal relics which only interact gravitationally and possibly through the weak force, but not through strong and EM forces [51]. WIMPs with mass greater than a keV are thermally produced at non-relativistic speeds and they can function as CDM, and many WIMP models contain self-interactions so the major of the issues of CDM are avoided.

As the early universe expanded and cooled, particles which were in thermal equilibrium of annihilation and production fell out of equilibrium to form relic abundances that can be seen today. This thermal mechanism is present for many of the SM particles. The Boltzmann equation is used to describe the change in number density of the thermal particles over time,

$$\frac{dn}{dt} = -3Hn - \langle \sigma_A v \rangle (n^2 - n_{eq}^2). \tag{3.3}$$

Here, H is the Hubble parameter, n is the number density, $\langle \sigma_A v \rangle$ is the thermally averaged annihilation cross section, and n_{eq} is the number density in equilibrium. For the case of WIMPs, $n_{eq}^2 \langle \sigma_A v \rangle$ describes the annihilation rate into SM particles, and $n^2 \langle \sigma_A v \rangle$ describes the formation of WIMPs from SM particles. The Boltzmann equation can be solved numerically at freeze out, which is defined to be when $n \langle \sigma_A v \rangle =$

H, to find the thermal relic density and the annihilation cross section. The so-called "WIMP miracle" refers to the convenient fact that WIMPs over a large mass range are naturally produced with the correct relic density to be all of DM. Another interesting outcome of the WIMP miracle is that the annihilation cross section of WIMPs is on the weak scale, with $\sigma_A v \propto g_{weak}^4/m_X^2$ [51].

WIMP parameters such as self-interaction rates and mass range can be constrained by astronomical observations such as the Bullet Cluster or large-scale structures. Finer constraints of WIMP parameters and potential direct measurements are searched for using direct detection. There are many different methods for WIMP detection such as beam-dump experiments or cosmic ray searches for WIMP signatures, but the most popular and well-funded searches are in nuclear recoils. A WIMP has no EM interactions, so a WIMP will elastically scatter off a nucleus of a atom and cause a nuclear recoil of which the energy could be measured. To perform these searches, a dense and very stable medium is needed, which is why the largest WIMP experiments use liquid Nobel gases as their detection medium, liquid xenon being the most prominent [52].

The WIMP parameter space has been constrained to such a high degree that experiments are now hitting what is known as the "neutrino floor" or more optimistically, the "neutrino fog" where DM recoils are difficult to distinguish from recoils from a neutrino background. While this may seem like a bleak ending for WIMPs it should be noted that any WIMP that can be found in a detector, either from nuclear recoil or collider experiment, is not model independent and changes in models could open new parameter space [53]. Additionally, the neutrino fog can be understood with careful directional searches and better understanding of the neutrino interactions.

The WIMP as a particle candidate is so far primarily constrained by experimental direct detection, and cosmological and astrophysical limits are much less strong by comparison. Figure 3-4 shows the experimental direct detection constraints on the WIMP and the neutrino fog for liquid xenon experiments.

3.2.2 Athermal Dark Matter: the Axion

As discussed in the previous chapter, axions are massive light bosons that are a viable candidate for DM. The axion has small interactions with the SM, they are produced athermally making them non-relativistic and a CDM candidate and they do not have self-interaction terms at tree-level. The non-tree-level self-interactions are important for DM evidence like the bullet cluster, where the luminous matter collided but the DM passed right through. If the axion had strong self-interaction terms, the axions in the Bullet Cluster would have been slowed and the centers of gravitational potential would have more closely matched the luminous matter.

The axion parameter space is still relatively open, with experimental direct-detection limits getting better each year and a wide range of strong astrophysical and cosmological limits. Even while holding the abundance constant, the addition of

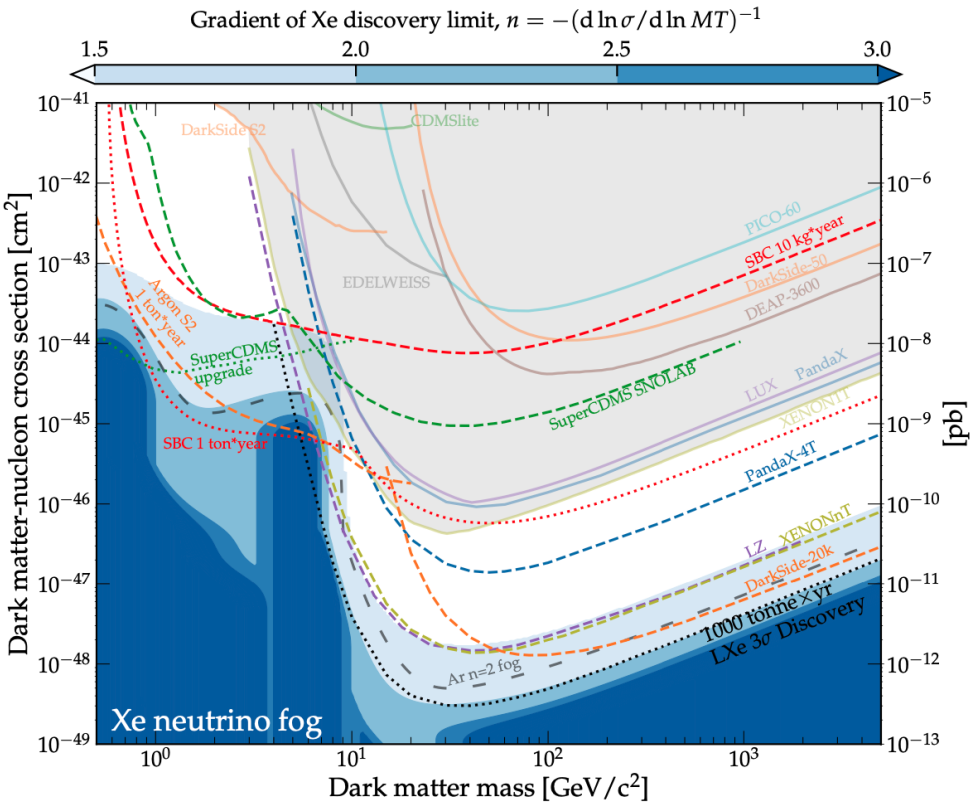

Figure 3-4: Reproduced from [54]. WIMP parameter space with liquid-xenon neutrino fog limits.

a light particle to the SM has the potential to highly affect astrophysics on many different scales. A few robust limits on axion parameter space from supernovae, Globular clusters and white dwarfs are explored below.

Supernova 1987A

During a core-collapse supernova (SN), it is expected that ALPs will be emitted via nucleon interactions and the Primakoff process, and limits can be placed on axion parameter space based on observations of SN 1987 A and the diffuse SN background. During SN 1987A, about two dozen neutrinos were detected from the SN by the Kamiokande II experiment over an 11 second interval [55] and the IMB experiment over a 6 second interval [56]. These neutrino detections closely matched models of core-collapse SN, establishing cooling limitations. In the nascent protoneutron star stage[4] of the SN, the neutrinos are trapped and escape on a timescale described

[4]The nascent protoneutron star stage occurs when the core of the star collapses to the point that the density has exceeded the saturation density and the core begins to bounce back.

by the diffusive neutrino energy transport. If ALPs are emitted through nucleon bremsstrahlung during the SN, the neutrino burst duration would shrink as the system cools faster, placing limits on the coupling constant g_{aNN} [1, 57]. ALPs would also be expected to form via the Primakoff process during the core expansion.

Additional signs of ALPs from SN 1987A would appear in the form of γ-rays, as ALPs produced in the SN would convert to photons in the magnetic field of the Milky Way and produce a γ-ray flash which would have been detectable for certain ALP couplings and masses. The ALPs form through the Primakoff process for this burst, giving a detection dependence on $g_{a\gamma\gamma}^4$ and an arrival time which would match with the SN neutrinos, ahead of the SM-SN γ-rays. Limits were placed on ALPs as a result of the lack of a γ-ray burst of $g_{a\gamma\gamma} \lesssim 5.3 \times 10^{-12}$ GeV^{-1} for $m_a \lesssim 4.4 \times 10^{-10}$ eV [58].

Extra-galactic supernovae (SNe) can also be analyzed for signs of axions in the form of prompt γ-ray bursts and the diffuse γ-ray background. In [59], 20 core-collapse SNe were examined with the assumption the Fermi Large Area Telescope would observe at least one SN. Without signs of γ-ray bursts characteristic of ALPs, they were able to place limits of $g_{a\gamma\gamma} \lesssim 2.6 \times 10^{-11}$ GeV^{-1} for $m_a \lesssim 3 \times 10^{-10}$ eV. The limits from extra-galactic γ-ray burst can be made stronger by the inclusion of ALP-nucleon coupling, to get $g_{a\gamma\gamma} \lesssim 6 \times 10^{-13}$ GeV^{-1} for $m_a \lesssim 10^{-11}$ eV [60]. The extra-galactic space is expected to also have remnants of ALP-created γ-rays from past SNe in the form of a diffuse background [61], which was used to constrain heavy ALPs down to $g_{a\gamma\gamma} \lesssim 5 \times 10^{-11}$ GeV^{-1} for $m_a \sim 5$ keV [60]

Globular Clusters

As a result of the non-interactive nature of the axion, axions are able to pass through optically opaque regions of stars, carrying energy away from the star through the Primakoff process. Throughout the life cycle of a main sequence star, a star composed originally of primarily hydrogen and helium, the star burns energy, expands, contracts, cools and heats. One part of the cycle that is of particular note from the prospective of axion production is during the red-giant phase when the star maintains a constant luminosity while continuously dropping in temperature. The effect is a horizontal line of the stellar population in the H-R diagram[5], and these stars are referred to as horizontal branch (HB) stars. The HB phase occurs once the star has burned hydrogen to the point the helium core is massive enough to begin helium burning. During helium burning the core of the star becomes less dense, allowing for more free photons and as a consequence more axion production. As axions are produced and leave the star, they take away energy which results in contracting and heating of the core which shortens the time the star spends in this phase. If these red giant stars

[5]The HR diagram is the Hertzsprung-Russel diagram, which is used to plot the luminosity of stars as a function of temperature. The stars are plotted as a scatter plot, each plot is for a given population of stars.

were to cool too fast, the HB stars would not be observed. With the observations of HB stars, we can set limits of the axion mass and coupling to photons, to prevent too-rapid cooling.

Observations of globular clusters (GCs) are used to constrain axions (or ALPs in this case) by counting stellar populations in different phases of stellar evolution. Globular clusters are populations of stars in the galactic halo which are gravitationally bound together. These GCs were formed early, they tend to have a higher density of stars than the surrounding space and the stars within often have a low metallicity[6], these factors make GCs relatively well understood and easier to model than other astronomical collections. In Figure 3-5 the HB limits were originally resulting from finding the R-parameter in multiple globular clusters, were R is ratio of the observed HB stars to the observed red giant branch stars in a given cluster [62]. The "Globular Clusters" limits in Figure 3-5 are from an alternate ratio, R_2 which is the ratio of asymptotic giant branch stars to HB stars [63]. The R_2 value used to create these limits was found by measuring 48 GCs in the Milky way using data from the Hubble Space telescope [64].

White Dwarfs

Much like for the HB stars, the presents of an axion affects the cooling of white dwarfs (WDs). For dense stellar objects like WDs, the primary production channel for axions is through their coupling to electrons,

$$\mathcal{L}_{aee} = \frac{C_{aee}}{2f_a}(\partial_\mu \phi_a)\bar{e}\gamma^\mu\gamma_5 e, \tag{3.4}$$

by axion bremsstrahlung off electrons, $e + Ze \rightarrow Ze + e + a$. Observations of the period of rotation of WDs slowing at rates higher than theory would suggest could be a sign of axion cooling [65, 66, 67, 68]. Global fits to a QCD axion with data from WD, HB stars, red giant stars and neutron stars (NSs) was conducted by [69], who found a best-fit axion mass of around 10 eV, but some tension remained with supernova and NS cooling results. The future IAXO and ARIADNE experiments will be able to probe the parameter space suggested by [69].

WDs can also be used to constrain other anomalies from observations of x-rays from magnetic WDs. These constrains are based on the axion coupling to photons, where an axion produced in the core of a magnetic WD may convert to an x-ray photon in the strong magnetic field of that same WD [70]. The x-ray observations of these magnetic WDs were be used to place limits on the combined $|g_{a\gamma\gamma}g_{aee}|$ in [70], and with more x-ray data from Chandra, new limits were placed in [71]. They additionally found limits on $g_{a\gamma\gamma}$ alone by taking $C_{aee} = C_{a\gamma\gamma}$ at tree level of $g_{a\gamma\gamma} < 4.4 \times 10^{-11}$ of $m_a \approx< 5 \times 10^{-6}$ eV.

[6] metallicity in stars refers to the abundance of elements heavier than helium in stars.

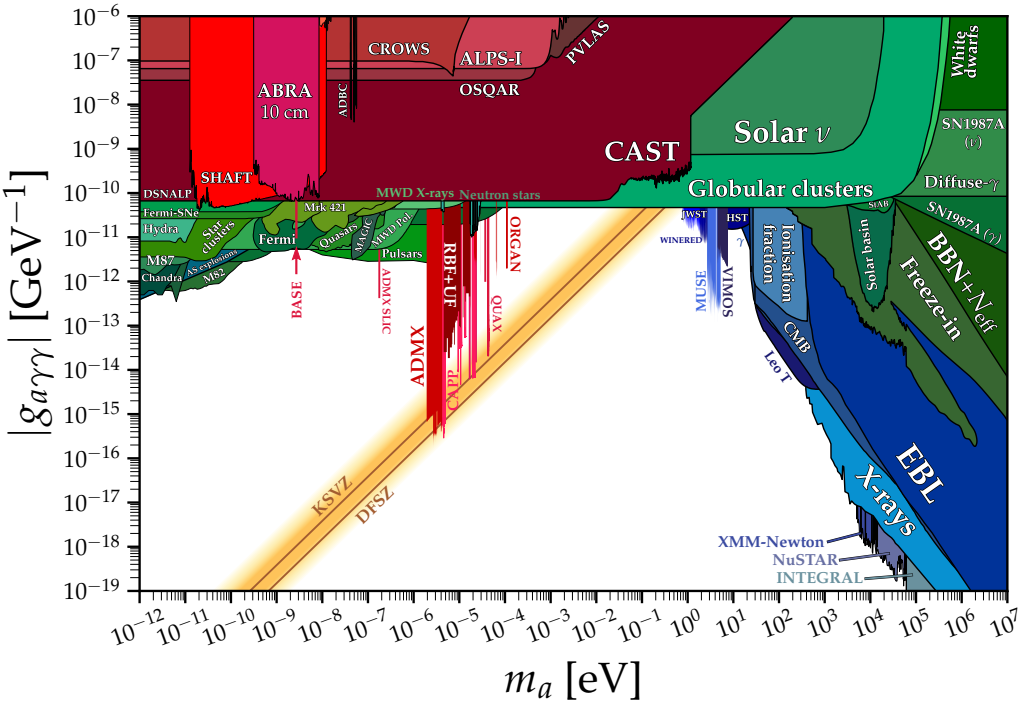

Figure 3-5: Reproduced from [14]. Limits of axion coupling to two photons from direction detection and astrophysical/cosmological searches.

3.2.3 Athermal Dark Matter: Primordial Black Holes

Primordial black holes (PBH) are one of the few viable non-particle candidates for CDM. A PBH describes a black hole (BH) formed in the early universe before matter-radiation equality. After they were first theorized in the late 1960s, interest in PBH has once again grown with the 2016 LIGO and Virgo discovery of GWs from a merger of BHs with masses around 30 $M_\odot$ [72]. These merging BH could be primordial, if that were the case they would fall in a mass range of interest where they could constitute a portion of the DM abundance, however there are astrophysical explanations for these BHs outside of primordial formation. PBHs are exciting for a number of reasons, their existence could lead to new cosmological physics, and they could be small enough in present day to constitute DM [73].

A BH formed after matter-radiation equality must be larger than 3 $M_\odot$ by the Tolman-Oppenheimer-Volkoff limit, but a PBH could have a mass below this limit if they were produced early in the age of the universe. Standard model BHs are formed from star death, placing a maximum creation age at the star formation, $z < 20$. A PBH would form if the density contrast (δ) in the plasma exceeded a critical value ($\delta_c = c_s^2$), defined as the square of the speed of sound during radiation domination. The mass of a PBH is on the order of the Horizon mass at the time of formation,

where the Horizon mass is given by

$$M_H \sim \frac{t}{G} \sim 10^{15}[g] \left(\frac{t}{10^{-23}[s]} \right), \tag{3.5}$$

with G as the gravitational constant. The relationship between the PBH and the Horizon mass goes as $M_{PBH} = \kappa M_H(\delta - \delta_C)^\gamma$, where the constants κ and γ are dependent on the shape of the primordial perturbation and the equation of state [73]. Limits on the density contrast place the bounds as $0.41 < \delta < 0.67$, which correspond to small pressure gradients on the larger limit, and large pressure gradients on the smaller limit [74].

Mass and abundance constraints on PBHs come from primarily astrophysical and cosmological sources, with GW-based direct detection experimental limits emerging at a slower rate. Some of the more prominent sources are listed below, with more depicted in Figure 3-6.

- The evaporation rate from Hawking radiation places a limit of $M_{PBH} > M_* = 4 \times 10^{14} g$ for PBHs with lifetimes longer than the age of the universe that could be around today. PBHs masses below $10^{17} g$ should emit a strong gamma ray signal, and therefore be more easily detectable. Absence of detection of a BH with mass $10^{17} g > M_{PBH} > M_*$ places constrains on the PBH parameter space.

- Microlensing from compact objects places another limit on PBHs. Lack of detection of sufficient microlensing events excluded standard massive compact halo objects (MACHOs) from being all of DM, however PBHs are constrained but not fully excluded since they can be smaller and even more compact, producing a smaller lensing effect.

- Gravitational waves observed by LIGO and Virgo restrict PBH merger rates to not exceed the rates that have been observed. This constraint affects PBHs in the mass range of 1 to 300 $M_\odot$ where LIGO/Virgo observations have been made [75].

- BHs emit radiation by accretion and by Hawking radiation, and this radiation can affect the CMB spectrum. The CMB spectrum can be altered from radiation by spectral distortions and modification of temperature anisotropies [76].

- NANOGrav is an experiment which uses radio pulsar timing to detect low-frequency GWs. The NANOGrav collaboration found evidence of a low-frequency GW background, which was recast as a limit on PBHs by making the assumption that the signal had an origin in scalar inducted GW for PBH formation [77, 78].

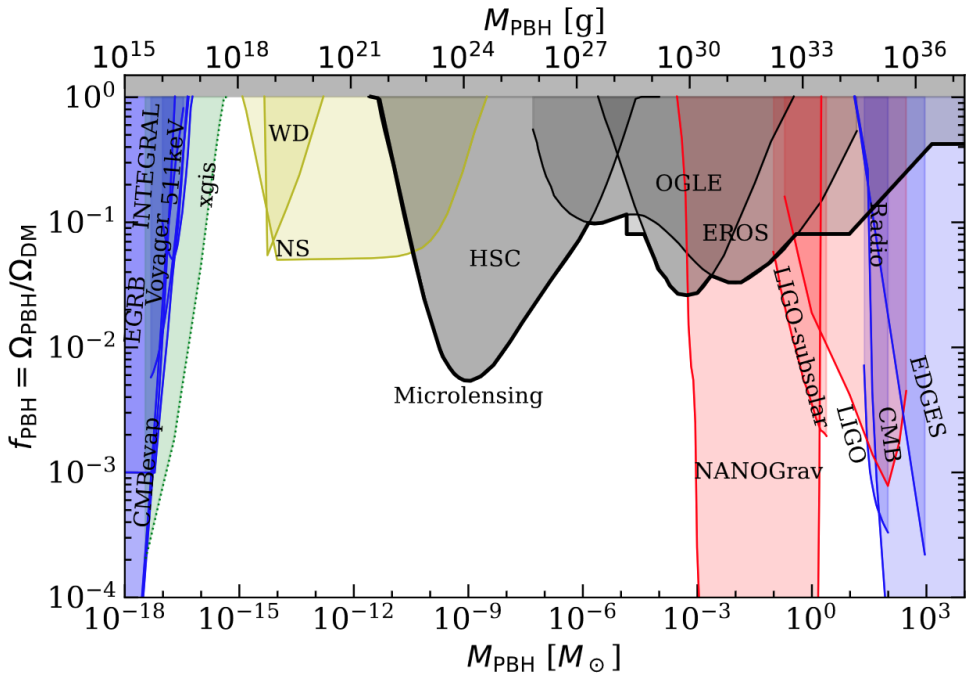

Figure 3-6: Reproduced from [79] generated using [80]. x-axis is the mass of the PBH, and the y-axis is the fraction of DM could consist of PBHs, with $f_{PBH} = 1$ as the DM abundance fully accounted for by PBHs.

3.3 Gravitational Waves

The first direct detection of GWs by the LIGO/Virgo collaborations in 2016 [49] marked one of the most prolific discoveries in modern physics, along with the discovery of the Higgs Boson in 2012 [81, 82]. LIGO, Virgo and KAGRA are long-baseline Michelson laser interferometers which are sensitive to the modification of arm length as a result of a passing GW. The three detectors used in tandem can correlate signal discoveries and triangulate the direction of the incoming GW signal [83].

3.3.1 What is a Gravitational Wave?

Gravitational waves were first theorized by Einstein in his theory of general relativity, they are propagating oscillations in the gravitational field caused by moving masses. Gravity is theorized to have a force carrier, the graviton which is described by a massless spin-2 field. Gravitons have not yet been discovered but are theorized to constitute GWs similarly to how photons constitute EM waves.

To get a concept of how GWs modify spacetime we can follow [84] by starting with the Einstein field equations that are used to describe the geometry of space time

as it relates matter and energy,

$$G_{\mu\nu} = R_{\mu\nu} - \frac{1}{2} g_{\mu\nu} R = \frac{8\pi G}{c^4} T_{\mu\nu}, \tag{3.6}$$

where $G_{\mu\nu}$ is the Einstein tensor, $R_{\mu\nu}$ is the Ricci tensor, R is the Ricci scalar, $g_{\mu\nu}$ is the metric tensor, G is Newton's constant and $T_{\mu\nu}$ is the energy momentum tensor. In the linearized theory where the source of the GW is considered weak, the flat-space metric tensor can be expanded to contain a small perturbation from a GW, $h_{\mu\nu}$,

$$g_{\mu\nu} = \eta_{\mu\nu} + h_{\mu\nu}, \qquad |h_{\mu\nu}| \ll 1. \tag{3.7}$$

Plugging in equation (3.7) into equation (3.6) and choosing the Lorentz gauge, $\partial^\nu \bar{h}_{\mu\nu} = 0$, the linearized Einstein equations become

$$\Box \bar{h}_{\mu\nu} = -\frac{16\pi G}{c^4} T_{\mu\nu} \qquad \text{for} \qquad \bar{h}_{\mu\nu} = h_{\mu\nu} - \frac{1}{2}\eta_{\mu\nu} h, \tag{3.8}$$

for $\Box$ as the flat space d'Alembertian, $\Box = \eta_{\mu\nu}\partial^\mu\partial^\nu = \partial^\mu_\mu$. From the Lorentz gauge and equation (3.8) we find $\partial^\nu T_{\mu\nu} = 0$, which is the conservation of energy-moment.

To study sources from outside the source location we can look at the transverse-traceless (TT) gauge. At the location of the observer, we have

$$\Box \bar{h}_{\mu\nu} = 0, \tag{3.9}$$

where now $\Box$ has taken the form of $-(1/c^2)\delta_t^2 + \nabla^2$ and we have taken the the energy momentum tensor $T_{\mu\nu}$ to be zero. From equation (3.9) we can conclude that GWs travel at the speed of light, which was later confirmed by LIGO/Virgo [49]. The TT frame is defined by setting

$$h^{0\mu} = 0, \quad h^i_i = 0, \quad \partial^j h_{ij} = 0. \tag{3.10}$$

The metric in the TT gauge is denoted by h^{TT}_{ij}, for the plane wave solution $h^{\mathrm{TT}}_{ij} = e_{ij}(\mathbf{k})e^{ikx}$ with $k^\mu = (\omega/c, \mathbf{k})$, $\omega/c = |\mathbf{k}|$ and the polarization tensor $e_{ij}(\mathbf{k})$. We now have

$$h^{\mathrm{TT}}_{ab}(t,z) = \begin{pmatrix} h_+ & h_\times \\ h_\times & -h_+ \end{pmatrix}_{ab} \cos[\omega(t - z/c)] \tag{3.11}$$

for a GW propagating in the z-direction originating from a source in the x-y plane, h_+ and $h_\times$ are the amplitudes of the plus and cross polarizations of the GW and a, b are the indices in the transverse plane (x, y).

We can express the strain tensor in terms of the second mass moment $M(t)^{ij} = \mu x^i_0(t) x^j_0(t)$ with reduced mass $\mu = m_1 m_2/(m_1 + m_2)$ from an expansion of the

quadrupole moment,

$$h_{ij} = \frac{2}{r}\frac{d^2 M(t)^{ij}}{dt^2}. \tag{3.12}$$

The two polarization of strain can now be expressed as

$$h_+ = \frac{1}{r}\frac{G}{c^4}\left(\ddot{M}_{11} - \ddot{M}_{22}\right), \qquad h_\times = \frac{1}{r}\frac{G}{c^4}\ddot{M}_{12}. \tag{3.13}$$

3.3.2 Sources of Gravitational Waves

The GWs which were detected by the LIGO/Virgo collaborations were created by merging compact objects, specifically BHs and NSs. Other sources which have been explored in recent years include GW backgrounds, such as GWs from the time of the CMB or super-massive BHs.

Compact object mergers

A merger of compact objects can be described in three distinct stages, a relatively frequency-stable in-spiral, the chirp where the two objects rapidly spin together and merge, and the ring-down, in which the excess angular momentum is radiated away from the new object. The in-spiral occurs in the weak-field regime where post-Newtonian approximations work well, but the chirp and the ring-down exist in the strong-field regime and require numerical relativity to be modeled. All three of these stages produce a GW signature, with the chirp having the highest frequency and amplitude in strain.

For the in-spiral portion we follow [85] for the Newtonian approximation. The in-spiral has a relationship between the orbital radius R and the orbital frequency given by Kepler's law

$$\omega_s^2 = \frac{Gm}{R^3}. \tag{3.14}$$

For a circular orbit in the (x, y) frame,

$$x_0(t) = R\cos(\omega_s t + \frac{\pi}{2}), \quad y_0(t) = R\sin(\omega_s t + \frac{\pi}{2}) \quad \text{and} \quad z_0(t) = 0, \tag{3.15}$$

the second mass moment now gives

$$\begin{aligned} M_{11} =& R^2\mu\cos^2(\omega t), \quad M_{22} = R^2\mu\sin^2(\omega t)\cos^2(\theta), \\ & M_{12} = R^2\mu\cos(\omega t)\sin(\omega t)\cos^2(\theta). \end{aligned} \tag{3.16}$$

The two components of strain polarization from equation (3.13) are now

$$h_+(t) = \frac{4}{r}\left(\frac{GM_c}{c^2}\right)^{5/3}\left(\frac{\pi f_{\rm gw}}{c}\right)^{2/3}\frac{1+\cos^2\theta}{2}\cos\left(2\pi f_{\rm gw}t_{\rm ret}+2\phi\right),$$
$$h_\times(t) = \frac{4}{r}\left(\frac{GM_c}{c^2}\right)^{5/3}\left(\frac{\pi f_{\rm gw}}{c}\right)^{2/3}\cos^2\theta\sin\left(2\pi f_{\rm gw}t_{\rm ret}+2\phi\right), \tag{3.17}$$

where $f_{\rm gw} = \omega_s/\pi = \omega_{\rm gw}/(2\pi)$, θ is the angle on inclination of the orbital plane, ϕ is the phase of the GW and M_c is the chirp mass,

$$M_c = \mu^{3/5}m^{2/5} = \frac{(m_1m_2)^{3/5}}{(m_1+m_2)^{1/5}}. \tag{3.18}$$

The total power radiated by the in-spiral is

$$P = \frac{32}{5}\frac{c^5}{G}\left(\frac{GM_c\omega_{\rm gw}}{2c^3}\right)^{10/3}. \tag{3.19}$$

As the compact objects orbit one another and lose energy through the emission of GWs the radius of the orbit must decrease, and as a consequence of equation (3.14), ω_s must also increase. As ω_s increase more power is emitted in the form of GWs repeating the cycle in quasi-circular motion until coalescence under the condition $\dot{\omega}_s \ll \omega_s^2$. The frequency of the GW at a time to coalescence $\tau = t_{\rm merge} - t$ is

$$f_{\rm gw}(\tau) = \frac{1}{\pi}\left(\frac{5}{256}\frac{1}{\tau}\right)^{3/8}\left(\frac{GM_c}{c^3}\right)^{-5/8} \simeq 134{\rm Hz}\left(\frac{1.21M_\odot}{M_c}\right)^{5/8}\left(\frac{1s}{\tau}\right)^{3/8}. \tag{3.20}$$

As a useful metric for detection, we can calculate the number of cycles the binary will in-spiral within the detector's bandwidth $f \in [f_{\rm min}, f_{\rm max}]$,

$$\begin{aligned}\mathcal{N}_{\rm cyc} &= \frac{1}{32\pi^{8/3}}\left(\frac{GM_c}{c^3}\right)^{-5/3}\left(f_{\rm min}^{-5/3} - f_{\rm max}^{-5/3}\right) \\ &\simeq 1.6\times10^4\left(\frac{10{\rm MHz}}{f_{\rm min}}\right)^{5/3}\left(\frac{1.2M_\odot}{M_c}\right)^{5/3},\end{aligned} \tag{3.21}$$

assuming $f_{\rm min}^{-5/3} - f_{\rm max}^{-5/3} \simeq f_{\rm min}^{-5/3}$.

As the two compact objects spiral in towards one another the assumption they are perturbations in a flat-space metric becomes less reasonable, specifically the in-spirally objects will eventually reach an innermost stable circular orbit (ISCO) with a corresponding source frequency $(f_s)_{\rm ISCO} \simeq 2.2{\rm kHz}\frac{M_\odot}{m}$ for $m_1 = m_2 = m$. The

form of the wave functions when the two objects coalescence, "the plunge", and the resulting ring-down requires numerical relativity to solve for the GW forms, and these are calculated to form templates. With matched filtering these templates are used in GW searches to make discoveries.

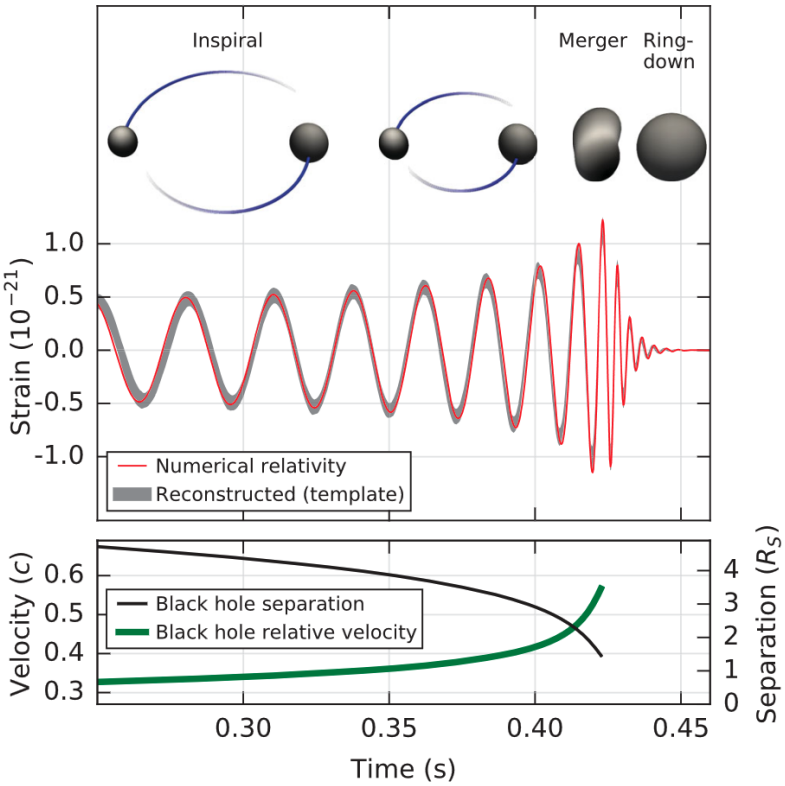

Figure 3-7: Reproduced from [49]. Estimated GW strain amplitude from GW150914 and the Keplerian effective BH separation for Schwarzschild radii $R_s = 2GM/c^2$.

LIGO and VIRGO have observed BH-BH mergers, BH-NS mergers, and NS-NS mergers. NS-NS mergers are of particular interest since they are theorized to be the major factory for the rapid neutron capture process (r-process), which is responsible for the nucleosynthesis of the majority of elements heavier than iron in the universe [86].

Gravitational wave backgrounds

A stochastic background can be either be generated from early universe productions of GW which have formed a GW background similarly to how the CMB has formed an electromagnetic background, or a combination of astrophysical sources which have formed an incoherent superposition of GWs. A stochastic background is characterized by four qualities, first, the background must be stationary, the point in time of observation should not affect the observed signal. Second, the background is Gaussian

distributed, stemming from the central limit theory for the astrophysically sourced stochastic background. Third, the background will likely be isotropic, as most cosmological sources are, but deviations from the isotropy are not unexpected. Fourth, the background should be unpolarized if it is a combination of many different sources, and a cosmological GW is also expected to be unpolarized [84]. A cosmologically sourced GW produced with frequency f_* will have a frequency today of

$$f_0 = f_* \frac{a(t_*)}{a(t_0)} \simeq 2.65 \times 10^{-8} \frac{1}{\epsilon_*} \left(\frac{T_*}{1\text{GeV}} \right) \left(\frac{g_*}{106.75} \right)^{1/6} \text{Hz}, \tag{3.22}$$

where a is the cosmological scale factor, t_0 is the time now, and all quantities denoted by * are properties during the production of the GW, t_* is the time, ϵ_* is the super-horizon modes, T_* is the temperature and g_* is the number of spin or helicity states [87].

Anisotropies present at the time of inflation (the surface of last scattering) would polarize the CMB. The presents of anisotropies in the CMB were confirmed by the detection of temperature fluctuations. The pre-inflation anisotropies produce magnetic (B-mode) polarizations which probe the surface of last scattering directly, unlike temperature fluctuations which were formed between then and now, meaning B-modes would be direct proof of inflation [88]. Fluctuations in polarization are theorized to be smaller than fluctuations in temperature, making them very difficult to detect and distinguish [89]. B-mode detections have been claimed but cannot be verified to have originated from Inflation, as cosmic dust cannot be fully ruled-out as the source of the detection [90, 91]. A detection of B-modes would additionally be a measurement of GWs, since the GWs generated during Inflation are the cause of the anisotropies which created the B-modes. GWs from inflation are expected to have a frequency range of $f_{\text{CMB}} \sim 10^{-18} - 10^{-17}$ Hz [92].

The GW background's effects on the CMB could be modified by the existence of ALPs during inflation. The particle physics model of inflation requires a flat scalar potential which can be achieved by assuming the inflaton[7] is a pseudo Nambu-Goldston boson, which arises from string theory [93]. This pseudo Nambu-Goldston boson could be an ALP, lighter than the QCD axion, which couples to EM fields, the inflationary ALP cannot couple to QCD and therefore cannot be a solution to the strong-CP problem. If the ALPs began their oscillations between Recombination and now, the CMB polarizations would be affected by a rotation of the polarization plane, $\Delta\alpha$. A non-zero $\Delta\alpha$ would cause some of the E-modes of the CMB to rotate to B-modes, in this way ALPs do not generate B-modes, but their presents does cause a shift to more B-modes [94]. $\Delta\alpha$ has been constrained to $0.0^\circ \pm 0.37^\circ$ by the Planck collaboration at a 65% confidence level [95].

There are many of other sources of GW backgrounds at all frequencies produced by non-equilibrium phenomena in the early universe. The NANOGrav collaboration

[7] the inflaton is a scalar field which drives inflation in particle and string theories.

saw signs of a low-frequency GW background in their 15-year dataset analysis, which could be signs for many different types of physics, and they focused their analysis on super-massive BHs in the center of galaxies [77]. The NANOGrav results have also been cast to PBHs limits as discussed above.

A new generation of interferometry-based detectors in space will begin with the Laser Interferometer Space Antenna (LISA), which will have an expected frequency range of $f_{\rm CMB} \sim 10^{-5} - 0.1$ Hz with arms stretching lengths of millions of miles [92]. LISA's main goal is to look for massive BH binaries, but the detector will also be able to look for GW backgrounds [92]. There are also new generations of ground-based interferometers which will reach new greater sensitivities, some being built underground to reduce noise [96, 97].

3.3.3 High-Frequency Gravitational Waves

LIGO has searched for and found evidence of GWs with sensitivity up to around 10 kHz, which marks the highest frequency expected for GWs created by SM BH-BH mergers, NS-BH mergers and NS-NS mergers. GWs producing high frequency signals above 10 kHz could be the result of beyond the SM physics such as PBH mergers and superradiance, or early universe stochastic signals such as signs of preheating or phase transitions [98, 92]. Figure 3-8 presents possible early universe high-frequency GW (HFGW) signals and current/future projections from experiments.

The BBN bound

Big Bang Nucleosynthesis (BBN) marks the first production of stable nuclei in the history of the universe, it begins at a time around 3 minutes after the big bang, at a temperature of T $\sim$ 0.1 MeV, when nuclei can form without photo-dissociation. BBN lasted until around t $\sim$ 20 minutes and T $\sim$ 0.03 MeV, ending with the expansion and cooling of the universe to the point that the Coulomb barrier is too high for fusion processes to occur at any appreciable rate. By the end of BBN almost all free neutrons are bound into 4He nuclei. The result of BBN is a universe that is approximately 75% hydrogen and 25% helium. We understand BBN relatively well from the nuclear physics of the binding energies, and from astrophysical observations of abundances, the only two free parameters of BBN are baryon number and the effective neutrino number, $N_{\rm eff}$. Given our good understanding of BBN, it can be used in combination with our knowledge on the radiation from the surface of last scattering to constrain the total energy density of the GW background [98].

An excess of radiation before BBN would be apparent in $N_{\rm eff}$, which is related to the energy density of the GW background $\rho_{\rm GW}$ through $\Delta\rho_{\rm rad} = \frac{\pi^2}{30}\frac{7}{4}\left(\frac{4}{11}\right)^{4/3}\Delta N_{\rm eff} T^4$ and $\rho_{\rm GW}(T) \leq \Delta\rho_{\rm rad}(T)$. For $N_{\rm eff} < 0.2$ [99], the energy density of the GW wave

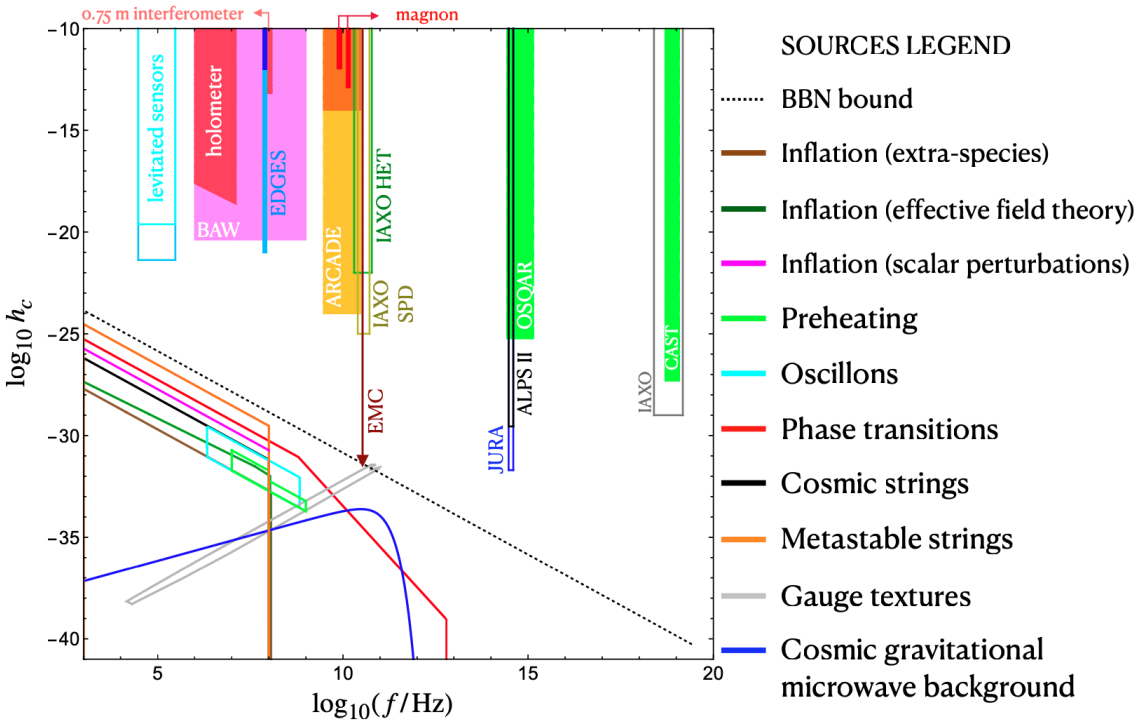

Figure 3-8: Reproduced from [98]. Projections of experimental sensitivity to HFGWs and possible HFGW sources.

background produced before BBN is constrained by

$$\left(\frac{\rho_{\mathrm{GW}} h_H^2}{\rho_c}\right)_0 < 1.12 \times 10^{-6}, \tag{3.23}$$

with $H_0 = h_H \times 100\mathrm{km\,sec^{-1}\,Mpc^{-1}}$ and critical energy density $\rho_c = 3H_0^2/(8\pi G)$ need for obtaining the Hubble parameter today H_0. This limit corresponds to frequencies $f \geq 1.5 \times 10^{-12}$ Hz as shown in Figure 3-8 [98].

Superradiance

Superradiance describes loss of energy from the formation of gravitational bound states around a rapidly spinning BH by spin-0 bosons [100, 101, 102, 103]. For superradiance to occur, the Compton wavelength of the boson must be on the order of the BH size. For astrophysical BHs, axions in the mass range of 10^{-22} eV to 10^{-10} eV could undergo the Penrose superradiance process by which the BH and axion-cloud system loses energy through GW emission [94]. The mass of the axion which could

form a superradiant state around a given BH is

$$m_a \sim \left(\frac{M_\odot}{M_{BH}}\right) 10^{-10}\text{eV}, \tag{3.24}$$

found from the Compton wavelength of the axion [98].

The GW emission is produced by axions losing energy in their atomic-like states around the spinning BH. The axions primarily release energy as they transition to lower energy states in the form of annihilating to gravitons, $a+a \to g$ with momentum $k_g \approx 2m_a$. The expected GW signal amplitude at the detector for annihilation is

$$h_0 \sim 10^{-22}\alpha^7\epsilon \left(\frac{10\,\text{Mpc}}{r}\right)\left(\frac{M_{\text{BH}}}{2M_\odot}\right), \tag{3.25}$$

where $\alpha = m_a r_g$ for the gravitation radius of the BH r_g, ϵ is the fraction of BH mass accumulated in the surrounding cloud and r is the distance to the source [104]. The resulting annihilation signal frequency is

$$f \approx 30\,\text{kHz}\,\alpha \left(\frac{M_{\text{BH}}}{2M_\odot}\right). \tag{3.26}$$

Additionally, axions are theorized to decay to two gravitons $a \to g + g$ during superradiance, producing a GW with a frequency of

$$f = \frac{k_r}{2\pi} = 1.2 \times 10^4 \left(\frac{m_a}{10^{-10}[\text{eV}]}\right)[\text{Hz}] \tag{3.27}$$

where k_r is the wavenumber [105]. The expected strain amplitude for axion decay is given by

$$h_0 \sim 10^{-24}\left(\frac{1\,\text{MHz}}{f}\right)\left(\frac{\epsilon M_{\text{BH}}}{10^{-7}M_\odot}\right)^{1/2}\left(\frac{10\,\text{kpc}}{D}\right), \tag{3.28}$$

for a distance from the observer D [98, 106].

Methods for searching for HFGWs

As a result of their shorter wavelengths, HFGWs are not well suited for searches with interferometers, which operate best for GW wavelengths longer than the length of the arms. Shorter arms decrease the sensitivity to strain, making interferometers difficult for HFGW searches. A search up for GWs up to 100 MHz was conducted by [107] with a 75 cm baseline to a strain sensitivity of $\sim 10^{-16}\,\text{Hz}^{-1/2}$, and the NEMO detector which is designed specifically to search for spinning NS-remnants from NS mergers would be sensitive to kHz regime with a 4 km baseline [108]. To achieve sensitivity to higher frequencies, other techniques are explored such as bulk acoustic wave (BAW) detectors, EM detection through the inverse Gertsenshtein effect and

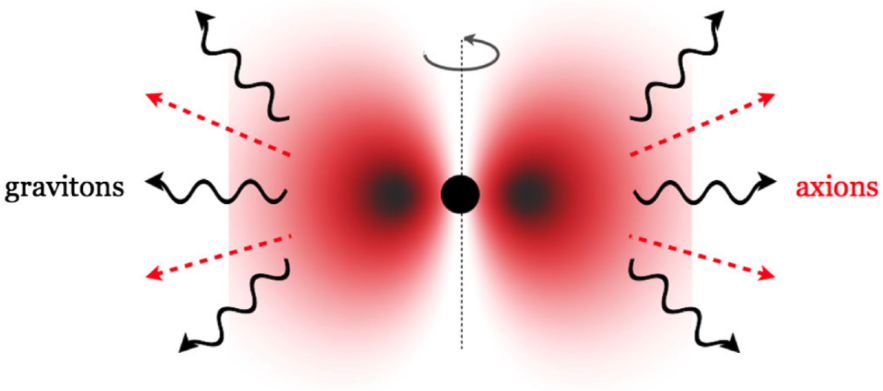

Figure 3-9: Reproduced from [104]. A rotating BH surrounded by an atomic-like axion cloud in a superradiant state, gravitons are emitted as the axions lose energy.

mechanical and EM cavity excitations.

The BAW detectors principally operate by resonantly trapping a large amount of phonons between borders to create a phonon cavity. By using a piezoelectric material, the phonons created from vibrations are converted to electric signals which can be measured with an amplifying circuit [109]. At cryogenic temperatures these devices have very high quality factors, with $Q \sim 10^6 - 10^9$, and can be tuned with a DC bias voltage to a specific frequency, these devices typically operate in the MHz regime [110, 111]. BAW detectors can act as a resonant mass antenna to search for HFGWs, the MAGE experiment [112] uses two quartz BAW resonators coupled to SQUIDs taking data simultaneously to exclude localized backgrounds and dark counts. The GWs couple to acoustic modes in the BAW resonators, which are narrow bands of around 1 Hz, and multiple modes are are monitored at once. MAGE has sensitivity down to $6.6 \times 10^{-21}\, 1/\sqrt{\text{Hz}}$ in its first iteration and is expecting to achieve greater sensitivity with the addition of more BAWs.

Inverse Gertsenshtein effect [113, 114] describes the relationship between GWs and photons, and was proposed as a method for GW detection. At low frequencies, mechanical strain detection has proved to be much more successful, but EM detection is possible at all frequencies, including high frequencies where many mechanical systems may have difficulties. In an analogy to axions, GWs can be searched for by GW conversion to photons in a magnetic field. Limits can be placed on GWs from existing axion data based on the inverse Gertsenshtein effect, and existing axion experiments can be used in modified configurations to search for GW signals. In [115] they use the back end of light-shining-through-walls axion experiments to search for GWs. Recall from Chapter 2, light-shing-though-walls experiments rely on the use of two cavities, one for production and one for detection. Since the GWs are difficult to produce in appreciable quantities, only the detection cavity is used and the signal

is from either an astrophysical or cosmological source, see Figure 3-10. Using existing data from the ALPS, OSQAR and CAST collaborations they set limits down to $h_c^{\min} \approx 6 \times 10^{-26}$ for a frequency of $(2.7 - 14) \times 10^{14}$ Hz and $h_c^{\min} \approx 5 \times 10^{-28}$ for a frequency of $(5 - 12) \times 10^{18}$ Hz, as seen in Figure 3-8 [115]. Similarly, data from resonant cavity axion experiments can be recast to HFGW limits, reaching sensitivities down to $h \sim 10^{-22} - 10^{-21}$ [116]. GW electrodynamics are explored in more detail in Chapter 6, along with the results from using the ABRACADABRA-10cm experiment to search for HFGWs.

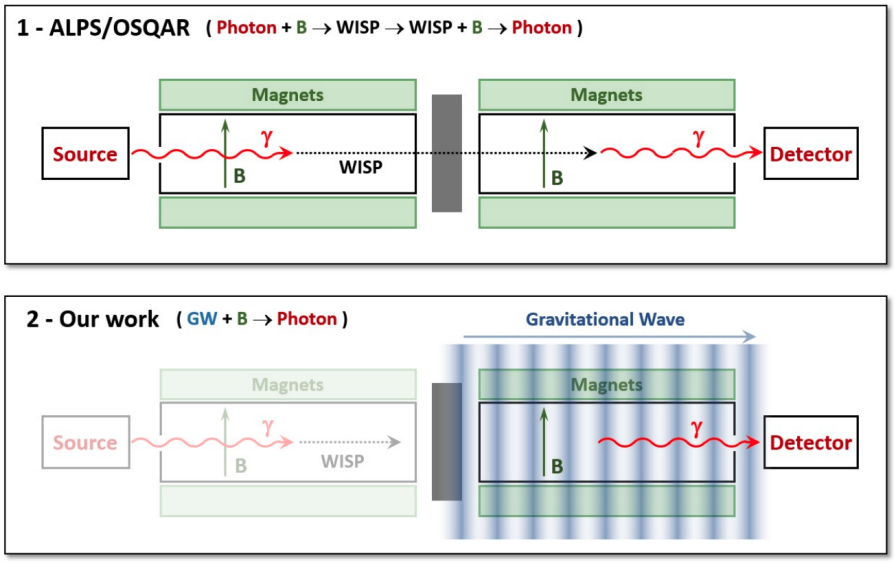

Figure 3-10: Reproduced from [115]. Top: standard setup for a light-shining-through-walls axion detection experiment. Bottom: modification for the detection of GWs.

EM cavities can be used to search for HFGWs by utilizing mechanical excitations in the cavities to produce an EM signal, similarly to a traditional Weber bar[8]. In particular, the MAGO 2.0 [118] experiment will utilize both the mechanical resonances signal, and the EM signal from the inverse Gertsenshtein effect to search for GWs. The superconducting radio-frequency cavity of the MAGO 2.0 detector has two EM resonant modes tuned to the frequency of the pump mode ω_0 and the signal mode ω_1 such that a GW with a frequency $\omega_g \ll \omega_0, \omega_1 \sim 1$ GHz fits the mode splitting $\omega_g \simeq |\omega_1 - \omega_0|$. The signal mode is initially empty and can be tuned to achieve the desired mode splitting dictated by the GW interaction with the pump mode, and energy is resonantly transfer from the pump mode to the signal mode if a GW interacts with the detector. The use of superconducting radio-frequency cavities allows for

[8]A Weber bar was designed by Joseph Weber as the first resonant-mass GW detector, utilizing vibrational eigenmodes to couple to the GW signal [117]. The more modern version of the Weber bar are the spherical resonant mass detectors.

low-noise detection, and the MAGO 2.0 experiment will operate in broadband mode, allowing for the search of transient signals.

The search for DM and HFGWs is ongoing, with the relatively young field of HFGW detection embarking on many new detection methods and experiments. Small signals pose many challenges for detection, and by their nature both DM and HFGW produce extremely small signals. Continued effort from the communities and new ideas are need for us to discover the nature of DM and detect HFGWs.

Chapter 4

ABRACADABRA-10cm Detector

The ABRACADABRA-10cm experiment (ABRA) was designed as a first-of-its-kind lumped-element axion direct-detection experiment [35]. As discussed in Chapter 2, "lumped-element" refers to using individual circuit components to inductively couple to the axion effective current [119]. ABRA has two published axion campaigns, Run 1 in [33, 32] and Run 3 in [120], and an in-progress gravitational waves search, see Chapter 6.

This chapter is structured by first a discussion of the large physical components of the experiment, then a discussion of the parts of the detector which are used directly in detecting a signal, and finally a discussion of the calibration and the data acquisition system (DAQ).

4.1 Large Detector Components

The ABRA detector is located on the ground floor of MIT building 24 between a server room and a chemical storage room. The experimental apparatus consists of a 1 T superconducting toroidal magnet, a calibration circuit and two two-stage DC SQUID current sensors and their readouts inside a dry dilution refrigerator, along with an external DAQ. The signal-to-noise relation for the axion signal is,

$$SNR = g_{a\gamma\gamma}\sqrt{\rho_{DM}}\mathcal{G}_V V B_{\max}\left(\frac{M_{in}}{L_T}\right)\frac{(\tau t)^{1/4}}{S_{\Phi\Phi}^{1/2}}, \tag{4.1}$$

where $g_{a\gamma\gamma}$ is the axion to two photons coupling constant, ρ_{DM} is the local DM density, $\mathcal{G}_V$ is a geometric factor, V is the magnetic volume, $B_{\max}$ is the maximum magnetic field inside the toroid, M_{in} is the mutual inductance coupling into the SQUID, L_T is the total inductance of the readout circuit, τ is the axion coherence time, t is the integration time and $S_{\Phi\Phi}$ is the flux noise level. To get the $(\tau t)^{1/4}$ factor, we assume the axion coherence time is much less than the total integration time [121]. For ABRA Runs 1 and 3 the total integration time for the axion searches were around

a month each. Relevant parameters for Runs 2 and 3, as well as the backgrounds investigations campaign (Runs 4 and 5) can be found in Table 4.1 [32]. Parameters for Run 6, which searched for both axions and gravitational waves, can be found in Chapter 6 and Appendix C.

Detector Design Parameters		
Pickup Cylinder Radius	R_p	5.1 cm
Pickup Cylinder Height	H_p	10 cm
Pickup Cylinder thickness	r_p	150 μm
Magnet Inner Radius	R_{in}	30 mm
Magnet Outer Radius	R_{out}	60 mm
Magnet Height	h	120 mm
Magnet Max Field	B_{max}	1.0 T
Geometric Factor	$\mathcal{G}_V$	0.031
Total Impedance	L_p	800 nH
SQUID Input Inductance	L_{in}	150 nH
SQUID Inductive Coupling	M_{in}	2.5 nH

Table 4.1: Design parameters for ABRACADABRA-10cm Runs 2-5 with a cylindrical pickup structure.

4.1.1 Magnet

The magnet used for ABRA is a superconducting 1 T DC toroidal magnet manufactured by Superconducting Systems Incorporated (SSI), with a magnet field that falls off as $1/\rho$ towards the center of the magnet. The dimensions of the magnet measure about 12 cm in height and diameter, with an inner radius of around 3 cm, giving a total magnetic volume of around a liter (a more detailed description of magnetic volume is described in section 5.2). The magnet was wound with NbTi wire (critical temperature around 10 K) in three separate pieces, then secured together with glue and superconducting crimps. The wires are supported by a 80 identical Delrin wedges which form the mandrel. The NbTi wire winds around the mandrel 1280 times, fitting into the 80 groves between each pair of Delrin wedges. The magnet is charged by injecting 121 A of current into the magnet leads on the warm side of the fridge which connect down to the magnet through a series of normal conducting wires, high-temperature superconducting wires, a superconducting switch and cold superconducting wires. These cold superconducting wires having a limited length, and as a result the wires are not well thermalized at each cooling stage. The lack of proper thermalization on the wires limit the base temperature of the magnet to just over 1 K (measurement taken on the shield of the magnet) and allow noise to be carried down into the system from the magnet leads as they act as antennas, see section 5.3 for more descriptions of backgrounds. Portions of the magnet description

were adapted from [32].

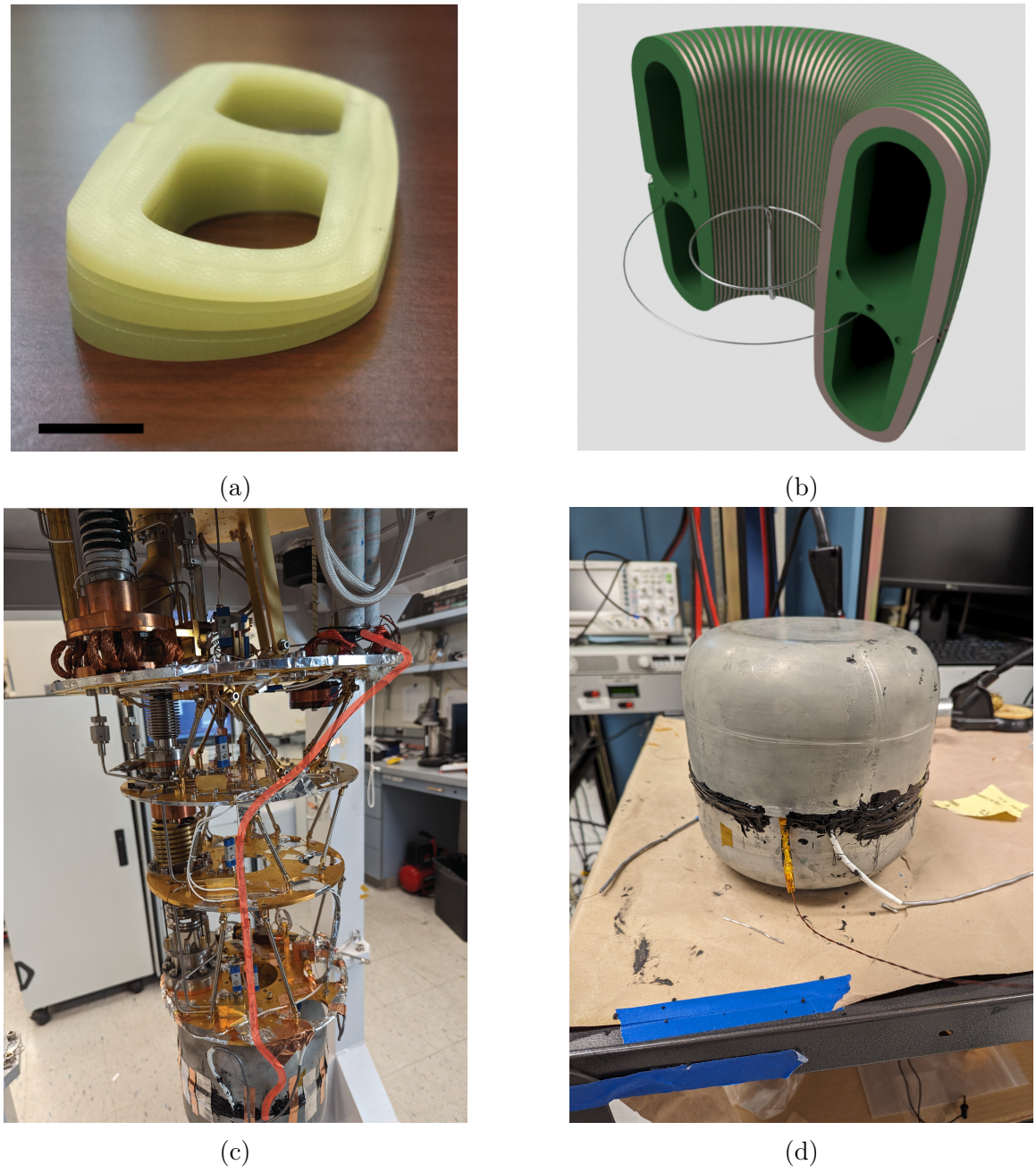

(a) (b)

(c) (d)

Figure 4-1: (a) Delrin wedges which for the mandrel, black bar indicating 1 cm, adapted from [32]. (b) CAD of a cross-section of the ABRA magnet, including Run 1 pickup loop and axion calibration loop, also adapted from [32]. (c) inside of the dilution refrigerator highlighting the path of the cold superconducting portion of the magnet wires. (d) tin-coated copper magnet shield.

The magnet is surrounded by a tin-coated copper shield. The tin layer is superconducting just under 4 K and approximately 25-75 μm thick. The shield was epoxied together with Sili-Thane™ 803 Sealant and solder was placed in the gap between the two shield halves. Solder becomes superconducting at temperatures below 5 K, and when placed between the halves it creates an electrical connection and provides a more complete electromagnetic shield. The shield-magnet system is suspended from a steel spring and Kevlar string system with a pendulum mode which rolls off below 0.4 Hz laterally and below 0.3 Hz vertically [32].

From photos of the magnet, we have concluded that the magnet was not counter-wound[1]. Not counter-winding the magnet results in a small azimuthal current in the toroid as the magnet wires cross between the groves in the mandrill, this current creates a DC field in the center of the toroid, and possibly a higher mutual inductance between the magnet and other components in the fridge. Fortunately, as a result of the oscillating nature of the axion signal, the field from a non-counter-wound magnet does not mimic an axion signal, it just increases our overall noise levels as there would be stray fields in the z-direction resulting from the azimuthal current.

Figure 4-2: Close-up image of the ABRA magnet wires, the wire only appears to cross in one direction as the wire is wound between Delrin wedges and does not cross back, suggesting that the magnet was not counter-wound.

[1]The magnet was ordered to have been counter-wound to prevent azimuthal currents.

4.1.2 The ABRACADABRA-10cm dilution refrigerator

ABRA uses a dry dilution refrigerator designed by Oxford Engineering which relies on pulse tubes to cool the mixture of He3 and He4 down to around 3K before the dilution unit cools the mixture to lower temperatures. These pulse tubes operate at 1.4 Hz and introduce harmonic vibrations into our system, which are explored in more detail in section 5.3. The magnet is thermalized to the mixing chamber stage, the coldest stage of the refrigerator. The mixing chamber also hosts either one or both of the SQUIDs (depending on the run configuration), and with the heat-load from the magnet the mixing chamber plate sits around 800 mK. The magnet reaches temperatures a little above 1 K, cold enough to ensure our data is not overwhelmed by thermal noise floor. With the magnet removed our dilution refrigerator would reach temperatures under 100 mK on the mixing chamber stage.

To mitigate external electromagnetic noise, a MuMetal shield is constructed around the body of the refrigerator, which covers the sides and bottom of the vacuum-holding external cans. The MuMetal is plated 200 μm thick on the external cans, and not on any of the internal radiation-shielding cans, since MuMetal becomes less effective at lower temperatures. After the MuMetal was shaped around our cans it was not re-annealed, meaning the shielding capabilities of the MuMetal were not as high as they would have been had it not been bent. The MuMetal shield was measured before Run 1 ex-situ to attenuate a DC magnetic field at a factor of $\sim 5 - 10$ [32].

4.2 Detection method

ABRACADABRA-10cm is designed to detect trace currents made by weakly[2] interacting phenomenon. To accomplish this extremely sensitive detection we turn to superconducting detection methods and devices. A superconducting pickup structure detects the current and is connected to a superconducting quantum interference device (SQUID) which is read out to an analog to digital converter (ADC), otherwise known as a digitizer.

4.2.1 Pickup structure

The pickup structure in any given ABRA detection campaign is built from NbTi and in a form in which the given signal would induce a current. NbTi is superconducting under around 10 K. For the axion detection campaigns these pickups have cylindrical symmetry to detect the azimuthally-symmetric axion signal. An effective current is the induced in the DC magnetic volume, resulting in a z-directional oscillating magnetic field in the otherwise (ideally) field-free region in the center of the toroid. Runs 1 and 6 used a loop of wire as the pickup structure for detecting axions, while Runs 2-5 used a cylinder for their respective axion or noise searches.

[2] as in low in coupling strength, not as in the weak force.

The GW signal has a much more complicated effective current structure which breaks cylindrical symmetry; therefore a stronger current is induced in the pickup if the pickup also breaks cylindrical symmetry. The form of the pickup for the GW signal is a circular figure-8, see Figure 3-3. To capture as much of the signal as possible, the form of the figure-8 is almost that of two connected semi-circles. The figure-8 pickup was only included in the Run 6 design.

All the pickup structures had a NbTi twisted pair which was an extension of the pickup loop wire (or was soldered on in the case of the cylindrical pickup) that exited the shield and was connected to a SQUID. These twisted pairs were shielded individually using hollowed-out solder which originally had a rosin core and is superconducting at the temperatures of the shield and SQUIDs.

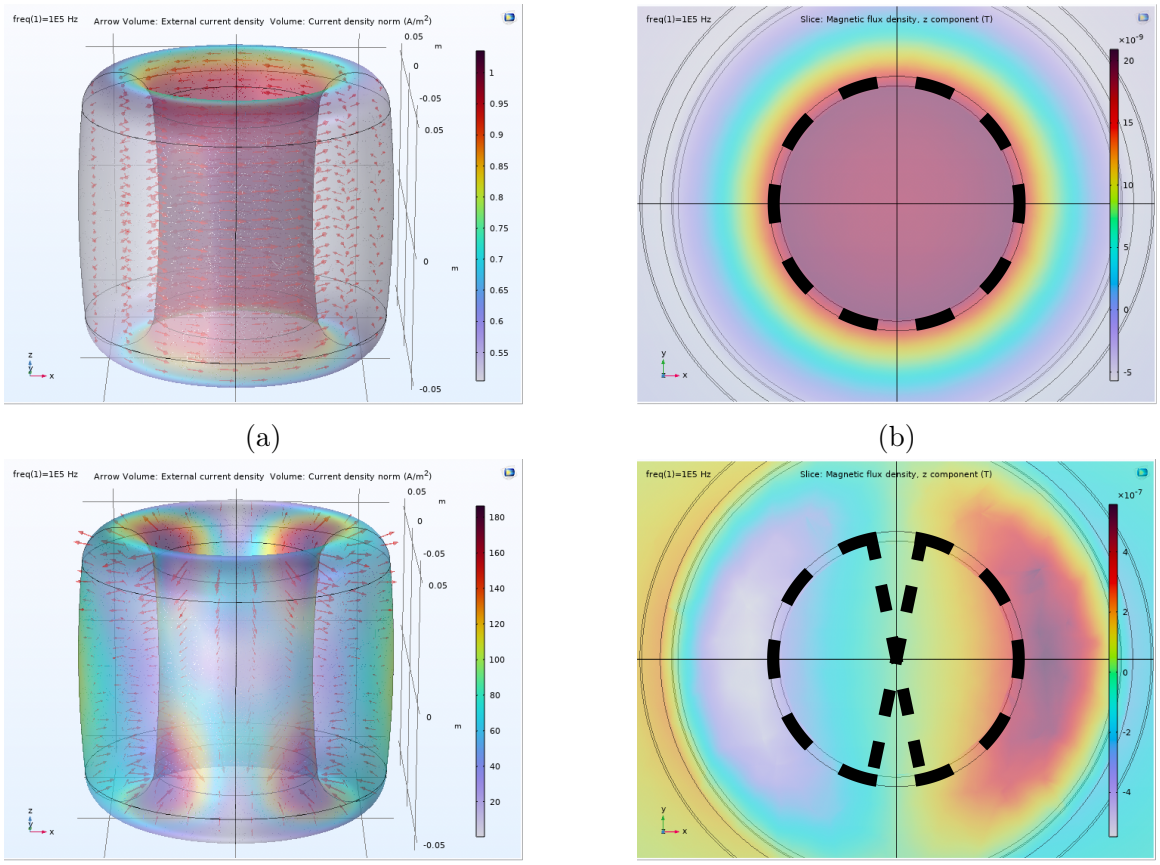

Figure 4-3: COMSOL models of the two signals searched for with ABRACADABRA-10cm, values shown are only used for relative comparison and the absolute values are only for display purposes. (a) and (c) are the volume current in the magnet resulting from an axion-like effective current (a) and a GW-like effective current (c). (b) and (d) are the z-component of the magnetic field from an axion-like signal (b) or a GW-like signal (d) in a top-down view, dashed black lines represent pickup loops.

4.2.2 Superconducting quantum interference devices

The current collected on the individual pickups was detected by two-stage DC Magnicon SQUIDs. The following section on the principles of DC SQUIDs is based on the work in [122].

DC SQUIDS

SQUIDs use the principles of flux quantization and Josephson tunneling to detect trace amounts of current. Josephson tunneling describes the tunneling of Cooper pairs between two super conductors through an insulator or barrier. The current through a junction is given by $I = I_0 \sin\delta$, where I_0 is the critical current and $\delta = \phi_1 - \phi_2$ is the phase difference between the superconducting electrodes. For a voltage U between the electrodes the phase difference changes with time as

$$\frac{d\delta}{dt} = \frac{2eU}{\hbar} = \frac{2\pi U}{\Phi_0}, \tag{4.2}$$

where Φ_0 is the magnetic flux quantum, a unit of measurement equal to $h/2e \approx 2.07 \times 10^{-15}$ Wb. For a static system with $U = 0$, a DC superconducting current can get up to critical current I_0 across the junction. For the non-static case where $U \neq 0$, I_j oscillates at a frequency of $\omega_j = 2\pi V/\Phi_0$, defined as the Josephson frequency, where V is the time-averaged DC voltage across the junction.

The most basic DC SQUID has two Josephson junctions connected in parallel in a superconducting circuit. Practically, most DC SQUIDs use a shunt to eliminate hysteresis on $I - V$ characteristics. A shunt can be made either resistively or capacitively, here the resistive shunt is explored. A resistor of resistance R can be added to a junction with critical current I_0 and self-capacitance C to mitigate hysteresis if

$$\beta_C \equiv 2\pi I_0 R^2 C/\Phi_0 = \omega_j RC \leq 1, \tag{4.3}$$

where ω_j the Josephson frequency for a voltage of $I_0 R$. If $\beta_C \ll 1$, now

$$V = R(I^2 - I_0^2)^{1/2}, \tag{4.4}$$

and as $I_0 \ll I$ the $I - V$ characteristic converges to $V = IR$ and hysteresis is not a large effect.

Figure 4-4 (a) depicts a basic DC SQUID with a bias current I_b. Changes in magnetic flux cause V to oscillate between extrema as seen in (c), resulting in a maximum reaction to a small change in flux. A maximal flux-to-voltage transfer coefficient, $V_\Phi \equiv |(\partial V/\partial \Phi_a)_I|$, occurs for $\delta\Phi_a \ll \Phi_0$, when $\Phi_a \approx (2n+1)\Phi_0/4$. Change in voltage ($\delta V = V_\Phi \delta\Phi_a$) is approximately linear in $\delta\Phi_a$ for a maximal flux-to-voltage coefficient.

DC SQUIDs operating below 10 MHz are typically run in flux-locked feedback loop (FLL) mode, which linearizes the flux response of the SQUID and maintains

proportionality between the voltage and flux for large changes in flux. If the voltage in response to a large flux increases past the working points by a change in voltage V_b, a feedback resistor with resistance R_f and a feedback coil with mutual inductance M_f with respect to the SQUID is used to amplify and integrate V_b so it can be fed back into the SQUID and working points can be re-established.

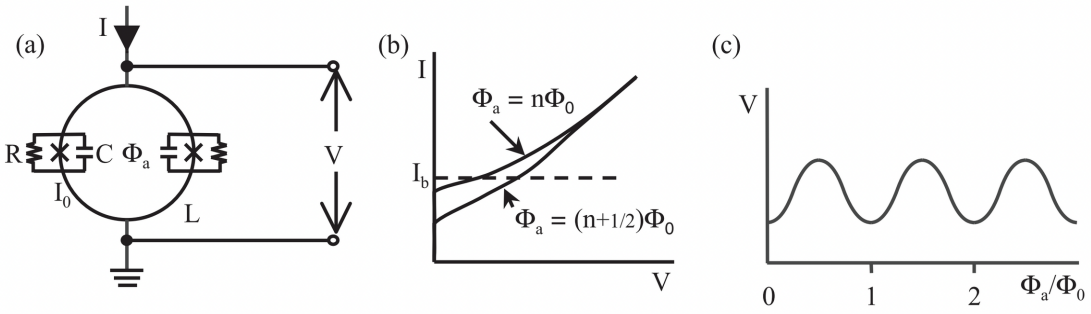

Figure 4-4: Figure 1.3 from [122], (a) depicts a basic DC SQUID, (b) $I-V$ characteristics for integer and half integer values, (c) voltage response of the SQUID to small changes in flux.

Noise in a DC SQUID is dominated by "flicker" or $1/f$ noise at frequencies below 0.1 Hz, thermal noise is also present, resulting from the resistors in the circuit, $S_I(\omega) = \frac{2k_BT}{\pi R}$. Thermal noise has no time correlation and presents as white noise. In addition to cooling for mitigation of thermal noise, SQUIDs must be kept under the critical temperature of 4.2 K to maintain Josephson coupling. At this temperature the noise floor of the SQUID is typically around 0.6 $\mu\Phi_0^2$/Hz.

SQUIDs in the ABRACADABRA-10cm detector

The DC Magnicon SQUIDs used in ABRA are operated below 4.2 K and follow the typical noise floor for DC SQUIDs. The SQUID noise floor can be affected by mechanical vibrations at frequencies below 100 Hz, but the SQUID noise resulting from vibrations is still well below the experimental noise floor [122]. In practice, the SQUID noise floor varies over our frequency range and thermal cycles of the dilution refrigerator. Flux can become trapped in the SQUID loops, which can be released by a brief controlled heating, but the SQUID parameters, such as the bias current, are prone to shifting slightly in value through thermal cycles.

While both of our SQUIDs are two-stage DC Magnicon SQUIDs, one of the SQUIDs has both stages integrated onto one chip, while the other SQUID has the two stages on separate chips in separate niobium casings, connected by a wire connector. We attempted to shield this connection electromagnetically by providing a small Faraday cage in the form of tin foil, but the separated SQUID still has a higher noise floor than the integrated SQUID. The integrated SQUID was used for data collection

in Runs 1-6, and the separated SQUID was used in addition to the integrated SQUID in Runs 4-6.

We operate the SQUIDs in FLL mode with a feedback resistance between 10 kΩs to 100 kΩ, dependent on the noise level in the system at the time of data collection. For Run 1 the SQUID flux-to-voltage conversion gain in FLL mode was $\partial V/\partial \Phi_S = 1.29\, V/\Phi_0$, while in Run 3 it was increased to 4.3 V/Φ_0, decreasing the system noise. This increase was possible as a result of decreasing the length of the twisted pair connecting the pickup structure to the SQUIDs, decreasing the inductance into the SQUID. The decrease in length of the twisted pair was achieved by moving the integrated SQUID down to the MC plate from the Still plate where it had sat for Run 1, decreasing the temperature of the SQUIDs from $\approx$ 870 mK to $\approx$ 450 mK, subsequently also decreasing the thermal noise floor [120]. The integrated SQUID was kept on the MC plate for Runs 2-6, and for Run 6 the separated SQUID was also moved down to the MC plate.

4.2.3 Readout

The SQUID current sensors were operated with Magnicon XXF-1 electronics in FLL mode and the signal was read into the computer by an Alazar 9870 8-bit digitization board. The Magnicon electronics consist of a steel-mesh-wrapped coaxial cable that runs from the current sensor on the MC plate, to the SQUID box at room temperature which reads the signal. At each cold stage the Magnicon wires are well-thermalized to the cryostat plates. The bandwidth of the SQUIDs is limited to 6 MHz by the dynamic range of the amplifier which is $\pm 11V$ and is linear over the bandwidth [32], but the SQUIDs were not the fundamental limit to the high-end of our frequency range.

The Alazar digitizer has a maximum sampling rate of 10 MS/s, limiting the top of our frequency range to the Nyquist frequency of 5 MHz. To prevent aliasing from higher frequencies, we use a 5 MHz low-pass filter, which has a transition band of about 2 MHz, limiting our science range to around up to 3 MHz. The low-pass filter roll-off limited the highest frequencies measurable in all our campaigns. Either a 10 kHz or 70 kHz high-pass filter is used on the low-frequency end of our spectrum to mitigate noise.

The digitizer is typically run with the lowest voltage range possible, the lowest range the digitizer can achieve is $\pm$ 40 mV resulting in a digitizer noise floor around 3.5×10^{-9} mV^2/Hz [32]. In many campaigns, particularly with the use of the second SQUID in separated stages, the noise on the digitizer was high enough that we had to collect data with a larger voltage window. Run 6 was taken with a range of $\pm$ 200 mV resulting in a digitizer noise floor around 7×10^{-8} mV^2/Hz. Section 4.5 describes the data acquisition methods used to process the data from the digitizer.

4.3 Calibration

The calibration system is setup to test the detector response to an axion-like signal for Runs 1-6 and an additional GW-like signal for Run 6. For an axion signal calibration, we inject an AC current into a loop located inside the magnet to mimic an oscillating axion current and we read that signal with the detector pickup structure. The GW signal is mimicked by a semi-circular figure-8 loop of the same form as the GW pickup 1 cm above the pickup in the final configuration of Run 6.

Figure 4-5 has a schematic of the calibration system from Runs 2-5 and Run 6. For a Run 2-5 science data collection configuration, the signal generator is used for active feedback to cancel out low frequency noise[120], see section 5.3.2 for more details. A Run 1 and Run 4-6 science data collection configuration has 50 Ohm terminators on both calibration ports, while Runs 2-3 only terminate the unused calibration port. See section 6.3 for more details on the complications of the Run 6 calibration with two different calibration circuits corresponding to the two pickups. Various attenuators are placed throughout the system to decrease the amount of power deposited onto the cold stages of the fridge during calibrations and to attempt to more closely mimic the small size of the axion or GW signal. See the circuit diagram for the attenuators listing and placement.

Calibrations are taken before and after science data collection, for both magnet on and off data collections. These calibrations are used to check our understanding of the system by comparing the data collected to estimated values of the gain of the system. The estimated gain is always larger than the measured gain as a result of unaccounted for parasitic inductances and the general principle that hardware has inherent complications and losses.

The data collected from a calibration is generally in the form of the gain of the amplitude of the signal from the signal generator to the amplitude measured on the digitizer,

$$\frac{V_{\mathrm{ADC}}}{V_{\mathrm{Sig}}} = \frac{V_{\mathrm{ADC}}}{V_{\mathrm{SQUID}}} \frac{V_{\mathrm{SQUID}}}{V_{\Phi_p}} \frac{V_{\Phi_p}}{I_C} \frac{I_C}{V_{\mathrm{Sig}}} \tag{4.5}$$

where V_{ADC} is the RMS voltage on the digitizer, V_{Sig} is the voltage output by the signal generator, V_{SQUID} is the measured on the SQUID, V_{Φ_p} is the voltage on the pickup loop and I_C is the RMS current entering the calibration loop. The first term is given by the attenuators and warm filters in the system, the third term is the mutual inductance between the calibration loop and the pickup structure, found by simulation, similarly to the first term, the last term is given by physical attenuators and the second term can be solved for.

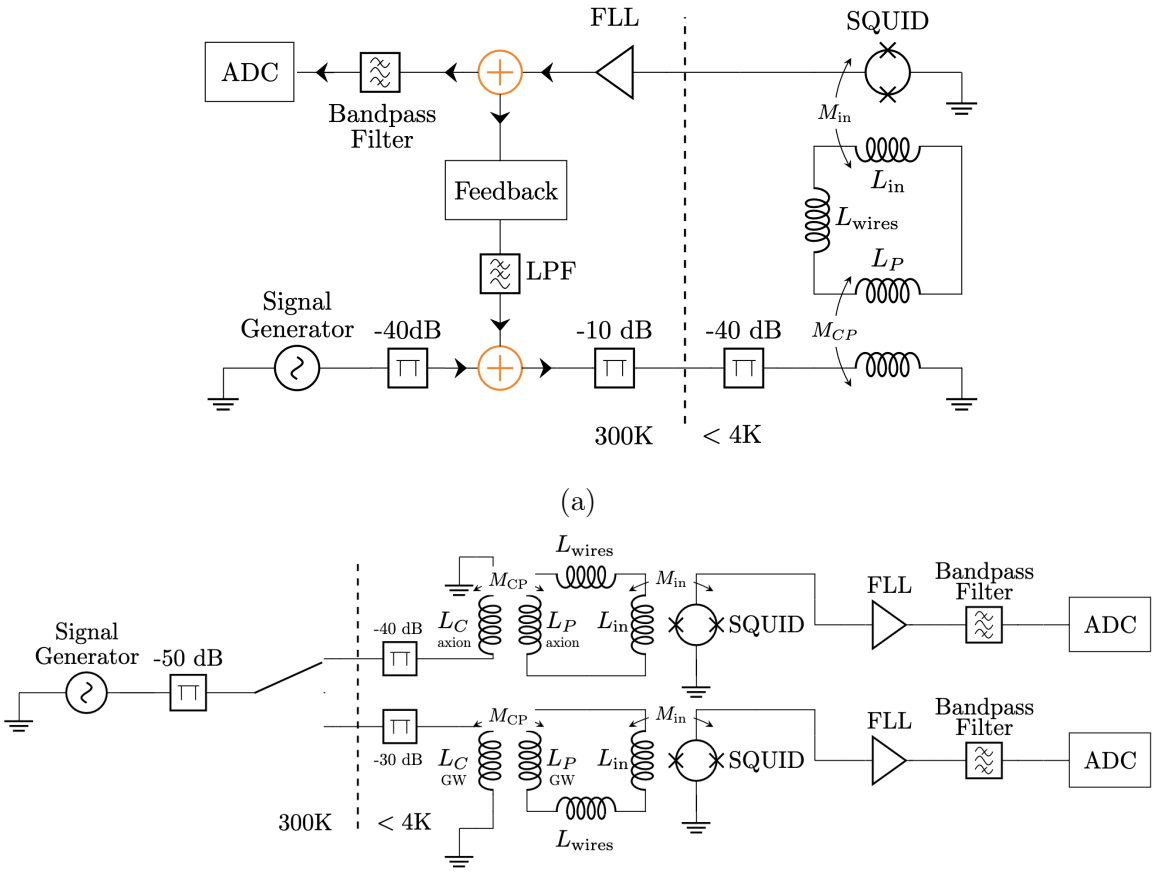

Figure 4-5: (a) The basics layout of our calibration system for Runs 2-5, the divide between the warm and cold parts of our system is marked by the dotted line, adapted from [120]. More information on the feedback system is given in section 5.3 and descriptions of filters are included in the text. (b) The basics layout of our calibration system for Run 6, the top circuit is used for calibrating the axion pickup loop, and the bottom circuit for the GW pickup. A calibration signal was only placed on one calibration loop at a time, represented by the switch between the signal generator and the fridge.

4.4 Data Acquisition System

Data was collected and saved in a series of averaged power spectral densities (PSDs) as well as in the raw time series (TS) form. The raw TS data was used in the GW analysis, correlation analysis in background identification campaign, and to detect instances where the signal exceeded the range of our digitizer which result in railing. The averaged PSDs are formed from squared fast Fourier transforms and have units

of mV^2/Hz.

4.4.1 Collecting Time Series

Time series data contains the maximal amount of information possible in our system, it is the raw output of the digitizer. Ideally, we would only save TS data, since the PSDs can be made from TS but the creation of the PSDs loses the phase information and the data cannot be transformed back to its TS form. However, since TS is so information dense, the files after a science run are large relative to our computer storage. In cases where we don't need the phase information and our signal is relatively stationary, it makes the most sense to save the data as averaged PSD to reduce storage size. When there is a specific need for TS data, especially on multiple channels, the process for collecting TS data needs compression and more efficient methods for saving files. The greater efficiency is needed to allow the system to take continuous data while also compressing the data and saving that compressed data. The data compression we've used relies on grouping like-values, which means the noisier the data, the less compressible it becomes. This effect is seen very clearly in that our files with the digitizer unplugged are about a tenth of the size of the science data files with the SQUIDs connected.

Sections of the background identification campaign data were taken simultaneously with an accelerometer, in this case the phase information is needed to perform a correlation between the two data sets. In addition, we were particularly interested in which noise resulted in an excess of the range of the digitizer (railing), which can clearly be seen in TS data as a maximal voltage value in a bin but cannot be distinguished once an FFT has been performed.

Run 6 has a transient search for the GW search data, which means the data cannot be averaged on large time scales relative to the signal. The amount of allowed averaging is defined by the duration time of the signal, the data can be averaged for as long as the signal is present and constant in frequency, otherwise averaging will reduce the signal amplitude. Post-data taking the raw data is filtered and down-sampled, but at the time of collection we did not anticipate the need for down-sampling and collected the maximum amount of data possible. Both channels were collected as TS data, while the axion data could have theoretically been collected in PSDs, the computer did not have enough memory to be continuously streaming data on one channel and preforming FFTs on the other.

4.4.2 Collecting PSDs

Power spectral density construction is flexible, and depending on the use of the PSDs they can be customized for the analysis preformed. The sampling rate determines the maximum frequency that can be measured by finding the Nyquist frequency. The frequency step is determined by the sampling rate and the length of the data being

transformed, $\Delta f = 1/T$ where T is the length of the data in seconds. For the axion campaigns, the resolution of the axion signal determined the minimum required Δf, see Chapter 5 for more axion analysis details.

The axion campaign PSDs were built in two different data streams, both were built while continuously sampling data [32, 120]. The first stream preformed an FFT on 10 seconds of data at a time to get the PSDs, then averaged 80 PSDs together to get an average over 800 seconds. This first stream is referred to as $\mathcal{F}_{10\mathrm{M}}$ as it uses a sampling rate of 10 MS/s with a Nyquist frequency of 5 MHz, shown in Figure 4-6. The frequency resolution of the $\mathcal{F}_{10\mathrm{M}}$ data is 100 mHz and was used in Runs 1 and 3 to evaluate frequencies from 500 kHz to 2 MHz in the axion analysis. The second stream down sampled the data by 10 to get a Nyquist frequency of 500 kHz, taking 100s of data in each PSD, 16 PSDs are averaged over 1600 seconds. The $\mathcal{F}_{1\mathrm{M}}$ data has a resolution of 10 mHz and was used to analyzes frequencies from 50 Hz to 500 kHz [32, 120]. For the background identification campaigns the frequency resolution did not have to be as fine for analysis. The PSDs taken were primarily 1 second long at a sampling rate of 10 MS/s.

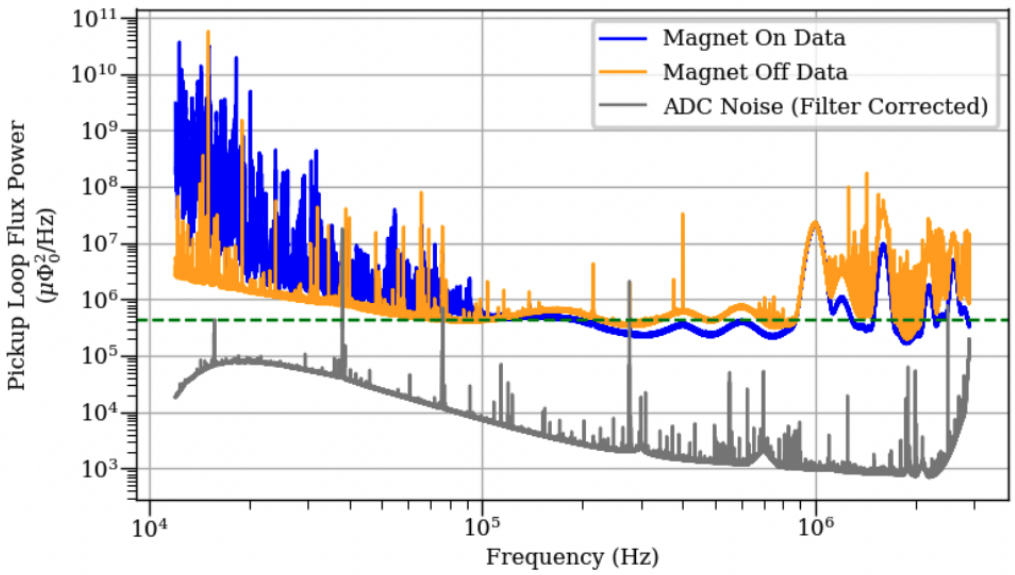

Figure 4-6: Adapted from [32], depicting an example of the $\mathcal{F}_{10\mathrm{M}}$ data collected for the magnet both charged and discharged averaged over ≈ 9 hours. The digitizer noise floor is also included, which was averaged over ≈ 16 hours.

The ABRA detector has served as the first-ever pathfinder experiment for two different lumped-element searches for low-mass axions, and then was adapted for use of HFGW detection, which in turn was the first-ever modification of an axion detector for the purpose of detecting GWs. With a conceptually simple setup of a magnet, a loop wire and a current sensor, ABRA has achieved many scientific goals and has been a pioneer in small signal searches.

Chapter 5

First Runs of ABRACADABRA-10cm and Noise Characterization

The axion search campaigns of ABRA include Runs 1-3 and 6. Runs 1-3 searched for axions at the GUT scale in the mass range of 0.3 to 8 neV, reaching below the CAST and setting world-leading limits with Run 3. Run 1 was the first published lumped-element search for axions, it used a loop of superconducting wire to inductively couple to the axion signal. To improve coupling to the axion signal, Runs 2 and 3 used a superconducting cylinder to replace the loop of wire and increase the mutual inductance to the signal, and therefore the geometric coupling constant $\mathcal{G}_V$, which is directly proportional to the signal to noise ratio shown in equation (4.1). This increased sensitivity to the axion signal also resulted in an increase of noise, which inspired the background identification campaign, Runs 4 and 5, which were dedicated to understand noise sources in a cryogenic axion detector. The numbering of the runs mark major hardware changes, changes in goal, and the passage of time. Run 2 was not calibrated so the data was used for testing the analysis framework and was not used to publish limits. Run 3, which had the same geometry and science goal as Run 2, was properly calibrated and was used to publish limits in [120]. Runs 4 and 5 only differ in the year in which data was collected, Run 4 data was taken in 2020 and Run 5 data was taken in 2021. Run 6 is the axion and GW search campaign, which necessitated a major hardware change, more on Run 6 in Chapter 6.

The first section of this chapter is an overview of the axion analyses done in Runs 1-3. The second section consists of a re-calculation of the method for finding the geometric constant used in the axion searches for Runs 1 and 3, focusing on the Run 1 value. Originally, we thought we would need a geometric constant for Run 6 before we figured out a different method for accounting for the detector geometry, which lead to the work in the $\mathcal{G}_V$ section. The third section describes the backgrounds in ABRA which increased as a result of the cylindrical pickup in Run 3, how that noise

was dealt with in Run 3, and the findings from the background identification and mitigation from Runs 4 and 5.

5.1 Overview of Axion Analysis

The goal of the ABRA Run 1 and 3 analyses were to search for an axion signal and set limits on $g_{a\gamma\gamma}$ as a function of the axion mass where one wasn't found. Both searches were broadband and collected data for around a month. The following section is based on the work done in [123], [120] and [32] focusing on the techniques used in Run 1. The Run 3 analysis differed by adding a more in-depth veto system and a better understanding of certain noise features.

The analysis for ABRA Runs 1 and 3 starts with an analytic description of the field of an individual axion or ALPs in our galaxy indexed by i, with $i \in 1, 2, ..., N_a$,

$$a_i(\nu, t) = \frac{\sqrt{2\rho_{\mathrm{DM}}/N_a}}{m_a} \cos\left[m_a\left(1 + \frac{\nu_i^2}{2}\right)t + \phi_i\right] \tag{5.1}$$

where ρ_{DM} is the local dark matter density, valued at 0.4 GeV cm^{-3}, N_a is the total number of axion particles, m_a is the axion mass, ν_i is the velocity of the individual axion and ϕ_i is the phase of that particle which is randomly distributed. The individual axion field is summed over for axions with like velocities and this axion distribution ($a(t)$) is used to determine the magnetic flux on the pickup loop,

$$\Phi_{\mathrm{pickup}}(t) = g_{a\gamma\gamma} B_{\mathrm{max}} \mathcal{G}_V V m_a a(t). \tag{5.2}$$

Where $g_{a\gamma\gamma}$ is the axion to two photons coupling constant discussed in Chapter 2, B_{max} is the peak magnetic field reached in the toroidal volume of the magnet, V is the volume of that total magnetic field and $\mathcal{G}_V$ is the geometric coupling constant discussed in the next section of this chapter. By taking the magnitude of the flux we can define the signal strength A,

$$|\Phi_{\mathrm{pickup}}|^2 = g_{a\gamma\gamma}^2 \rho_{DM} V^2 \mathcal{G}_V^2 B_{\mathrm{max}}^2 \equiv A. \tag{5.3}$$

The flux on the pickup is read out by the SQUIDs, which also measures flux,

$$\Phi_{\mathrm{SQUID}} \approx \frac{\alpha_S}{2}\sqrt{\frac{L}{L_p}}\Phi_{\mathrm{pickup}}, \tag{5.4}$$

here L is the inductance of the SQUID, L_p is the inductance of the pickup loop and α_S is a characteristic constant of the SQUID geometric coupling to the pickup, typically having a value of $1/\sqrt{2}$. In practice, there are many more inductances which affect the measured flux from the pickup loop, including parasitic inductances from the wires throughout the system, from the twisted pair which connects the pickup loop to the SQUID, to the wires of the SQUID readout. These inductances and other

experimental factors are accounted for with calibration. Run 1 measured a total inductance of the circuit of around 3.3 μH, an order of magnitude higher than the predicted total inductance of around 550 nH.

Equations (4.2) and the summed form of (4.1) can be combined to find the flux on the pickup loop taken over a collection period of $n\Delta t$, represented by Φ_n. The time step Δt is the spacing between data points, with $\Delta t = 1/f$, and $n \in 0, 1, ..., N-1$ marks the measurement time of each data point. The flux on the pickup is Fourier transformed and squared to get a PSD, $\mathcal{F}_k$ at a frequency of $f_k = k/T$ for frequency bin $k \in 0, 1, ..., N-1$. The frequency step of $\mathcal{F}_k$ is $\Delta f = 1/T$ where T is the experimental run time, or the length of time of the time series data collected for and used to form the PSD. As discussed in the previous chapter, the data is collected in chunks which are transformed and averaged together, the different lengths of collection mark different resolutions of frequency spacing.

The coherence time of the axion signal is given by $1/(f\nu_0^2)$, where $\nu_0 = 220$ km/s is the velocity dispersion of DM in the standard halo model (SHM), and the coherence time has a value of around 1 second for a MHz. To search for each individual mass point a frequency window was establish of $f_{k_i(m_a)} = m_a/(2\pi)$ to $f_{k_f(m_a)} = (1 + 4\nu_0^2) f_{k_i(m_a)}$. This window is approximately eight times larger than the expected width of the axion signal, given by $\Delta f/f \sim 10^{-6}$.

As a result of the random phase in the axion distribution, $\mathcal{F}_k$ is exponentially distributed. The background is assumed to be Gaussian distributed and locally independent in the time domain over the window of data used to take each PSD, which also translates to an exponential distribution once the PSD of the background is taken. The averaged independent PSDs of $\bar{\mathcal{F}}_k$ and $\bar{\mathcal{F}}_{\text{background}}$ are Erlang distributed,

$$P(\bar{\mathcal{F}}_k; N_{\text{avg}}, \lambda_k) = \frac{N_{\text{avg}}^{N_{\text{avg}}}}{(N_{\text{avg}}-1)!} \frac{(\bar{\mathcal{F}}_k)^{N_{\text{avg}}-1}}{\lambda_k^{N_{\text{avg}}}} e^{-\frac{N_{\text{avg}}\bar{\mathcal{F}}_k}{\lambda_k}} \tag{5.5}$$

for N_{avg} averages and $\lambda_k = s_k + b$, where

$$s_k = \begin{cases} A\frac{\pi f(\nu)}{m_a \nu}, & f_k > m_a/2\pi, \\ 0, & f_k \leq m_a/2\pi \end{cases}$$

b is the background power, $\nu = \sqrt{4\pi f_k/m_a - 2}$ and $f(\nu)$ is the local velocity distribution of DM as dictated by the SHM. The background over the total science collection time will likely not remain stationary, to account for this drift the background values are defined as $\mathbf{b} = \{b_1, b_2, ..., b_{\mathcal{N}}\}$, these values are treated as nuisance parameters. The signal strength will not vary with time in the SHM.

The likelihood of the data $\mathbf{d}$ for a background of $\mathbf{b}$ is given by

$$\mathcal{L}(\mathbf{d}_{m_a}|A, \mathbf{b}) = \prod_{j=1}^{\mathcal{N}} \prod_{k=k_i(m_a)}^{k_{f(m_a)}} P(\bar{\mathcal{F}}_{j,k}; N_{\text{avg},j}, \lambda_{j,k}) \tag{5.6}$$

with j indexing the different spectra and allowing for the individual spectra to have different numbers of averages. Using Wilks' theorem, a likelihood ratio test is used to search for the axion signal with a log-likelihood ratio as the test statistic (TS).

$$\mathrm{TS}(m_a) = 2\ln\left[\frac{\mathcal{L}(\mathbf{d}_{m_a}|\hat{A},\hat{\mathbf{b}})}{\mathcal{L}(\mathbf{d}_{m_a}|\hat{A}=0,\hat{\mathbf{b}}_{A=0})}\right] \tag{5.7}$$

with $\hat{A}$ and $\hat{b}$ as the values which maximize the global likelihood, and the denominator representing the null hypothesis, where there is no signal ($A = 0$) and the background maximizes the likelihood with respect to no signal ($\hat{\mathbf{b}}_{A=0}$). A is maximized for a range of parameter values and A is allowed to take a negative value. A negative value of A is not physically possible, it is interpreted as $\mathrm{TS}(m_a) = 0$, and the null hypothesis is found true. To determine a signal detection, a 5σ threshold for discovery is given by $\mathrm{TS}(m_a) > \mathrm{TS}(m_a)_{\mathrm{thresh}}$ with

$$\mathrm{TS}_{\mathrm{thresh}} = \left[\Phi^{-1}\left(1 - \frac{p}{N_{m_a}}\right)\right]^2, \tag{5.8}$$

where Φ is the cumulative distribution function of the normal distribution and N_{m_a} is the number of mass points searched for. N_{m_a} is determined analytically to be

$$N_{m_a} = \frac{3}{4\nu_0^2}\ln\frac{f_{\max}}{f_{\min}} \tag{5.9}$$

where the constant of 3/4 was determined by comparing the analytic form to Monte Carlo simulation. The look-elsewhere effect is accounted for in this analysis by assuming the background could fluctuate and create a signal with a probability $p = \Phi(N)$ for $N\sigma$ significance, for an N of 5 $p = 2.87 \times 10^{-7}$. Run 1 had around 8.1×10^6 mass points, giving $\mathrm{TS}_{\mathrm{thresh}} = 56.1$, and Run 3 had around 11.1×10^6 mass points, giving $\mathrm{TS}_{\mathrm{thresh}} = 55$.

The survival function under the null hypothesis is the probability that the background produces a significant signal, and is given by

$$S(\mathrm{TS}(m_a)) = 2\left(1 - \Phi\left(\sqrt{\mathrm{TS}(m_a)}\right)\right), \tag{5.10}$$

and the presents of an axion would produce a slight deviation from this distribution. Transient noise that produces many correlated peaks in a spectrum creates a clearly distorted distribution, and quality cuts can be made for averaged PSDs with an excess of 30 mass points with over 3σ significance. In Run 1 these transient noise cuts removed around $\approx 30\%$ of the exposure but did not affect the single-mass axion search.

The data is farther processed by using Magnet off data to veto any possible signal that appears without the presents of a magnetic field. Additionally, Run 3 had a data cleaning procedure which removed narrow spectral features which presented

often as single-bin excesses and peaks which shifted in frequency over time. The stationary peaked noise features result from sources like AM radio stations and do not perfectly mimic an axion signal which has a distinct shape over multiple bins, however these features do look more like the signal than a flat background. Figure 5-1 shows the survival fraction of events from the Run 3 analysis, where the survival fraction represents the faction of mass points which have a TS which maximize A at or over the corresponding TS value on the x-axis.

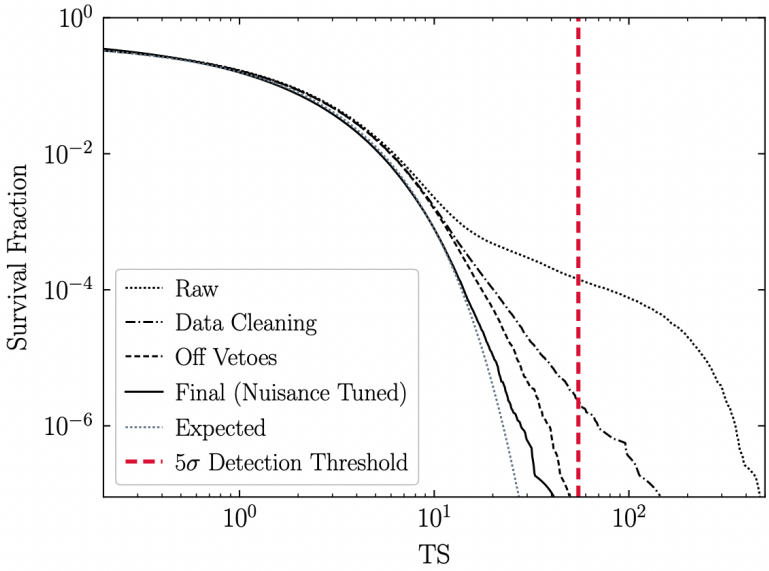

Figure 5-1: Adapted from [120]. The survival fraction of TS values for Run 3, shown with different vetoes and cuts applied.

Runs 1 and 3 did not discover an axion-like particle, and were able to place an upper limits for $g_{a\gamma\gamma}$ at a 95% confidence level for each mass point tested. The TS for placing limits is given by

$$q(m_a, A) = \begin{cases} 2\ln\left[\frac{\mathcal{L}(\mathbf{d}_{m_a}|\hat{A},\hat{\mathbf{b}})}{\mathcal{L}(\mathbf{d}_{m_a}|\hat{A},\hat{\mathbf{b}}_A)}\right], & A \geq \hat{A}, \\ 0, & \text{otherwise.} \end{cases}$$

Much like for equation (5.7), $\hat{\mathbf{b}}_A$ represents the background which maximizes the likelihood for a value of A. The upper limit is found by using a background only model with $q(m_a, A_{95\%}) = 2.71$. As was done for the discovery search, $\hat{A}$ is again allowed to take negative values. One-sided power-constrained limits are constructed which restrict the strength of the limit to 1σ above the 95% confidence level.

The axion searches of ABRACADABRA-10cm demonstrated the ability to search for axions with a lumped-element experiment, and Run 3 set limits on $g_{a\gamma\gamma}$ extending past the CAST limit, excluding previously empty parameter space. While Run 3 set

stronger limits than Run 1, it had a slightly reduced mass range as a result of noise, this reduction is explored in the last section of this chapter.

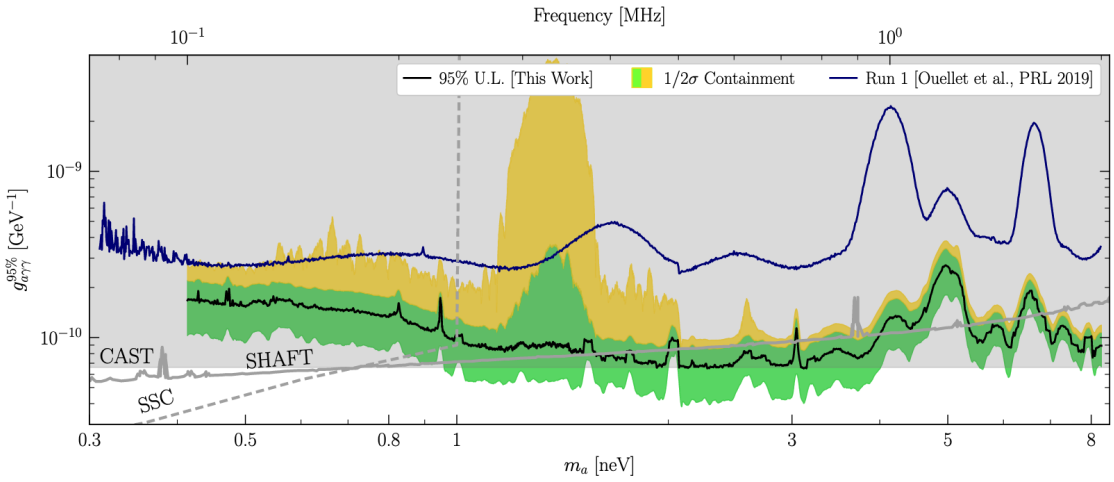

Figure 5-2: The limits placed on $g_{a\gamma\gamma}$ from Run 3 and Run 1 for the given axion mass range. The one-sided upper limit is shown for the Run 3 analysis. "This work" refers to [120], from which this figure was adapted.

5.2 Geometric Constant $\mathcal{G}_V$

$\mathcal{G}_V$ is the geometric constant which describes how the axion signal couples to the ABRA detector. This constant is needed to characterize the detector response to the axion signal and is used in addition to the calibration data. The calibration signal is created from a loop of wire and cannot account for the shape of the axion effective current, which is a current density filling the volume of the magnet. To find $\mathcal{G}_V$, the axion current is simulated through the magnetic volume and the pickup response is measured. The documentation was insufficient to reproduce the $\mathcal{G}_V$ results from Runs 1-3, this section describes different methods that could be used to recreate the Run 1 [32, 33] and Run 2-3[120] values. This re-calculation was initiated when we thought we might need a $\mathcal{G}_V$ for Run 6 and had to confirm we could reproduce the results from Run 1, which has a very similar geometry as the Run 6 axion search. In our initial calculations of $\mathcal{G}_V$, we had trouble recreating the published values. To find the source of the discrepancy, we found $\mathcal{G}_V$ for Run 1 using two different methods and different combinations of possible variable values for each method, resulting in 16 different calculations of $\mathcal{G}_V$. Out of these 16 calculations four of them matched the published value and lead us to believe an incorrect volume was used to find the published value of $\mathcal{G}_V$.

$\mathcal{G}_V$ provides a relationship between a theoretical axion current and the current on the pickup loop. The magnitude of axion effective current produced is directly related

to the magnetic volume, as the DM density is locally homogeneous. Analytically, $\mathcal{G}_V$ takes the form of

$$\mathcal{G}_V = \frac{1}{B_{\max} V} \left| \int_{\text{Loop}} dA \int_{\text{Toroid}} dV' \frac{\mathbf{B}(\mathbf{r}') \times (\mathbf{r}' - \mathbf{r})}{|\mathbf{r}' - \mathbf{r}|^3} \cdot \hat{\mathbf{n}} \right|, \tag{5.11}$$

where V is the magnetic volume of the detector and $\mathrm{B}_{\max}$ is the maximum value of the magnetic field, the volume integral is taken over the toroidal DC magnetic field volume, the surface integral is taken over the pickup loop area and $\hat{\mathbf{n}}$ is normal to that pickup loop area. This analytic form is very difficult to evaluate given the non-rectangular toroidal shape of the magnet, which makes simulation necessary for a more accurate calculation of $\mathcal{G}_V$.

As shown in the following calculations, it appears as though Runs 1-3 simulated the magnetic volume over the volume of the mandrel, likely over-estimating the magnet volume. A more likely accurate estimate for the magnetic volume would be to set the magnetic volume boundary as half-way through the wire winding, from here on referred to as the mid-winding volume. The length from the inside of the winding to the outside is about a 5 mm. In addition, the calculation of the magnet volume in the PRD is less than the actual value, we found the smallest possible value of the volume to be 917 cm^3 from COMSOL (measuring from the inside of the winding), while in the PRD the value is listed as 890 cm^3. In the following attempts there are multiple sets of COMSOL results with two volumes used in the simulation, one with the axion current filling the mandrel volume (1190.6 cm^3) and the other using the axion current filling the magnet mid-winding volume (1069.2 cm^3). The post-simulation calculations are also done both with the volume as calculated by COMSOL, and the volume listed in the PRD. See appendix A for COMSOL simulation specifics.

There are two volumes listed throughout the text, in a correct scenario this two volumes would be equal, as they both represent the volume of the magnet. However, as we discovered that we could not recreate the published values for $\mathcal{G}_V$, we experimented with using one value to define the volume of the magnet in the simulation (the value input to COMSOL as referenced in the text) and a different value as the variable "V" when solving for the final $\mathcal{G}_V$ in equations (5.17) and (5.22), referenced as the post-simulation calculation.

5.2.1 Method 1: using the current ratio

The first method used to calculate $\mathcal{G}_V$ finds the current ratio between the integrated axion effective current and resulting pickup current from the simulation. We start with [32] equation (3) which describes the flux resulting from an axion signal in the detector,

$$\Phi = g_{a\gamma\gamma} \sqrt{\rho_{DM}} \mathrm{V} \mathcal{G}_V \mathrm{B}_{\max}. \tag{5.12}$$

Additionally, we can calculate the flux in terms of M, the mutual inductance between the axion effective current and the pickup loop,

$$\Phi = \mathrm{MI_{tot}} = \mathrm{M}\int \mathrm{J_{eff}dA}, \tag{5.13}$$

with I_{tot} as the integrated axion effective current and $\mathrm{J_{eff}}$ as the axion effective current. Combining equations (5.11) and (5.12) we get

$$\mathrm{M}\int \mathrm{J_{eff}dA} = \mathrm{V}\mathcal{G}_V\mathrm{J_{max}} \tag{5.14}$$

where

$$\mathrm{J_{max}} = g_{a\gamma\gamma}\sqrt{\rho_{DM}}\mathrm{B_{max}}. \tag{5.15}$$

Solving for $\mathcal{G}_V$,

$$\mathcal{G}_V = \frac{\mathrm{M}}{\mathrm{V}}\left[\int \frac{\mathrm{J_{eff}dA}}{\mathrm{J_{max}}}\right]. \tag{5.16}$$

Inserting the equation for the mutual inductance between the axion current and the pickup loop, switching for an equivalent integral and adding a constant for units the final form of $\mathcal{G}_V$ is

$$\mathcal{G}_V = \frac{1}{\mu_0\mathrm{V}}\frac{\mathrm{I_p}}{\mathrm{I_a}}\mathrm{L_p}\left[\int \frac{\mathrm{R_{in}dA}}{\rho}\right]. \tag{5.17}$$

Where $\mathrm{R_{in}}$ is the inner radius of the magnet, valued at 30 mm, and ρ is the cylindrical radial coordinate. The effective axion current used in the magnet volume was based on the current in the magnet (121 [A]) and the number of winding (80*16) with a 1/r dependence,

$$\mathrm{J_{eff}} = 4\pi * 121 * 80 * 16/(2\pi * r). \tag{5.18}$$

We use COMSOL to find the current ratio and solve for the integral over the magnet volume. Since this calculation relies on the current in the pickup, a frequency-based study is used. To mimic superconductivity, the boundary of the pickup loop was set to have a conductivity 18 order of magnitude greater than that of normal copper, see Appendix A for more details. The following calculations were done for a Run 1 geometry to be able to directly compare with the value found for Run 1, which published a $\mathcal{G}_V$ value of 0.027.

Note on interpreting tables 5.1-3: for the calculation of current through a cross section in COMSOL there are multiple options, the two listed in the tables below are "current density norm" and "current density, ϕ component". Norm in this case is slightly misleading, it is not the normal to the surface as one might think, but the normalization over the surface. For this reason, we trust the single component results more, but both are used in calculating $\mathcal{G}_V$ as we were searching for the cause of anomalous published values. $\mathcal{G}_V$ is calculated using equation (5.17) for both values of the current over the two values of V, the volume found by COMSOL and the PRD volume. Here "COMSOL volume" refers to the volume through which the axion

effective current was simulated, it is the same value as listed in the "Volume" row of the tables. The "$\mathcal{G}_V$ for ..." rows use the "Volume" value to evaluate (5.17).

Table 5.1 simulates the mandrel magnetic volume with a 3D simulation. Using the ϕ-component of the current density and the PRD volume in the post-simulation calculation we come close to the PRD value for $\mathcal{G}_V$, the error of which can likely be attributed to the simplifications of the geometry for the 3D simulation (see appendix A). Since the mandrel volume is likely an overestimate of the magnetic volume, and the PRD volume does not match the volume found in COMSOL, this result is likely unphysical.

Table 5.2 presents a more physical setup, using the mid-winding volume. The result for the norm of the current and post-simulation calculations with the PRD volume seems to recreate the published Run 1 value. The most physical result in table 5.2 would be for the ϕ component of the current density and using the COMSOL volume for post-simulation calculations, resulting in a $\mathcal{G}_V$ value of 0.019.

Table 5.3 uses an axi-symmetric simulation, which allows a more complicated geometry and the possibility to make the inside of the pickup loop superconducting as well (see appendix A). The simulation is likely the same as was used for the published result, Chiara Salemi sent the simulation over as the most updated version that was last used, and we ran it unaltered. The volume as calculated in COMSOL for the 2D axi-symmetric model matches the mandrel volume found in the 3D simulation. Using the PRD volume for post-simulation calculations and the ϕ component of the current density recovers the Run 1 published result.

Comparing the "$\mathcal{G}_V$ for ϕ comp" rows in tables 5.1-3, the values are fairly close in value, which seems to suggest that the exact value of the magnetic volume is not so significant as long as that same volume is used in the post-simulation calculations as was used for the simulation. This result for "$\mathcal{G}_V$ for ϕ comp" of around 0.0195 is the most physical of the current-based calculations, and about 72% of the published result.

While these current-based simulations are compelling, they rely on COMSOL correctly simulating the superconductivity of the pickup loop, which is not a function it was designed to simulate. The flux-based method for finding $\mathcal{G}_V$ in the next section only relies on the flux on the area of the pickup, so no physical pickup is required and superconductive properties do not have to be simulated.

Parameter	Value
Frequency	100 kHz
Volume	1190.6 cm^3
I_p norm of current	0.0003553 A
I_p ϕ component only	0.0003155
I_{axion}	0.0029802 A
$\int \frac{R_{in} dA}{\rho}$	0.0028863
$\mathcal{G}_V$ for norm	0.02196
$\mathcal{G}_V$ for ϕ comp	0.01950
$\mathcal{G}_V$ using PRD volume and norm	0.02937
$\mathcal{G}_V$ using PRD volume and ϕ	0.0261

Table 5.1: Current ratio method for solving for $\mathcal{G}_V$ using a 3D simulation and the mandrel volume as the input to COMSOL.

Parameter	Value
Frequency	100 kHz
Volume	1069.2 cm^3
I_p norm of current	0.00032862 A
I_p ϕ component only	0.00028172
I_{axion}	0.0026531 A
$\int \frac{R_{in} dA}{\rho}$	0.0025695
$\mathcal{G}_V$ for norm	0.0226
$\mathcal{G}_V$ for ϕ comp	0.019387
$\mathcal{G}_V$ using PRD volume and norm	0.0272
$\mathcal{G}_V$ using PRD volume and ϕ	0.0233

Table 5.2: Current ratio method for solving for $\mathcal{G}_V$ using a 3D simulation and the mid-winding volume as the input to COMSOL.

Parameter	Value
Frequency	100 kHz
Volume	1190.6 cm^3
I_p norm of current	0.00078848 A
I_p ϕ component only	-0.0003296
I_{axion}	0.0029802 A
$\int \frac{R_{in}dA}{\rho}$	0.0028863
$\mathcal{G}_V$ for norm	0.0487
$\mathcal{G}_V$ for ϕ comp	0.0204
$\mathcal{G}_V$ using PRD volume and norm	0.0652
$\mathcal{G}_V$ using PRD volume and ϕ comp	0.0272

Table 5.3: Current ratio method for solving for $\mathcal{G}_V$ using the mandrel volume. This simulation was done as a 2D-axisymmetric model.

5.2.2 Method 2: Flux based calculation

For the flux calculation the goal is to get $\mathcal{G}_V$ only in terms of flux and not current. First we use equations (5.15) - (5.17) to solve for J_{max},

$$J_{max} = \int JdA / \int \frac{R_{in}dA}{\rho}, \tag{5.19}$$

and plug that into [32] equation (3) to get

$$\Phi = V\mathcal{G}_V \int JdA / \int \frac{R_{in}dA}{\rho}. \tag{5.20}$$

If we use

$$J = \frac{R_{in}}{\rho}, \tag{5.21}$$

as our effective axion current (J_{eff}), the relationship between $\mathcal{G}_V$ and flux is now simplified to

$$\mathcal{G}_V = \frac{1}{\mu_0}\frac{\Phi}{V}. \tag{5.22}$$

We use the stationary solver in COMSOL to find the flux in the loop for a J_{eff}

of R_{in}/ρ in the ϕ direction. The area covered by the loop is defined by a surface and the z-direction of the magnetic field is integrated over that surface to find Φ_p. Similarly to tables 5.1-3, the "$\mathcal{G}_V$ for PRD volume" row refers to using the volume found in [32] to evaluate equation (5.22). The "$\mathcal{G}_V$" row uses the volume through which the axion effective current was simulated, which is listed in the "Volume" row, to evaluate (5.22).

Parameter	Value
Volume	1190.6 cm^3
Φ_p	3.0361 * 1e-11 Wb
$\mathcal{G}_V$	0.0203
$\mathcal{G}_V$ for PRD volume	0.02714

Table 5.4: Flux method for solving for $\mathcal{G}_V$ using the mandrel volume.

Parameter	Value
Volume	1069.29 cm^3
Φ_p	2.736 * 1e-11 Wb
$\mathcal{G}_V$	0.01692
$\mathcal{G}_V$ for PRD volume	0.02032

Table 5.5: Flux method for solving for $\mathcal{G}_V$ using the mid-winding volume.

The value for $\mathcal{G}_V$ using the PRD volume post-simulation calculations in table 5.4 recreates the published Run 1 result, providing farther evidence that the published result used the mandrel volume for simulation and the PRD volume for post-simulation calculation. This value is in agreement with the table 5.1 and 5.3 values for "$\mathcal{G}_V$ using PRD volume and ϕ comp". Between tables 5.4 and 5.5 the most physical result would be using the mid-winding volume for the simulation and post-simulation calculations, resulting in a $\mathcal{G}_V$ value of 0.017, about two-thirds of the published value for Run 1.

5.2.3 $\mathcal{G}_V$ Conclusions

Figure 5-3 summarizes all the $\mathcal{G}_V$ values found in tables 4.1-5. Strong statistical claims are difficult to make about the spread of $\mathcal{G}_V$ values since each value is calculated using different methods and input variables. Four of the re-calculated values closely matched the Run 1 published value, and it appears from these calculations that the Run 1 published value likely used the full mandrel volume as the magnetic volume for the simulation and the PRD volume as the magnetic volume for the post-simulation

calculation. The most logical method for calculation would use a consistent magnetic volume for both the simulation and post-simulation calculations. The results that have the most physical step up used the mid-winding volume, they are "Flux calculation and COMSOL volume" at 0.0169 and "ϕ component of current and COMSOL volume" at 0.0194. We reiterate that the fluxed-based calculations do not rely on COMSOL to simulate superconductivity, a function which COMSOL was not built to simulate. It is likely the true value of $\mathcal{G}_V$ is not smaller than 0.01692, and not larger than 0.0203, both values are from the flux calculation, the first using the mid-winding volume for simulation and calculation, and the second using the mandrel volume for simulation and calculation.

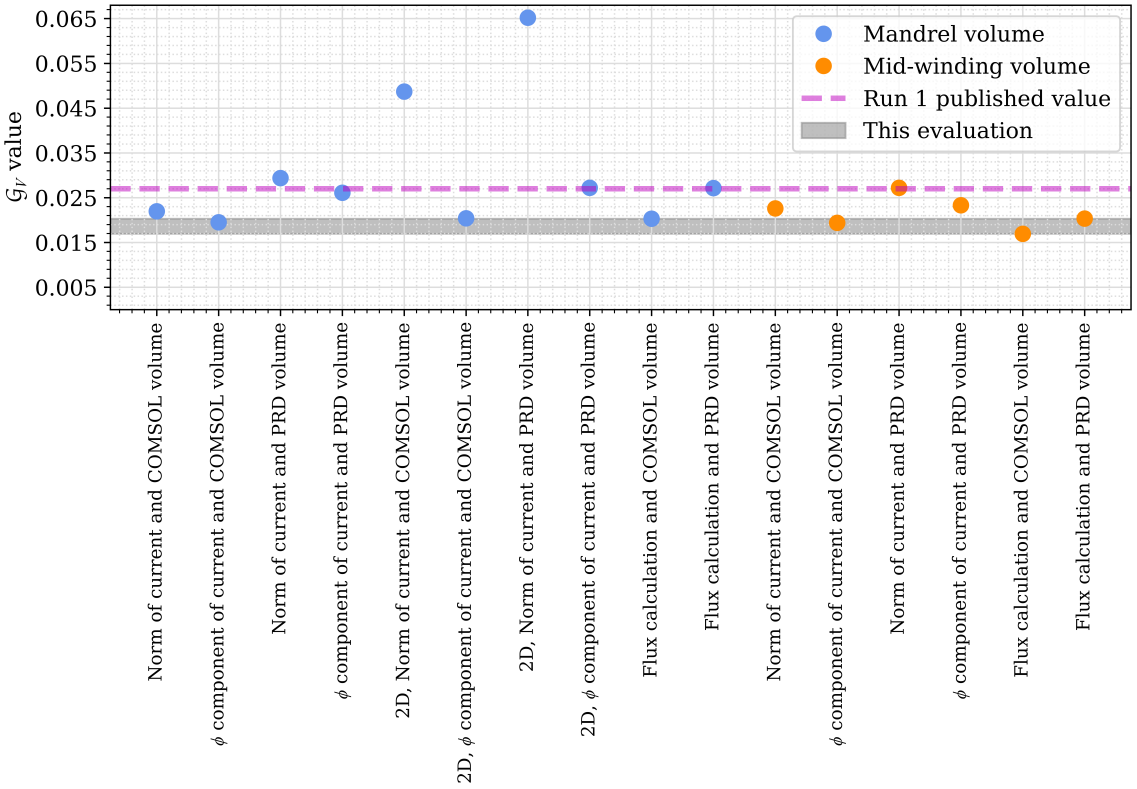

Figure 5-3: All the calculated $\mathcal{G}_V$ values from the tables in section 5.2. The x-axis lists the volume and pickup-current value which was used to evaluate $\mathcal{G}_V$ for the current-based solution (5.17), or the volume used to evaluate $\mathcal{G}_V$ for the flux-based solution (5.22). The gray band marking "This evaluation" shows the region in which we determined the value of $\mathcal{G}_V$ should lay based on the work in this chapter.

5.3 Backgrounds in ABRACADABRA-10 cm

For the background-search campaign of ABRA (Runs 4 and 5) we used the same cylindrical pickup setup as used in Run 3, which was more sensitive to the axion signal than the ring pickup from Run 1, but in turn also more sensitive to backgrounds. From Run 1 to Run 3 there was a reduction in measurable axion mass parameter space, from a lower limit of $m_a \sim 0.31$ neV (~ 75 kHz) to a lower limit of $m_a \sim 0.41$ neV (~ 100 kHz) as a result of noise increase. Unlike the data taken in Run 3, the majority of the noise tests were done without the use of the PID, which was used for active feedback to reduce the low-frequency noise in Run 3 [120].

In the following sections we discuss the increased sensitivity in Run 3 and the predominant noise features we encounter with ABRA and how they interfere with our data collection and signal detection. The features discussed are electromagnetic interference (EMI), vibrations and an artifact in our background at 70 kHz.

5.3.1 Sensitivity in Run 3

The cylinder used in Runs 2-5 had a higher coupling to the axion signal than the loop used in Run 1, increasing the published $\mathcal{G}_V$ value from 0.027 to 0.031[120]. We did not re-simulate and recalculate the value of $\mathcal{G}_V$ for the cylinder when we did the Run 1 recalculations since the axion geometry of Run 3 is fundamentally different from the axion geometry of Run 6. We have reason to believe the same methods used in the Run 1 published value were also used in the Run 3 published value, i.e. using the inflated magnet volume for simulation and the deflated magnet volume for post-simulation calculation. Given the similarity in methods, the scaling between Runs 1 and 3 are likely the same, which would put the Run 3 value for $\mathcal{G}_V$ around 0.023.

The noise increase with the addition of the cylindrical pickup affected all frequencies, but at low frequencies the amplification was enough to overwhelm the SQUIDs, rendering the data unusable and preventing data from being collected at any frequency initially. To combat this low-frequency noise for Run 3, we used a Stanford Research Systems SIM960 analog PID controller during the data collection for active feedback. The PID was connected to the signal generator, which in turn was connected to the calibration loop, and signals were injected at low frequencies to destructively interfere with the noise. Since this active feedback was limited to the low-frequency region, it did not interfere with the frequency range which was of scientific interest [120]. A 10 kHz low-pass filter was placed before the digitizer to attenuate these actively corrected low frequencies, see Chapter 4.4 Figure 4-3 for a circuit diagram of the setup. With the low frequencies attenuated, the data could be collected for Run 3, but there was still a need for passive noise reduction to increase the searchable axion mass range.

5.3.2 E and M Noise

In the winter of 2021, we conducted a series of tests to determine the sources and characteristics of electromagnetic noise in our system. The majority of these tests were conducted with the magnet uncharged, since the noise from the magnet dominates our backgrounds, especially at high frequencies. EM noise can enter our system directly into the pickup, or through our readout chain either through the body of the fridge into the cold components, or onto the electronics external to the fridge.

Our pickup structure is susceptible to EM noise entering through the body of our fridge from environmental sources, and EM noise from wires within the fridge itself. As a consequence of the short magnet charging wires which are not well thermalized, noise can easily travel through our system to the pickup via the magnet leads. Our leads act as antennae, picking up EM noise on the warm side, and carrying that noise down into our system. We experimented with placing different types of Faraday cages over the leads, and found generally the more shielding we added, the greater the decrease in noise. The ultimate system we found worked best included plastic covers directly on the leads, followed by aluminum foil around each lead, covered entirely by an aluminum can, which was then wrapped in aluminum foil.

In an effort to minimize environmental noise entering thought the body of the fridge, we temporarily placed an additional portable MuMetal blanket around the body of our fridge. The combination of the MuMetal blanket and extra shielding around the magnet leads reduced our noise by an order of magnitude to two orders of magnitude over our frequency range, with the greatest reduction from 100 Hz to 1 kHz.

In the process of organizing our lab we moved our portable external electronics, including filters, SQUID electronics, our computer and signal generator into a walled server rack. The external electronics had previously been laid out a lab bench, with each instrument plugged into the wall separately. The result was a large reduction in our noise floor as seen in Figure 5-5. This reduction was likely a result of the walled server rack acting as a Faraday cage, shielding our electronics from the EM noise in the building. We conducted tests with the server rack with and without walls and observed a decrease in high-frequency noise with the doors added, making a more complete Faraday cage. In addition, we placed the box that contained our external SQUID electronics inside another metal box within the server rack and grounded to the server rack sitting about two feet above the rest of the external electronics. This move and additional shielding proved to further reduce our high frequency noise by a half order of magnitude in the frequency range between 800 to 1300 kHz (see Figure 5-5). In addition to acting as a Faraday cage, the server rack also allowed us to plug all of our external electronics into the same ground, which likely contributed to the noise reduction. However, we were led to believe the greater effect was the Faraday cage, since there was a large difference between the wall-less server rack, and the walled rack.

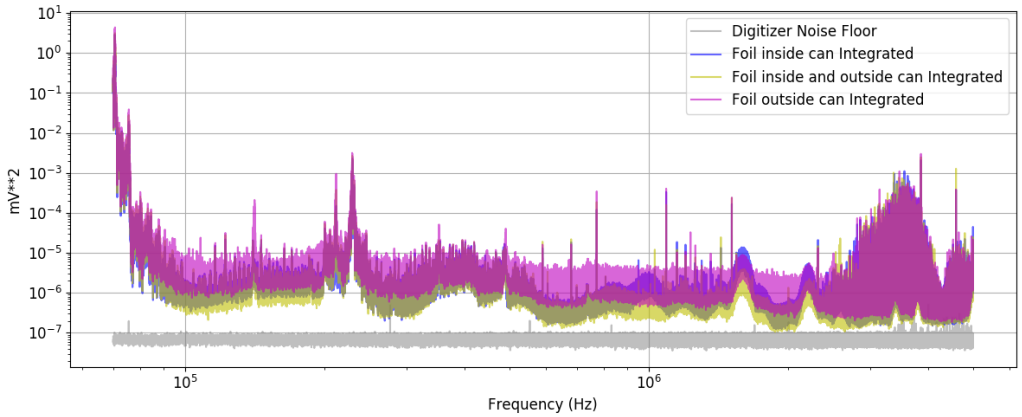

(a)

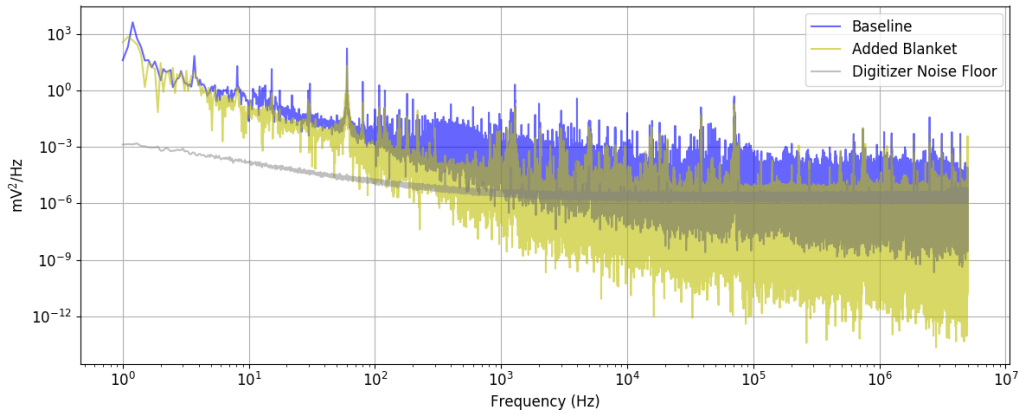

(b)

Figure 5-4: Top: Shielding the magnet leads with layers of metal and plastic (see text), Integrated refers to the two-stage SQUID on one chip, see Chapter 4 for details on the SQUIDs. Bottom: Low-frequency PSD of the body of the fridge without additional Mumetal shielding (Baseline) and with an addition Mumetal blanket (Added Blanket). The digitizer noise floor is added for comparison.

Unfortunately, the background created by the fully charged magnet is much noisier than the background created by external EM signals. With the magnet fully charged, the background from the magnet dominated all other backgrounds and the only reduction which was visible was the disappearance of the board EM peaks, however the results from these tests can be used to better inform future upgrades with lower magnet backgrounds.

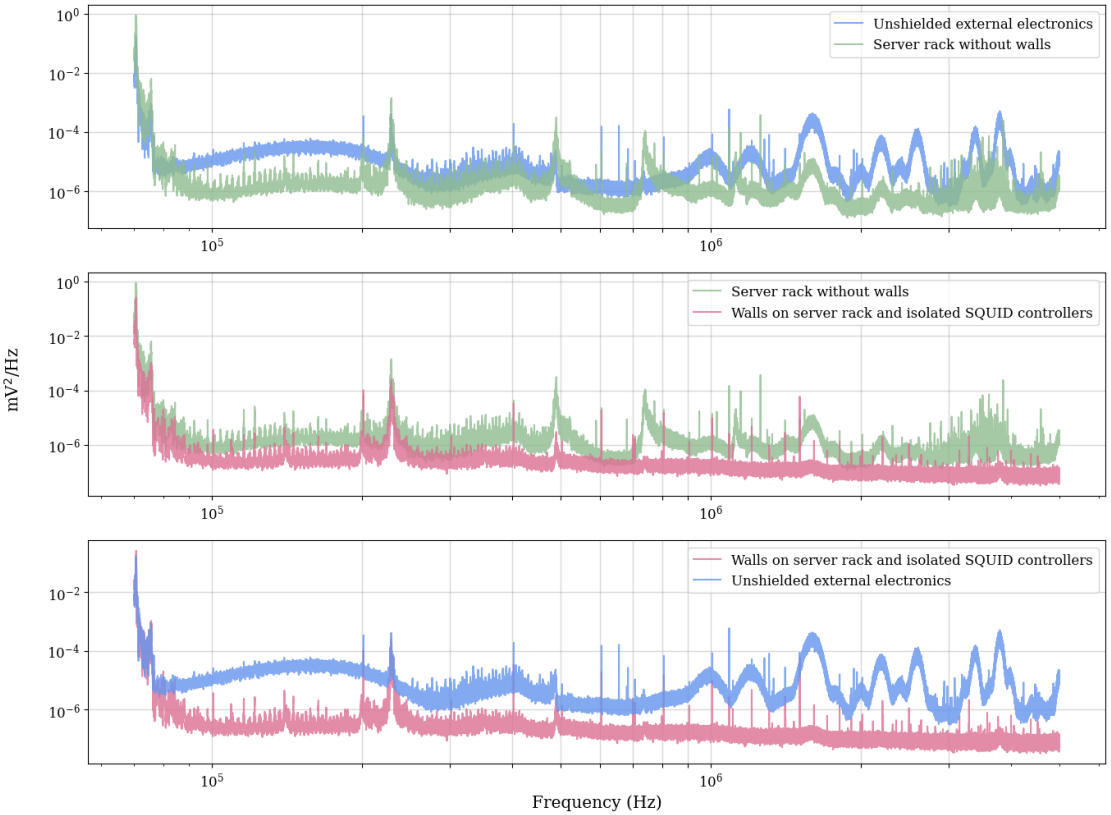

Figure 5-5: The PSD of the noise with the magnet off. Blue: configuration with external electronics on lab bench not connected to the same ground. Green: external electronics in an un-walled server rack with all electronic plugged into the same ground. Pink: external electronics in a fully shielded server rack with walls on and SQUID controller box additionally shielded inside the server rack, all grounds are connected.

5.3.3 Vibrations

Vibrations are a major contributor to noise in our system, both directly at low frequencies, and with harmonics to higher frequencies. Any mechanical motion of the pickup within a spatially varying magnetic field gradient will generate a current signal within our circuit. These field gradients can come from fringe fields from the magnet (only present when the magnet is on) or from residual DC fields from the environment penetrating into the pickup region. Vibrations can be induced by a variety of sources, including cryogenic pumps and compressors, as well as environmental sources within the building. The detector is supported by a simple vibration isolation system described in [32], which reduces, but does not completely eliminate, this vibration.

We perform a series of tests using a PCB Piezotronics model 393B04 accelerometer

fastened to the room-temperature plate on top of the fridge. With the accelerometer taking z-directional data, we took simultaneous SQUID data for different experimental configurations. These tests included changing the current in the magnet, turning off the pulse tubes, and driven external audio speaker tests.

Since we expect the majority of the signals from vibrations come from the pickup moving in the fringe fields, we tested that theory by varying the value of the magnetic field. As seen in Figure 5-6, the values of our baseline increase with the charge of the magnet. The effect of the magnet can be seen to drop off at the top of our frequency range, as seen both with and without the high-pass filter. We observed large structures at frequencies above 10 kHz which seem to be connected to the charging process. These large structures don't appear in our long data runs, after the magnet has been charged for a significant amount of time, suggesting they are an artifact of the charging, possibly a result of trapped flux or heating of different parts of the system resulting from the charging. The magnet charging process, and the magnet hold charge significantly increase our noise floor.

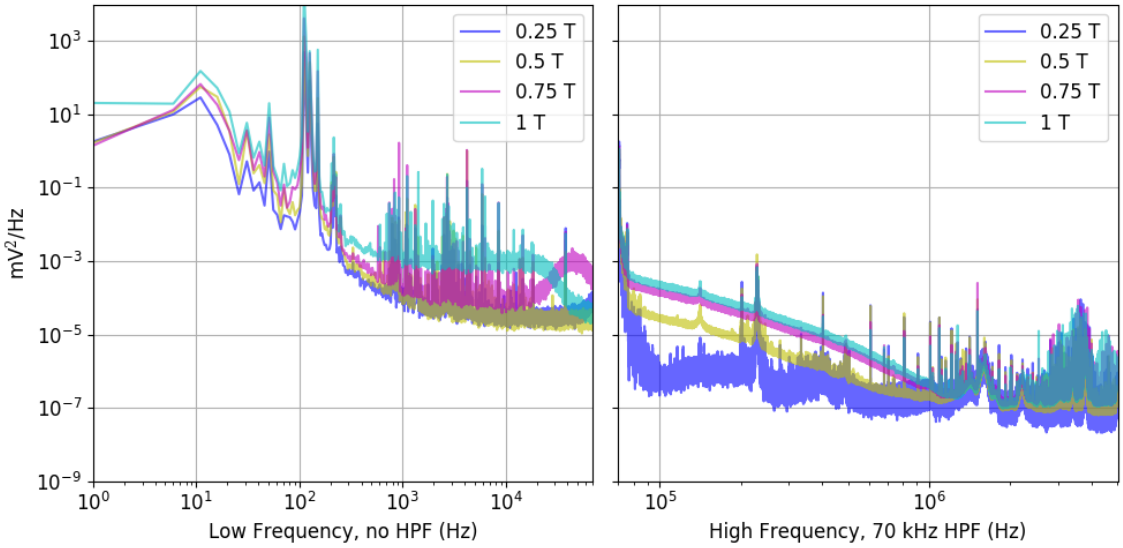

Figure 5-6: Ramping the magnet strength from 0.25 T to 1 T in steps, data taken in 20 minute intervals for the low-frequency plot (left plot) and 8 hours for 0.25 T, 4 hours for 0.5 T, 2 hours for 0.75 T, and 1 hour for 1 T in high-frequency plot (right plot).

We took additional data with a SQUID not connected to the pickup cylinder, or anything at all, and saw no change in the noise level of the PSD from the changing magnet strength. The disconnected SQUID is located on the Still plate, which is a little under two feet above the mixing-chamber plate where the data-taking SQUID is mounted. These disconnected SQUID data suggest that if there are significant fringe

fields, they do not affect any of the electronics beyond the pickup cylinder and above the Still plate.

The pulse tubes (PTs) provide the second stage of the cooling power for the dilution refrigerator. They can only be shut off for brief tests without compromising the temperature stability of the system. To minimize the amount of time that the PTs were turned off, we limited our tests to 60 second integration periods, with $\sim 10\,\mathrm{s}$ between turning the PT off and starting data collection. The data we collected during this 60 second period showed that the pulse tubes are relatively well isolated from our system as compared to higher background which dominate. We see only small effects at the PT driving frequency of 1.4 Hz and harmonics at 2.8 Hz, higher harmonics are not significantly observed.

Though we turned off the PT compressor, the mixture circulation pumps stayed on. These are located about a meter from the base of the fridge on rubber isolation pads in a rolling cart, but it's possible these are adding to the vibrations. The mixture circulation pumps cannot be turned off. In addition, the effects from the pulse tube compressor were not considered, since the compressor is well isolated in a separate room from the dilution refrigerator.

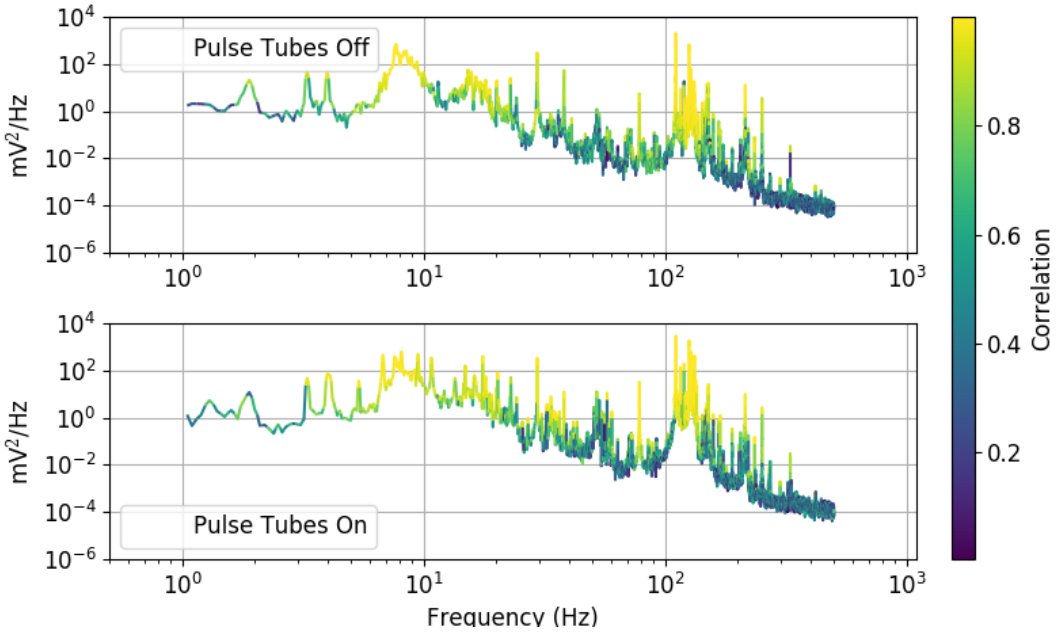

Figure 5-7: Low-frequency spectrum of acceleration correlated data with the pulse tubes on for 60 seconds, then off for 60 seconds.

To see which vibrational frequencies induced the strongest signals in our system, we used a speaker connected to a signal generator driven at signal frequencies. The speaker was place on top of our fridge, and we collected data for frequencies in the

range of 1 Hz to 10 kHz. As seen in the 100 Hz example, we were able to clearly see the accelerometer peak, along with a corresponding peak in the SQUID signal. As the speaker was uncalibrated, and the accelerometer is not rated to measure accelerations above 450 Hz, we use this data a proof-of-concept for the propagation of vibrations from the top of the fridge into our data readout. For future upgrades, vibration isolation systems could greatly reduce our backgrounds.

In addition, we took data with the accelerometer on top of the fridge and with the accelerometer placed on the floor near the fridge, unmounted. There was correlation with the floor and the SQUIDs, but the rate of correlation was much higher from the top of the fridge. We expect the vibration on the top of the fridge to be higher in general, since it is a free-standing structure, and the floor is on the ground level.

With the magnet off, the signals resulting from the vibrations are not a result of the pickup moving through stray magnet fields. The vibrational noise induced by the SQUIDs themselves is below the base SQUID noise floor. A likely possibility for the source of the majority of the vibrational noise is microphonic noise from the wires in the fridge.

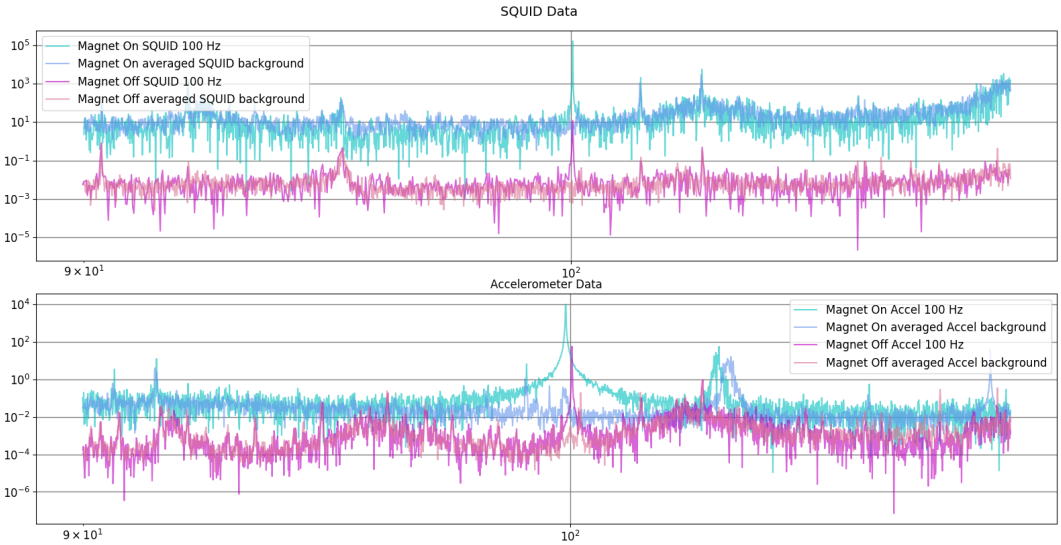

Figure 5-8: Data taken with the speaker place on the top of the dilution refrigerator and driven at 100 Hz, two runs taken, magnet off (0 T) and magnet on (1 T). The top plot shows the data taken from the SQUIDs, and the bottom plot shows the data form the accelerometer.

5.3.4 70 kHz Anomalous Signal

For Runs 2-5, our power spectrum contained a large peak at 70 kHz of unknown origin which remained in the data regardless of magnet charge and filters in the system. As

a part of our background characterization, we conducted multiple tests to determine the nature of this signal.

The peak first appeared after the upgrade to the cylinder pickup from the loop pickup in June of 2019. During the upgrade, there was a down time from April till June of 2019 in which no data was taken. It is possible that there has been a 70 kHz signal since the start of data taking in 2018, and the upgrade in the pickup caused an amplification of that signal, allowing it to be raised above the noise floor. The hypothetical amplification of the peak could be caused by a resonance of the signal with the cylinder. Another possibility is that during the down time when the upgrades were taking place something changed in our environment creating this 70 kHz signal.

We conducted multiple tests in which we varied high and low pass filters, magnet charge, magnet height, and the RF value to see how these changes affected the 70 kHz signal. Changing filters and the charge value of the magnet had little to no effect on the peak, but we did see a shift in the amplitude from changing the magnet height and varying the RF value. A change in the RF resistance value is reflected in the peak amplitude but not in the shape of the signal, leading us to believe that the signal enters on the SQUID input. For an RF value of 100 kΩ, the peak is on the order of 1e-1 mV^2/Hz, and at an RF value of 10 kΩ, the peak has a value around 1e-3 mV^2/Hz. The loss of two orders of magnitude for a one order of magnitude loss in RF is as expected for a signal on the SQUID input.

Changing the magnet height had a less definitive conclusion, the amplitude of the peak changed with the height but not consistently. After multiple tests of raising and lowering the magnetic the peak amplitude was occasionally at a max for the lowest height of the magnet, and occasionally at a max for the highest height of the magnet. The only conclusion we draw was that moving the magnet affected the signal. Previous EM tests had little to no effect on the signal.

Additionally, we observed the value of the peak of the 70 kHz signal to fluctuate over time. In the spring of 2021, we observed values of the peak amplitude for an RF value of 100 kΩ around 5$\times$1e-1 mV/Hz, and as high as 1 mV^2/Hz. In comparison, in the fall of 2021 values at the same RF were closer to 1e-1 mV^2/Hz. In the same week during the fall, we observed a peak value of 2$\times$1e-2 mV^2/Hz, almost a full order of magnitude lower.

The peak is not present in the Run 6 data for either the axion data, nor the gravitational wave data, which both use wire loops in different configurations. The existence of the 70 kHz peak in only Runs 2-5 suggests that the signal is tied to the cylinder, either in a stronger coupling to the pickup itself or having to do with the installation of the cylinder.

5.3.5 Effects of Noise on the Axion Analysis

The axion signal is characterized by a Doppler-shifted peak in frequency space, which disappears when the magnet is turned off. This signal is quite unique, and unlikely to be mimicked by any noise source. However, while the axion signal can be distinguished from background signals, noise limits the searchable parameter space and the sensitivity of our experiment. Lumped-element axion experiments are evolving and gaining sensitivity, and with this improved signal sensitivity there is likely to be increased noise sensitivity. EM shielding and vibration mitigation are essential for controlling noise in a lumped-element axion experiment.

While simple in design, the ABRA experiment has a sophisticated analysis with a complex array of backgrounds. Each element of the experiment has been studied and while the backgrounds have not all been fully accounted for or mitigated, as a pathfinder experiment, ABRA has taught us much about searching for axions in this frequency regime and controlling and characterizing noise for future experiments.

Chapter 6

ABRACADABRA-10cm Gravitational Wave

Once ABRACADABRA-10cm completed its Run 3 data collection and set limits in previously unsearched parameter space, large modifications needed to be made to the experiment to increase the sensitivity to axions. Taking equation 4.1 for the signal to noise ratio, one of the most effective methods to increase sensitivity is to increase the magnetic field volume, requiring a new magnet to be wound and a new larger dilution refrigerator to cool the magnet. Another method that could be employed for greatly increasing our sensitivity would be to change from a broadband search to a resonant search. Both of these changes require major hardware and/or software upgrades, a new experiment had to be built from the ground up to reach greater axion sensitivity. To achieve this higher sensitivity, ABRA joined with the DMRadio Pathfinder experiment with Stanford and UC Berkeley. In Appendix B more details on the DMRadio suite of experiments are given. With the ABRA setup at MIT we moved to modify the experiment to search for high-frequency gravitational waves (HFGWs), which produce an electromagnetic signal analogous to the axion signal. With ABRA-GW, we set out to prove a lumped-element axion experiment could be modified to search for HFGWs without losing sensitivity to axions.

The following chapter begins with GW electrodynamics, followed by the setup and calibration of ABRA-GW, and concluding with the results and data analysis of ABRA-GW.

6.1 Gravitational Wave Electrodynamics

The following section is based on work in [124] and [125]. The scale of interest for our experiment is ωL, with ω as the angular frequency of the incoming GW wave, and L as the characteristic spatial length scale of the experiment, which is 10 cm for ABRA. With the division by the speed of light for units, this quantity is very small, we take $\omega L \ll 1$. For the remaining chapter and in Appendix D, ωL/c is implied with

the mention of orders of ω.

Another important note, on the spatial length scale of the experiment and in the frequency range considered ($\omega > 10$ kHz) we can safely consider mechanical perturbations negligible, and only consider the electromagnetic interactions. There have been considerations of how a mechanical interaction with the detector could in itself produce a small (likely negligible) electromagnetic signal, however this effect would likely only enhance our signal and is safe to not consider in our analysis.

6.1.1 Gravitational Wave Interaction

Much like the axion, GWs can also be detected electromagnetically, the EM mechanism for interaction however is fundamentally different for GWs. Axions modify Maxwell's equations through their interaction with photons, and while a closer analogy can be made using the inverse Gertsenshtein effect, we can also consider that GWs perturb the flat spacetime metric, thereby modifying Maxwell's equations. The flat spacetime metric is given by $g_{\mu\nu} = \eta_{\mu\nu}$, and in the presents of a GW the spacetime metric is perturbed adding a new term $h_{\mu\nu}$, to form $g_{\mu\nu} = \eta_{\mu\nu} + h_{\mu\nu}$. The work done in [124] and [125] and what is presented here is all done in the proper detector frame, as opposed to the TT frame discussed in Chapter 3, we also consider a plane wave in the following section. In this frame distances can be measured by rigid rulers, and the detector quantities are understood.

In the proper detector frame, a plane GW warping spacetime at position $\mathbf{r}$ with azimuthal and inclination angles of ϕ_h and θ_h respectively produces a metric $h_{\mu\nu}$ of

$$
\begin{aligned}
h_{00} &= \omega^2 e^{-i\omega t} F(\mathbf{k}\cdot\mathbf{r}) r_m r_n \sum_{A=+,\times} h^A e^A_{mn}(\hat{\mathbf{k}}), \\
h_{0i} &= \frac{1}{2}\omega^2 e^{-i\omega t}\left[F(\mathbf{k}\cdot\mathbf{r}) - iF'(\mathbf{k}\cdot\mathbf{r})\right]\left[\hat{\mathbf{k}}\cdot\mathbf{r}\; r_m\delta_{ni} - r_m r_n \hat{k}_i\right] \sum_{A=+,\times} h^A e^A_{mn}(\hat{\mathbf{k}}), \\
h_{ij} &= -i\omega^2 e^{-i\omega t} F'(\mathbf{k}\cdot\mathbf{r})\left[|\mathbf{r}|^2\,\delta_{im}\delta_{jn} + r_m r_n \delta_{ij} - r_n r_j \delta_{im} - r_m r_i \delta_{jn}\right] \sum_{A=+,\times} h^A e^A_{mn}(\hat{\mathbf{k}}),
\end{aligned}
\tag{6.1}
$$

where $F(\xi) = (e^{i\xi} - 1 - i\xi)/\xi^2 \approx -1/2 + \mathcal{O}(\xi)$, $h^{+,\times}$ represents the amplitude of the two possible strain polarizations, and the direction of GW propagation is $\hat{\mathbf{k}} = \sin\theta_h \hat{\mathbf{e}}_\rho^{\phi_h} + \cos\theta_h \hat{\mathbf{e}}_z$, with $\hat{\mathbf{e}}_\rho^{\phi_h}$ and $\hat{\mathbf{e}}_z$ representing the unit vectors with the origin at the center of the experiment for a polar angle of ϕ_h. The polarization tensor $e_{ij}^{+,\times}$ is defined as

$$
\begin{gathered}
e_{ij}^{+} = \frac{1}{\sqrt{2}}\left[\hat{U}_i\hat{U}j - \hat{V}_i\hat{V}_j\right], \quad e_{ij}^{\times} = \frac{1}{\sqrt{2}}\left[\hat{U}_i\hat{V}j + \hat{V}_i\hat{U}_j\right], \\
\hat{\mathbf{V}} = \hat{\mathbf{e}}_\phi^{\phi_h}, \quad \hat{\mathbf{U}} = \hat{\mathbf{V}} \times \hat{\mathbf{k}}.
\end{gathered}
\tag{6.2}
$$

The EM tensor is modified by the perturbation of spacetime to gain a new effective current in the presence of a GW,

$$\partial_\nu F^{\mu\nu} = j^\mu + \mathrm{j}^\mu_{\mathrm{eff}}, \qquad \partial_\nu F_{\alpha\beta} + \partial_\alpha F_{\beta\nu} + \partial_\beta F_{\nu\alpha} = 0 \tag{6.3}$$

where $F^{\mu\nu}$ is the electromagnetic field tensor, j^μ is the electromagnetic current for a flat spacetime metric and the equation on the right is the homogeneous form of Maxwell's equations which are unaffected by the presents of a GW, the appendix of [125] goes into detail of why the equations are unaffected. The effective current is given by

$$\mathrm{j}^\mu_{\mathrm{eff}} \equiv \partial_\nu \left(-\frac{1}{2} h^\mu_\mu F^{\mu\nu} + F^{\mu\alpha} h^\nu_\alpha - F^{\nu\alpha} h^\mu_\alpha \right). \tag{6.4}$$

The effective current can also be written in terms of the effective polarization and magnetization vectors for a more direct comparison to axion electrodynamics. In Appendix D the full equations for the effective current resulting from a plane GW in a toroidal magnet are given.

6.1.2 Gravitational wave detection in ABRACADABRA-10cm

The effective current is induced in the presents of a magnetic field, and that effective current itself induces an oscillating magnetic field at the frequency of the GW, ω. The form of the magnetic field for a toroidal magnet with inner radius R and peak field value B_{max} (see Figure 6-1) like the one used in ABRA is a DC magnetic field with

$$\mathbf{B}_0 = B_{\mathrm{max}}(R/\rho)\hat{\mathbf{e}}_\phi \tag{6.5}$$

for the volume within the toroid and zero elsewhere. The resulting magnetic field in center of the toroidal magnet can be found from the effective current using Biot-Savart law

$$\mathbf{B}_h(\mathbf{r}', \mathbf{k}) = \frac{1}{4\pi} \int_{V_B} d^3\mathbf{r} \frac{(j_\rho \hat{\mathbf{e}}_\phi - j_\phi \hat{\mathbf{e}}_\rho) \cdot (\mathbf{r}' - \mathbf{r})}{|(\mathbf{r}' - \mathbf{r})|^3}, \tag{6.6}$$

with j_ρ and j_ϕ as $\mathbf{j_{eff}} \cdot \hat{\mathbf{e}}_\rho$ and $\mathbf{j_{eff}} \cdot \hat{\mathbf{e}}_\phi$ respectively. The integral is taken over the volume of the magnetic field, V_B. Much like for the axion searches of ABRA, we search for this resulting magnetic field. The GW magnetic field signal would be detected from the flux in the area of the pickup loop

$$\Phi_h = \int_{A_\ell} d^2\mathbf{r}' \mathbf{B}_h(\mathbf{r}') \cdot \hat{\mathbf{n}}'(\mathbf{r}'), \tag{6.7}$$

which induces a current in the pickup loop that is read out with our current sensors. Unlike the axion signal, the GW signal lacks azimuthal symmetry. The asymmetric

signal results in a weaker coupling to a circular pickup. The radial component of the effective current is integrated to zero for the circular pickup and only the azimuthal component remains, resulting in an ω^3 dependence from only the $h^\times$ polarization,

$$\Phi_c = \frac{ie^{-i\omega t}}{16\sqrt{2}} h^\times \omega^3 B_{\max} \pi r^2 R a (a + 2R) \sin^2(\theta_h), \tag{6.8}$$

where R and a are dimensions of the toroid as depicted in Figure 6-1. However if that symmetry is broken in the form of a semicircular figure-8 loop, then the signal is able to couple to terms up to ω^2 using the radial component of the effective current. The figure-8 pickup couples to both the $h^\times$ and h^+ components. The flux for a figure-8 pickup is approximated as

$$\begin{aligned}\Phi_8 = \frac{ie^{-i\omega t}}{3\sqrt{2}} h^\times \omega^2 B_{\max} r^3 R \ln(1 + a/R) \sin^2(\theta_h) \\ \times (h^\times \sin(\phi_h) - h^+ \cos(\theta_h) \cos(\phi_h)).\end{aligned} \tag{6.9}$$

These equations for flux are made in the limit that the magnet is a rectangular toroid and has infinite height, to account for these approximations in the analysis we find the flux on the pickup loop resulting from a GW by simulation as opposed to analytically.

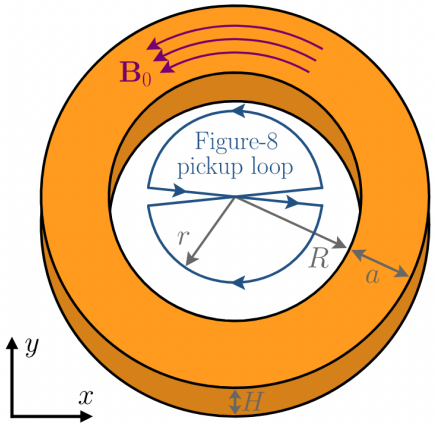

Figure 6-1: Reproduced from [124], original proposition for the GWs search with an ABRACADABRA-like detector. The DC magnetic field is represented by $\mathbf{B}_0$, H, R and a are the height, inner radius and width of the toroid respectively. The radius of the semi-circular figure-8 is r.

6.2 Setup

ABRA-GW is designed to simultaneously look for axions and HFGWs. The system is constructed with two pickups for detection: a circular pickup for axion detection, and a semi-circular figure-8 pickup for GW detection. To first order, the axion signal does not induce a current in the figure-8 loop and the GW signal does not induce a current in the circular loop, this is because the mutual inductance between a circular loop and figure-8 loop should be effectively zero. To higher orders, possible cross-measurement of signals is not much of a concern since the signal shapes are very distinct and cross-measurements can be vetoed in the analysis. Since these searches do not fundamentally interfere with one another theoretically, we were able to conduct simultaneous searches. Experimentally we faced a few challenges ensuring the lack of interference between the searches.

ABRA-GW has gone through two configurations. The first configuration consisted of three pickups, two GW pickups rotated 90 degrees apart, and an axion pickup. As shown in Figure 6-2, the GW pickups were 1 cm above and below the axion pickup, which was lined up with the center of the magnet. The axion calibration loop used was the same as in previous runs, a 9 cm diameter wire that runs through the inside the magnet in the azimuthal direction. The plan was to calibrate the GW pickups with a GW loop 5 cm above the center of the magnet, which was at a 45 degree rotation with respect to both GW pickups. This 45 degree rotation would have allowed us to calibrate both GW pickups with a single calibration loop. Our system has two two-stage DC SQUIDs, which limits our readout to measuring only two pickups at a time. For the first cool down, we connected the top GW pickup (the GW loop closest to the GW calibration loop) and the axion pickup.

In the first cool down with configuration 1, the signal we observed from the GW calibration was the same order of magnitude as measured from both the axion pickup and the GW pickup. Since the signal in the two pickups were of similar strength, we could not trust that the signal seen in the GW pickup was directly as a result of the current in the calibration figure-8 loop itself, nor could we make any sort of claim that the axion pickup was weakly coupled to the GW signal. Without being able to trust the calibration, we could not reasonably take science data. We suspected the source of the issue was a weak coupling between the GW pickup loop and the GW calibration loop, and the signal was primarily resulting from higher up in the system, past the SQUIDs in the form of parasitic inductances.

To determine the nature of the signal measured on the axion pickup from the GW calibration we ran a dedicated parasitic inductance and calibration cool down, where we connected only one of the SQUIDs to a pickup loop, and only one of the calibration loops to a port. The disconnected SQUID can only collect signal from the SQUID readout chain, since the current sensors themselves are housed in a super conducting niobium shield. We left a SQUID connected to the axion pickup loop, disconnecting the GW pickup by removing the twisted pair from its SQUID

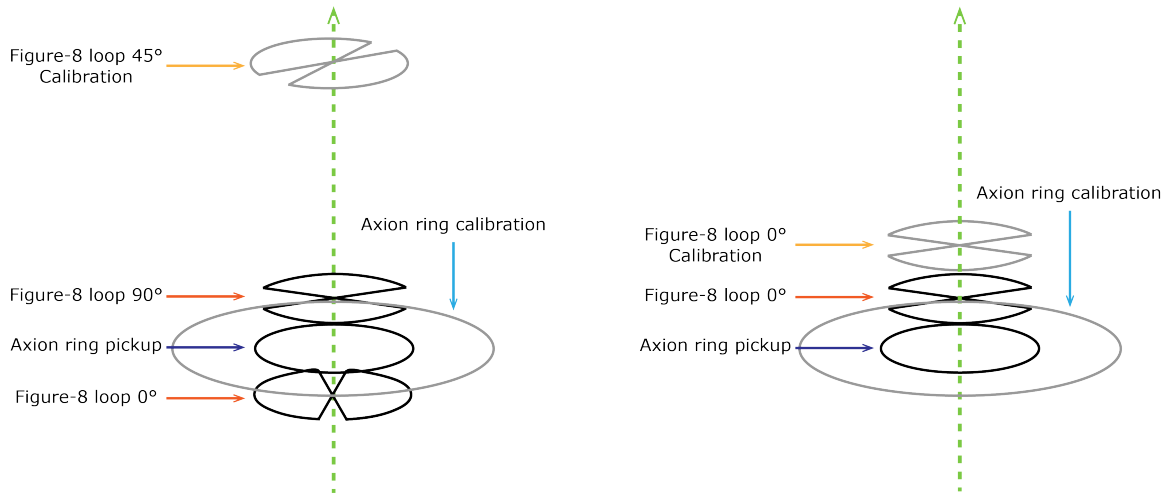

Figure 6-2: Configuration 1 (left) of the pickups and calibration loops with the extra directional GW loop and the GW calibration loop 5 cm above the axion pickup. Configuration 2 (right) of the pickups and calibration loops without the directional loop and the GW calibration loop 2 cm above the axion pickup.

and securing that pair with Kapton tape to the side of the shield. In addition we disconnected the axion calibration loop by unplugging the SMA connector on the mixing chamber plate which connected to the calibration port. Figure 6-3 shows the results of this dedicated parasitic inductance and calibration cool down. From this data, we determined that the parasitic inductance from the input and readout wires in the GW calibration system was the dominate source of the GW calibration signal, as the GW calibration signal read by the connected axion SQUID was less than the signal read on the disconnected GW SQUID. In addition, We found that the SQUID used in the GW search had a higher noise floor than the SQUID used for the axion search. To combat these issues, we needed to increase the coupling between the GW pickup and calibration loops and reduce the parasitic inductance in the system as much as possible. Both solution required hardware changes to the system.

First, we needed to fully determine the state of the physical pickup structures, as they were sealed inside of the shield containing the magnet. When we unsealed the shield halves we found that the Teflon tube which held the pickups had fallen from its secured position at the top of the magnet, and the twisted pairs coming out of the pickup tube were un-shielded (the solder casing had slipped off) and slightly unwound. For the purposes of calibration, the fallen position of the Teflon tube should not have had a large impact, since the wires appeared to still be in good condition, but now the geometric coupling to the axion and GW signals would be altered. A new position of the pickups would need a new signal simulation, and would result in a different $\mathcal{G}_V$ for the axion search. The center of the magnet produces the largest coupling between the signals of interest and the pickup, our sensitivity would be greatly reduced with a

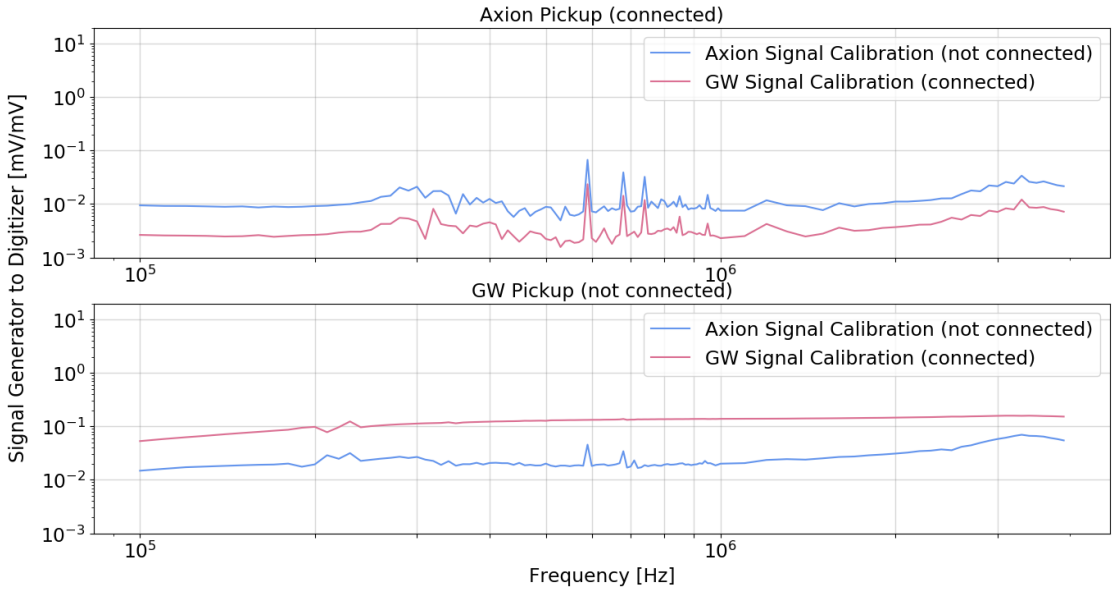

Figure 6-3: Results from the dedicated parasitic inductance and calibration cool down. Both figures show the gain from the signal generator output to the end of the readout chain at the digitizer for both the axion calibration and the GW calibration. The axion calibration loop was disconnected for this cool down. The top figure depicts the axion detection chain, with the axion pickup connected to the SQUID. The bottom figure depicts the GW detection chain with the GW pickup not connected to the SQUID, this figure effectively shows the SQUID baseline with calibration signals injected into the system.

move away from the center of the magnet. For the second configuration, we took care to secure the Teflon tube not only with epoxy, but also mechanically by pressing the shield halves closer together to rest the ends of the tube on both the top and bottom of the shield.

In addition to the loose wire shielding, we had originally wired the pickup tube such that the wires were all coming out in the same direction. With the twisted pairs un-shielded and in such close proximity we were maximizing any potential parasitic inductance that could occur within the shield. In the new hardware design described below we made sure all the twisted pairs came out of the tube from different points. This spreading out the of the twisted pairs also allowed us to push the magnet halves closer together as mentioned above.

We determined we needed to rewire the pickups to neaten the wires, reducing parasitic inductance, and to choose a design that gave us a stronger coupling between each pickup and its respective calibration loop. We made the decision to remove the bottom GW pickup, line up the GW calibration loop with the remaining GW pickup, and move the GW calibration loop down such that it was only a centimeter

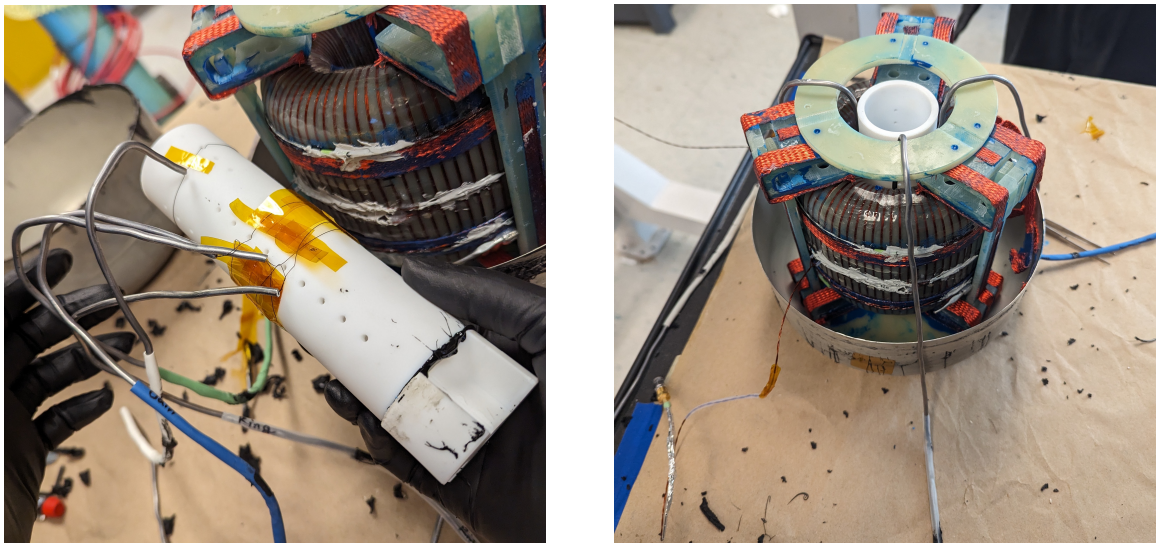

(a) (b)

Figure 6-4: (a) The first version of the Teflon tube wiring removed after a year of running with all twisted pairs exiting the magent at the same point. (b) Second version of the Teflon tube wiring, showing the twisted pairs coming out of the magnet at different, equidistantly spaced points.

above the pickups. There were multiple reasons for deciding on this new design, but it came down to what gave us the most interesting science result and the best chance to calibrate the detector. The initial goal of ABRA-GW was to show a search for axions and a GW search could be done simultaneously, and if possible we wanted to maintain that goal. By increasing the mutual inductance between the GW pickup and the GW calibration loops, we increased our chances of being able to distinguish a signal in the GW pickup from a signal in the axion pickup resulting from a signal in the GW calibration loop. In other words, we would be able to confidently claim that the signal seen on the GW pickup from the GW calibration was actually a result of a signal on the calibration figure-8 and not some other parasitic inductance that would also show up on the axion pickup. From a proportional Biot-Savart calculation, moving the GW calibration loop even just 2 cm closer the to GW pickup should have increase our mutual inductance by almost an order of magnitude, and aligning the figure-8s should have also greatly increased the mutual inductance. Simulations done in COMSOL confirmed this calculation.

While rotating the GW calibration loop to line up with only one of the GW pickups did remove the possibility to calibrate the other GW pickup, we had no chance of calibrating the far GW pickup even without rotating the calibration loop out of phase. With the GW calibration loop 3 cm above the near GW pickup in configuration 1, we were not strongly coupled enough to calibrate, therefore even moving the GW calibration loop down to 1 cm above the near GW pickup would not have assisted in

calibrating the far loop, which would have been 3 cm away from the new calibration loop in this configuration. The only chance we would have of calibrating two out-of-phase GW pickups would be to place the rotated calibration loop between the two pickups, but even then the 45 degree rotation is still decreasing the mutual inductance significantly. In addition this directional configuration would displace the axion pickup significantly and greatly decrease the axion sensitivity, making it difficult to prove the GW search does not interfere with the axion sensitivity.

6.3 Calibration

After changing from configuration 1 to configuration 2, we could show that the current on the GW calibration loop was producing the dominate signal on the GW pickup, and the signal was no longer dominated by parasitic inductances. The signal on the GW pickup as a result of the GW calibration was now more than two orders of magnitude higher than the signal produced by the axion calibration. Figure 6-5 shows the difference between the two configurations in terms of the gain on the GW pickup loop from the signal generator to the ADC.

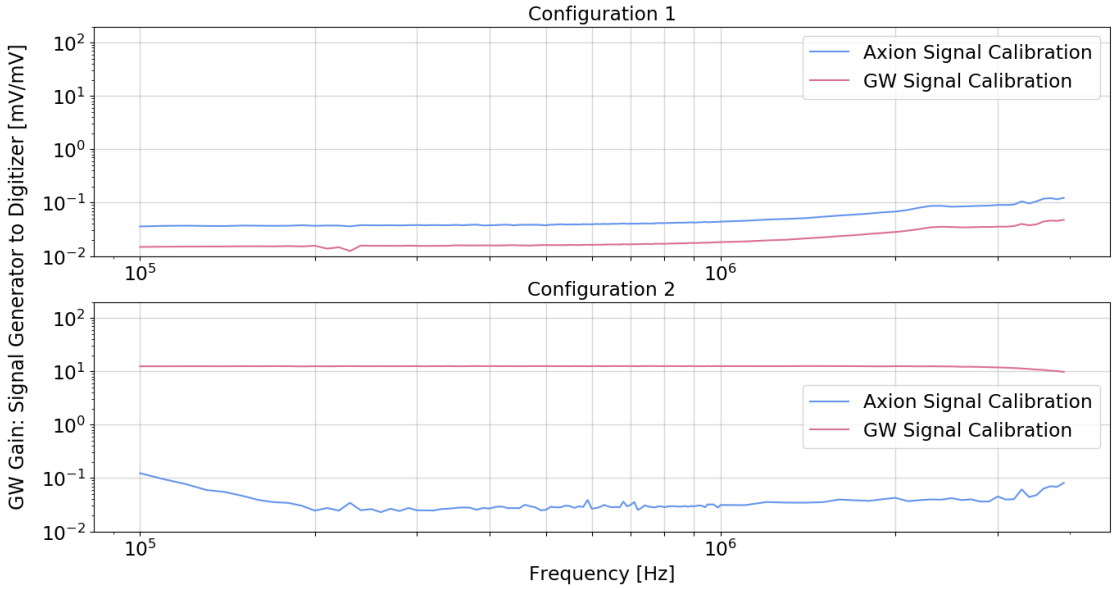

Figure 6-5: Difference between configuration 1 (top) and configuration 2 (bottom) as shown in gain on the GW pickup loop. Both figures show the gain from the signal generator output to the end of the readout chain at the digitizer for both the axion calibration signal and the GW calibration signal.

We also compared our calibration data to a calculated expected value for the gain of each calibration combination. This expected value was calculated by modifying the

existing framework from Runs 1-3 to fit the new setup with multiple pickups. The largest challenge for the new expected values was calculating current transfer between loops using a matrix of mutual inductances, as each loop in the system had mutual inductance with every other loop. Self inductances and mutual inductances were calculated in COMSOL then those results were used to find the expectation value of a signal resulting from the signal generator, results and general system parameters show in Appendix C. The expectation values ensured we understand our system within an order of magnitude, but the exact value has a low chance of matching as a result of unknown parasitic inductances and systematic error.

Calibration results were additionally used to find the transfer function between a signal on one part of the system to another, for example converting flux on the pickup to voltage on the digitizer as was used to create the templates. These conversions are done using equation (4.5) which describes the terms used for finding the gain from the calibration results.

6.4 Analysis

As a transient search with a fundamentally different signal, the GW search analysis looks different from the axion analysis done in Runs 1 and 3, described in section 5.1. ABRA-GW relies on the use of signal templates and a Gaussian Process (GP)-based handling of the background and likelihood ratio. We conducted a signal injection recovery to prove the efficacy of our data pipeline, and a search to place limits on a merger in our local environment.

The analysis was tuned using the first few hours of data that were taken. The DAQ crashed after around 12 hours of data collection and had to be restarted, the files from the first collection are clearly marked by timestamp and labeling. The crash happened as a result of memory allocation issues, the data itself was uncorrupted. The pipeline testing and the signal injection were preformed on this data, the merger search was preformed on the data collected after the crash.

The analysis testing and the merger search were conducted on the subMIT cluster at MIT Physics, and a copy of the data was stored there as well.

6.4.1 Templates

For the purposes of our demonstrator experiment, we only computed one signal template to use in our analyses, the analysis framework can be generalized to multiple templates, time and computing resources permitting. This template models the scenario where there is a primordial black hole merger event at some distance from the pickup. The signal is now no longer a plane wave, however the only change to the electrodynamics in section 6.1 and Appendix D is to replace the $h^+e^{-i\omega t}$ and $h^\times e^{-i\omega t}$ terms with the time-dependant form of the merger. All parameters were chosen to maximize the strain in the merger within our frequency window (10 kHz to 3 MHz)

and are listed in Table 6.1. In addition, the incoming angle of the GW was chosen to maximize the effective current which results in a higher flux on the pickup.

The ripple code base [126] was used to generate the waveforms of the two polarizations of strain ($\mathbf{h}^{+}(\omega)$ and $\mathbf{h}^{\times}(\omega)$) for the merger. Ripple outputs the waveforms as separate polarization arrays in frequency space, which we generate from 1 Hz to 5 MHz. The arrays could in principle be generated from 10 kHz to 5 MHz if we intended to stay in the frequency domain, however the transition to the time domain requires either the full frequency spectrum or a very carefully taken FFT with zero-padded arrays. We transform the arrays output from Ripple to the detector frame (mV on the digitzer) in the frequency domain before adding them together and taking a real inverse fast Fourier transform (irfft) to get to the time domain. Transformations could be made in the time domain where they would be convolutions instead of multiplications, but this process is both more computationally expensive and careful consideration is needed to preform linear and not circular convolutions.

Merger parameter	value
M_1	0.01 $M_\odot$
M_2	0.01 $M_\odot$
Dimensionless spin	0
Time of coalescence	1 ms
Distance to source	3.24 × 1e-23 Mpc (1 m)
Inclination	0

Table 6.1: Inputs to ripple to generate the merger template

The transfer function used to convert the strain output from ripple to voltage on the digitizer is in two parts: the first relies on finding the induced flux on the pickup using the analytic form of the effective current from [125] and COMSOL simulation, and the second part converts from flux on the pickup to voltage on the ADC and is found from the calibrations.

The full function for the effective current can be found in Appendix D, terms up to ω^2 were input to COMSOL as the external current density. The flux on the pickup as a result of the effective current was found by integrating over the surface of the pickup, see Appendix A for more details on the simulation configuration. The effective current for the h^{+} and $h^{\times}$ polarization terms were simulated separately. By testing different values of the strain polarizations, we ensured that the scaling with strain was linear and additive in terms of the two polarizations. To simplify the COMSOL inputs, terms which were constant and consistent across the different components of the effective current were accounted for post-simulation. The flux on the pickup is found to be

$$\Phi_{\text{pickup}} = \frac{1}{\mu_0} \times \mathbf{h}^{+/\times}(\omega) \times \omega^2 \times \text{COMSOL}, \tag{6.10}$$

where here the $\mathbf{h}^{+/\times}(\omega)$ terms represent the waveforms for the h^+ and $h^\times$ components of the incoming wave and "COMSOL" is the output from the simulation. The maximum magnetic field strength and the dimensions of the magnet are included in the COMSOL simulation. The strain is effectively unit-less, ω is the frequency of the GW whose units are accounted for in the effective current and the output from COMSOL is in units of flux, the μ_0 is the permeability of free space and is used to correct for the units from the effective current which was input to COMSOL. The maximum magnetic field strength could be accounted for post-simulation instead of in COMSOL since it is a constant and consistent term, but it has a value of 1 T and therefore it is inconsequential where it is included for our purposes.

As a result of our goal to create and run our analysis with one template, we chose only one angle for the incoming wave, which was $\pi/2$ for both ϕ_h and θ_h. This angle was chosen to maximize the $h^\times$ component, since the COMSOL results for $h^\times$ were on average an order of magnitude larger. Figure 6-6 shows the COMSOL flux results for each polarization for incoming angles from 0 to π in both θ_h and ϕ_h. In an analogy to the axion search, the conversion of strain to flux on the pickup for the GW search includes similar information to the axion geometric coupling term $\mathcal{G}_V$, which connects the axion current to the current on the pickup.

After finding the flux on the pickup from COMSOL, the gain resulting from the calibration of the GW pickup loop with the GW calibration loop were used to convert to mV on the digitizer,

$$\Phi_{\text{pickup}} \times \mathcal{T}(f)_{\Phi_{\text{pickup}} \to V_{\text{ADC}}} = V_{\text{ADC}}. \tag{6.11}$$

The transfer function for flux on pickup to voltage on ADC, $\mathcal{T}(f)_{\Phi_{\text{pickup}} \to V_{\text{ADC}}}$, is found from equation (4.5) dividing the total gain, $V_{\text{ADC}}/V_{\text{Sig}}$, by $\Phi_p/I_C \times I_C/V_{\text{Sig}}$, the mutual inductance between the pickup loop and calibration loop, and the attenuation and current conversion between the signal generator and calibration loop. See section 4.3 for more general ABRA calibration details. The results for the two polarizations were then added, an irfft was preformed, and the waveforms were band-pass filtered from 10 kHz to 3 MHz. Figure 6-7 shows the difference between a waveform which was only band-pass filtered in units of strain and one that had the transfer functions applied with units of mV.

In an effort to save computation time, we originally farther down-sampled the template, stopping when we could still resolve the template. We determined that we could down-sample by three and still resolve the signal, but two produced a smoother template. However, since the portion of the signal we are using is only 30 μs long, resolution gained by using the full signal outweighs the computational benefits. This benefit was determined by running the Gaussian process algorithm on a segment of

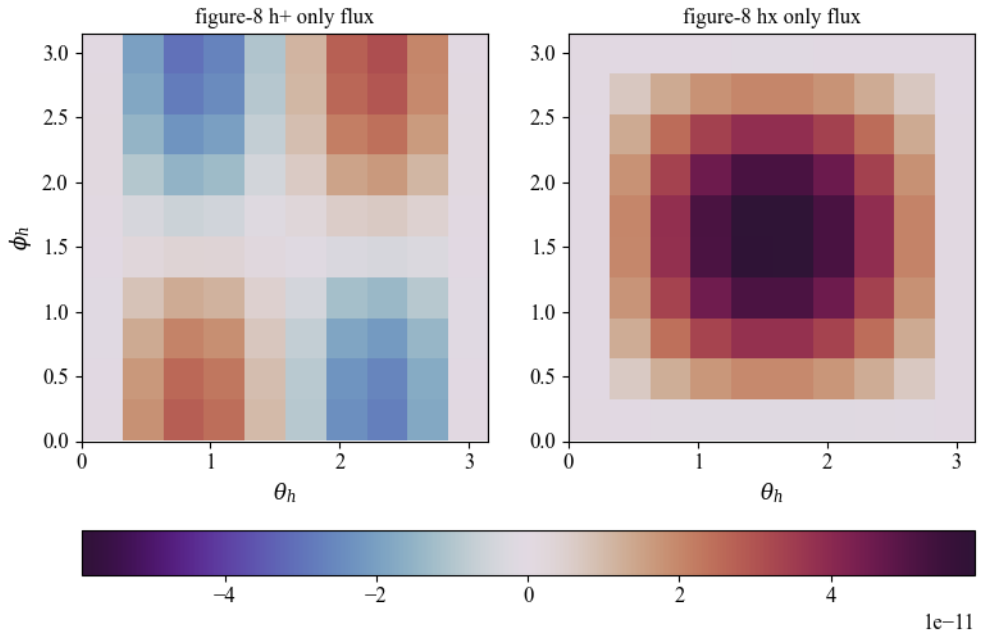

Figure 6-6: Each square in the plots is the magnitude of flux in the z-direction for a given pair of angles. The flux values are calculated over the half-sphere. Left: flux calculated over the figure-8 area for $h^{\times} = 0$, $h^{+} = 1000$. Right: flux calculated over the figure-8 area for $h^{\times} = 1000$, $h^{+} = 0$.

test data with a known signal injected and different amounts of down-sampling on the template and data, the algorithm recovered the signal with the least amount of uncertainty with no down-sampling. The signal injection recovery is explored more in section 6.4.6.

6.4.2 Backgrounds, Data Filtering and Data Stability

To get any meaningful results from our data we needed to have a good understanding of our backgrounds. The raw GW data had a consistent periodic pattern on multiple time scales which made the background difficult to model. When plotted in a histogram by like-voltage values, the result was bimodal with peaks in alternating bins. An autocorrelation analysis was preformed to characterize the time-scales of the periodic behavior and determine if we could down-sample the data to filter out the signal. The results of the autocorrelation found an oscillation with a frequency of 5 MHz which appeared to be somewhat aliased, and an additional aliasing of that signal at $\sim$ 500 kHz. Down-sampling to remove the 5 MHz signal could be done

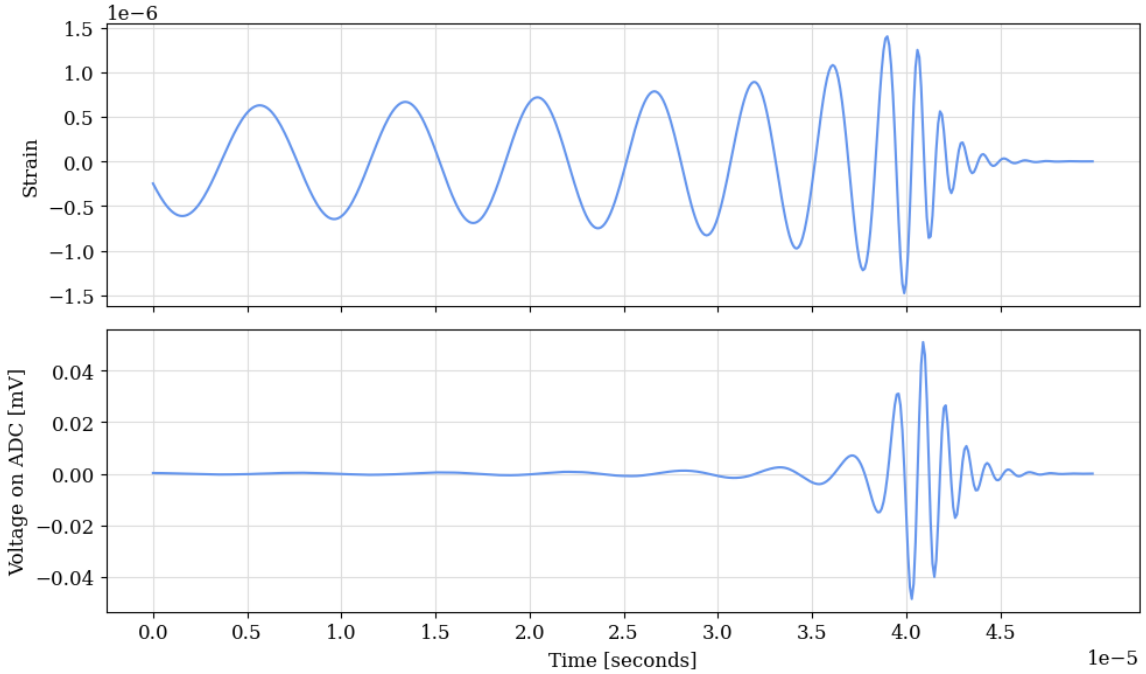

Figure 6-7: Results from a 0.01 $M_\odot$ equal mass merger with the parameters from Table 6.1. Top: strain from h^+ and $h^\times$ polarizations added together, band-pass filtered and an irfft taken. Bottom: transformed h^+ and $h^\times$ polarizations to the detector frame, band-pass filtered and an irfft taken.

without affecting our sensitivity to the chirp signal, but high-pass filtering the signal removed both the 5MHz signal and the aliased 500 kHz signal.

Zooming out we found another periodic background at 13 kHz, which is directly in our search range of interest. As can be seen in Figure 6-7, the in-spiral of the template sits around 13 kHz, therefore removing that frequency would degrade the template. After band-pass filtering from 10kHz to 3 MHz the histogram only had one mode, but failed the Anderson-Darling test for normality. To model the simplified 13 kHz periodic background for the likelihood analysis, we used a Gaussian Process (GP). We used the George code base [127] for our GP in both the signal injection analysis, and the merger search analysis.

Additionally, we checked the stability over time by dividing the data into hour-long segments and transforming those segments to averaged PSDs. Each PSD was composed of 10 seconds of raw data, 360 PSDs were averaged together for each hour. For legibility, those hour-long PSDs were grouped into days and averaged to form Figure 6-9, were we can see over the six days of data collection each averaged day had very little variance from the other averaged days.

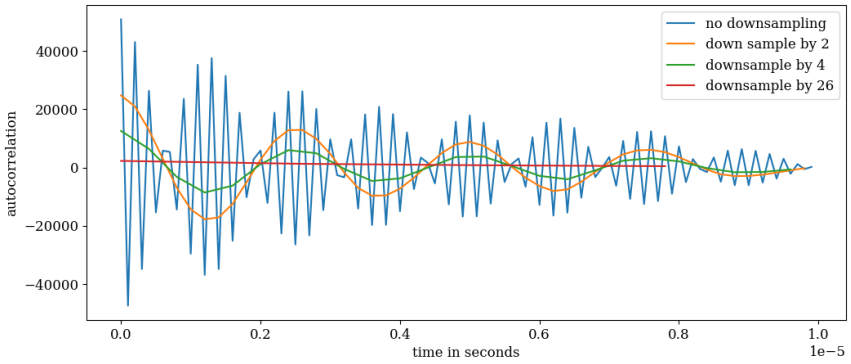

(a)

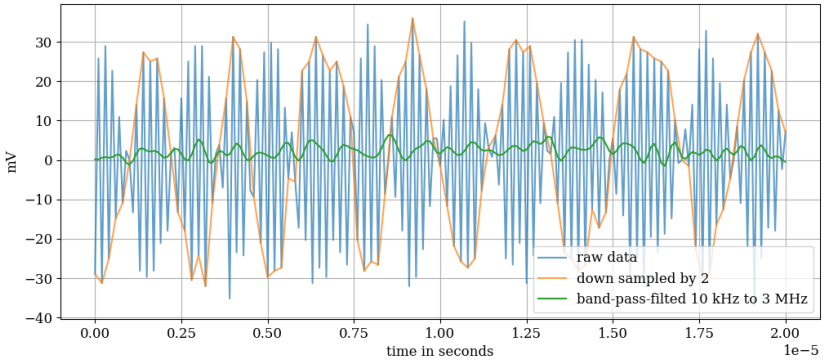

(b)

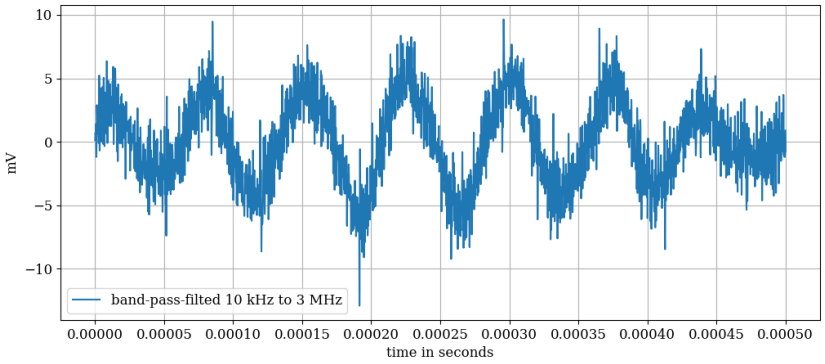

(c)

Figure 6-8: (a) Auto correlation of 10 μs of data (100 samples) taken in Run 6. The data was down-sampled to varying degrees to remove periodic noise features. The 5 MHz signal is seen in the data in its raw form (blue), and down-sampling by 2 (orange) removes the high-frequency signal. The broader aliased $\sim$500 kHz signal is only completely removed by down-sampling by 26. (b) Down-sampling vs filtering, the band-pass filter removes the signal and aliased remnants. (c) Band-pass filtered data, 13 kHz background is apparent.

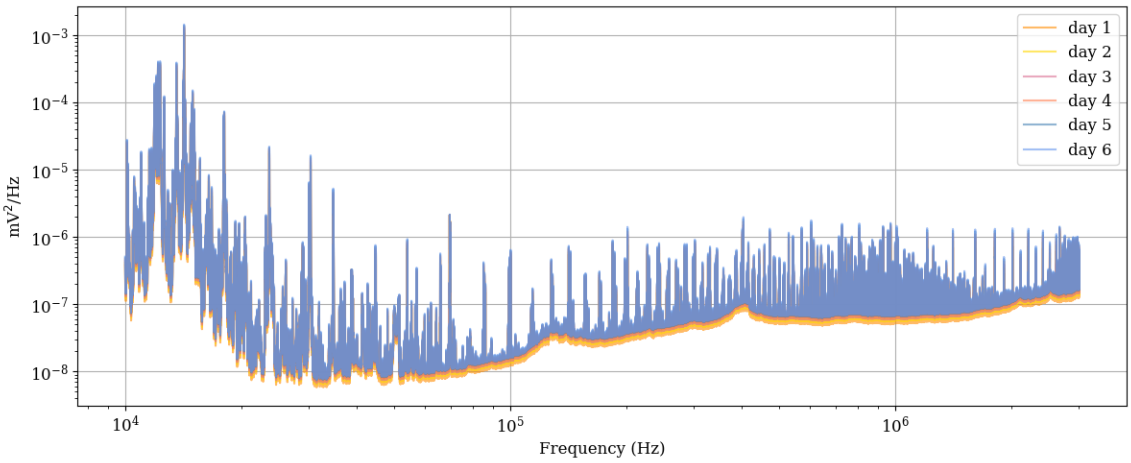

Figure 6-9: Power spectral density of the GW data in the frequency range of interest, 10 kHz to 3 MHz. The PSD for each day is composed of 8,640 averaged 10-second PSDs.

6.4.3 Axion Sensitivity

One of the goals of the ABRA-GW campaign was to prove we can simultaneously look for both axions and GWs. For the axion portion of the search, we changed from a cylinder to a ring to physically accommodate the GW pickup and calibration loops. This change decreased our sensitivity to axions through the geometric coupling constant $\mathcal{G}_V$. Comparing Run 6 to the published value for Run 3, the axion search went from a $\mathcal{G}_V$ of 0.031 to 0.022. We used the flux method described in section 5.3 to find the Run 6 value, but the published Run 3 value is likely slightly inflated from the true value. To compare sensitivity to axion between previous runs and Run 6 we could not compare limits on $g_{a\gamma\gamma}$ because of this change in $\mathcal{G}_V$ and the decrease in integration time from one month to one week. Instead we took data of the SQUID noise floor on the axion channel and compared to the data taken with the axion loop simultaneously with the GW search. Proving we have not increased our noise with the addition of the GW loop demonstrates that if we wanted to integrate for longer and run the full axion analysis pipeline, we could recover similar limits to Run 1. We focus our discussion on Run 1 since it was similarly a ring, the $\mathcal{G}_V$ values between Run 1 and Run 6 are 0.019 to 0.022 respectively using the method flux method described in section 5.3.

We demonstrated with Figure 6-10 that the axion sensitivity was not degraded by the GW search. In Figure 6-10, the axion data taken during six-day-long Run 6 is segmented, transformed to PSDs, averaged down and compared to the SQUID noise floor. All the data shown in the figure have the shapes of the physical high and low pass filters filtered out and the calibration data was used to compare results at the

stage of the pickup loop. For the SQUID noise floor we used data taken a few months prior of the SQUID used for axion data collection not connected to any input. This data was taken in a five minute collection period as a part of the inductance run. After the inductance run and the switch from configuration 1 to configuration 2 we switched which SQUID was connected to which pickup for spatial reasons. Since this data is much shorter than the full axion collection, and therefore does not average down as much, we down-sampled the SQUID floor data to match the width of the axion data. Similarly to the ABRA-GW axion result, figure 5 of [32] shows that Run 1 also had a noise floor close to that of the SQUID noise floor. The noise floor in [32] was determined analytically instead of experimentally, as Run 1 did not take data with the disconnected SQUID.

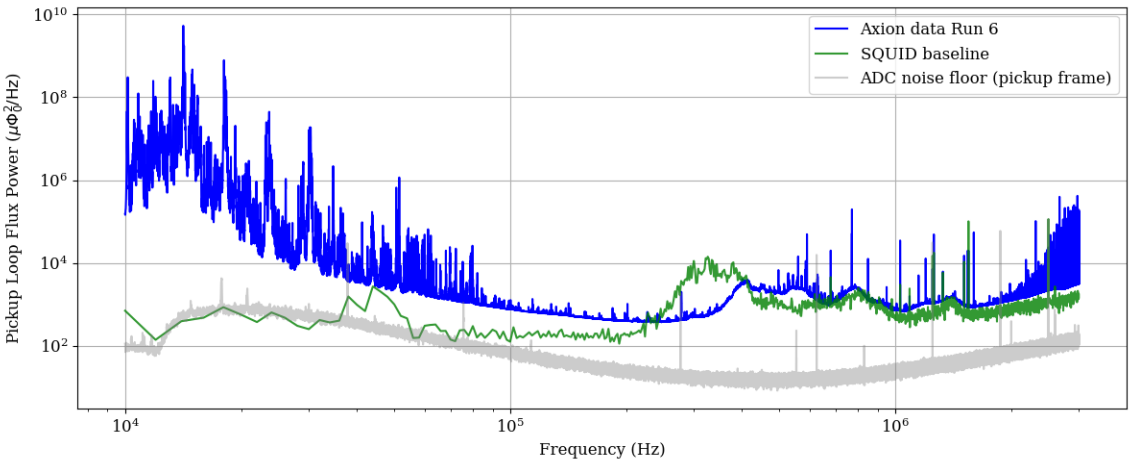

Figure 6-10: Axion data collection for Run 6 (blue), SQUID noise floor (green) and digitizer noise floor (gray). Data shown is in power on the pickup loop, with all filters divided out. All three data sets were taken at different times in different thermal cycles. There are some regions where the axion Run 6 data seems to be more sensitive than the SQUID noise floor, we attribute this unlikely situation to differences between cool downs, as the data collections were taken months apart and the experiment was thermal-cycled between collections. The result shows that the data taken with the axion loop attached to the SQUID and the GW loop simultaneously taking data had a noise floor almost the same the SQUID noise floor.

6.4.4 Noise-equivalent strain

The noise-equivalent strain is a metric adopted by the GW community used to compare different detectors that may be looking for different GW signals with different detection methods. The fundamental idea is to characterize the noise of the detector as the minimum possible strain that could be detected by that detector. The metric was created to be independent of the detector properties.

A method for finding the NES is given by chapter 7.1 of [84]. GW detectors primarily collect TS data to search for transient events, that data is often later Fourier transformed for frequency based searches. The input signal to a given detector can be described by

$$h(t) = D^{ij} h_{ij}(t) \tag{6.12}$$

where D_{ij} is a constant tensor which describes the detector geometry, and h_{ij} is the familiar GW tensor shown for a plane wave in equation (6.1). For that given signal the detector outputs a signal of the form

$$\tilde{h}_{\text{out}} = \mathcal{T}(f)\tilde{h}(f), \tag{6.13}$$

with $\tilde{h}(f)$ as the Fourier transform of $h(t)$ and $\mathcal{T}(f)$ as the transfer function of the detector, example shown in equation (6.11) for ABRA-GW. Accounting for the noise that is measured, the full detector output can be written as

$$s_{\text{out}} = h_{\text{out}}(t) + n_{\text{out}}(t). \tag{6.14}$$

If we think of the noise output in the same manor as the signal, with all the noise output from the detector as having originated completely as an input (i.e. all noise that originates inside the detector is attributed as input to the detector) we can write the Fourier transform of the input noise as

$$\tilde{n}(f) = \mathcal{T}^{-1}(f)\tilde{n}_{\text{out}}(f). \tag{6.15}$$

The input noise $n(t)$ can alternatively be thought of as the minimum value of strain that could be detected, with the detector response completely filtered out. The input to the system $s(t)$ is now a sum of $n(t)$ and $h(t)$. If we assume the noise is real and stationary and time averages to zero, $\langle n(t)\rangle = 0$, then we have

$$\langle \tilde{n}^*(f)\tilde{n}(f')\rangle = \delta(f - f')\frac{1}{2}S_n(f), \tag{6.16}$$

where $S_n(f)$ is the noise spectral density and is a signal-sided PSD as defined in [84]. If we set $f = f'$ and restrict to the time interval to $[-T/2, T/2]$ with T as the data collection time, $\delta(f - f')$ reduces to $T = 1/\Delta f$. With some rearranging, we now have

$$\frac{1}{2}S_n(f) = \langle|\tilde{n}(f)|^2\rangle\Delta f, \tag{6.17}$$

and transforming to the time domain,

$$\langle n^2(t)\rangle = \int_0^\infty df\, S_n(f). \tag{6.18}$$

Once the square root is taken of the noise spectral density, $\sqrt{S_n(f)}$ is what we

refer to as the noise-equivalent strain. Figure 6-11 reproduced from the MAGO 2.0 collaboration [118] mentioned in section 3.3.3 shows the NES for various GW detection experiments, focusing on the HFGW regime. The projection for the m^3 lumped-element resonant detector is based on the work in [124] and the future DMRadio m^3 experiment.

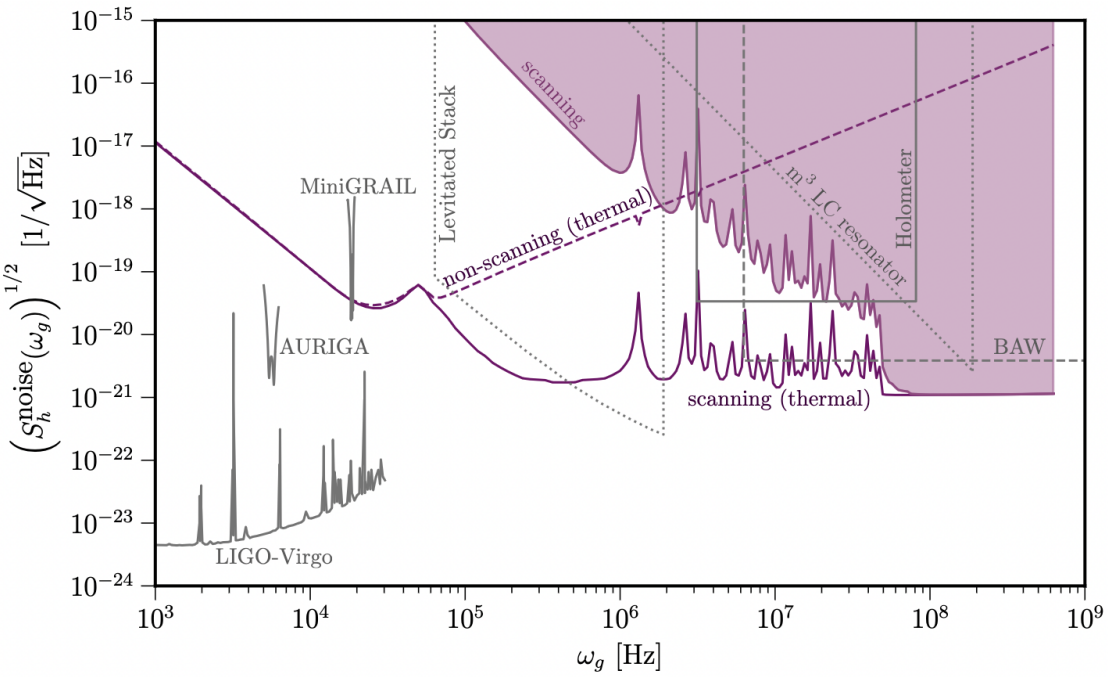

Figure 6-11: Reproduced from [118], the noise-equivalent noise power projections for many experiments which can search for HFGWs.

Finding the NES experimentally was essentially the inverse process of transforming the merger template. For the NES we start with power on the digitizer from the full data set[1], then work backwards to convert to strain. Since the data for Run 6 was taken in TS ($n_{\rm out}(t)$), we first had to find the PSD of the data on the digitizer. The data was divided into segments, those segments were Fourier transformed ($\tilde{n}_{\rm out}(f)$), squared and divided by frequency step to get the PSD ($\mathcal{F}_{V_{\rm ADC}}(f)$), then all the individual PSDs were averaged together ($\bar{\mathcal{F}}_{V_{\rm ADC}}(f)$). The final $\bar{\mathcal{F}}_{V_{\rm ADC}}(f)$ was averaged over the total collection time of six days, representing the PSD of the detector output.

The input to the detector was found by multiplying $\bar{\mathcal{F}}_{V_{\rm ADC}}(f)$ by the inverse of

[1]We take $s_{\rm out}(t) = n_{\rm out}(t)$ for the full data set as the case where there is no signal without losing our ability to claim discovery by using the fact that the signals we look for are transient and lasting μ seconds. To find the NES we rfft the data and average over the span of data collection, any transient signal we might be looking for would be averaged to zero and we lack the sensitivity to search for a stochastic signal with only one detector.

the transfer function which converts flux on the pickup to voltage on the digitizer,

$$\bar{\mathcal{F}}_{V_{\mathrm{ADC}}}(f)\mathcal{T}^{-1}(f)^2_{\Phi_{\mathrm{pickup}}\to V_{\mathrm{ADC}}} = \mathcal{F}_{\Phi_{\mathrm{pickup}}}(f). \tag{6.19}$$

To get the NES, we used simulation to convert flux on the pickup to strain. Using the equations for effective current from [125] as input and separating the h^+ and $h^\times$ terms into separate simulations, we use equation (6.19) to find either h^+ or $h^\times$. Since the simulation results for h^+ and $h^\times$ are not equal, the polarizations must be handled separately. When choosing an incident angle to produce the strongest signal, the $h^\times$ term dominates by an order of magnitude for $\theta_h = \phi_h = \pi/2$, with this in mind we choose approximate the NES for the $h^\times$ term only. With the simulation-based transfer function, we found $\bar{\mathcal{F}}_{\mathrm{strain}_{h^\times}}(f) = 1/2S_n(f)$. The factor of 2 relating $S_n(f)$ and $\bar{\mathcal{F}}_{\mathrm{strain}_{h^\times}}(f)$ results from us taking a two-sided PSD on the raw data. The result for solving for $\sqrt{S_n}$ using the experimental and simulation is show in Figure 6-12.

The theoretical calculation shown in Figure 6-12 was performed by Nicholas Rodd, using the same incident angle of $\theta_h = \phi_h = \pi/2$ for only the $h^\times$ term. The noise floor for the detector was estimated to be $10^{-6}\Phi_0/\sqrt{\mathrm{Hz}}$ corresponding to the estimated SQUID noise floor, and the flux on the pickup was estimated using equation (6.9). As can be seen in the figure, the experimental result closely matches the theoretical calculation.

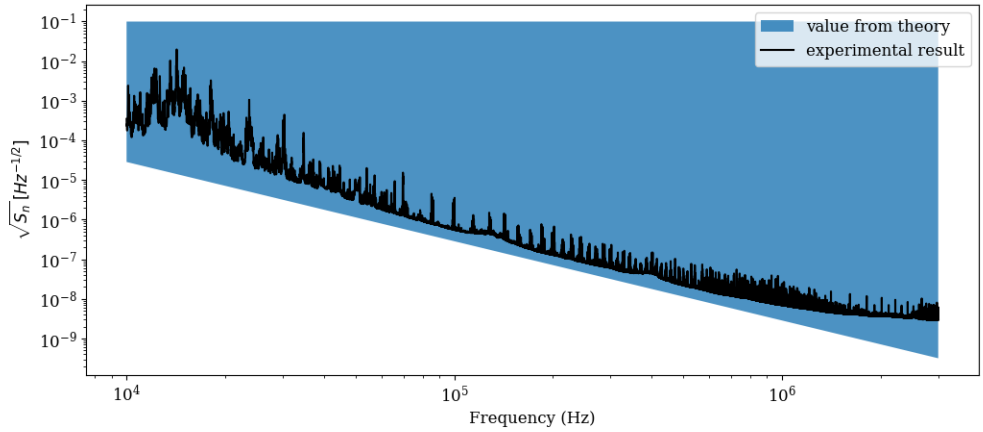

Figure 6-12: Noise-equivalent strain power for the ABRA-GW run, calculated for the $h^\times$ polarization of the strain in the angular direction which maximizes amplitude for both the theoretical calculation and the experimental result. The data was averaged over a six-day-long period.

6.4.5 Data Pipeline

The basic outline of the data pipeline was

$$s(t)_i \rightarrow \text{band-pass filter} \rightarrow \text{GP marginalized log-likelihood} \rightarrow \text{best-fit signal amplitude} \rightarrow \text{statistical processing}, \tag{6.20}$$

for data segment $s(t)_i$ indexed by $i \in 1, 2, ..., N_{\text{process}}$ where N_{process} is the number of segments processed.

The amplitude of the signal reference throughout the analysis text refers to a constant that is multiplied by the existing template amplitude. An amplitude of 1 would mean the template was unaltered, and the amplitude represents a merger with the parameters listed in Table 6-1 originating from $\theta_h = \phi_h = \pi/2$ or from a closer distance with a different angular entry point. For an amplitude with a value other than 1 could originate from a merger from a different distance away, or incoming from a different direction. A negative amplitude would be a signal incoming from the opposite angular direction $\theta_h, \phi_h \in [\pi, 2\pi]$, for $\theta_h = \phi_h = 3\pi/2$ the amplitude would be -1. Both the distance and the incoming angle affect only the amplitude of the signal and not the frequency.

To preform a template search, the template and the data must be in the same frame, the detector frame (voltage on the digitizer) in the case of our analysis. The template is pre-filtered and transformed to the detector frame as shown in section 6.4.1 above, and the raw data begins in the detector frame, only needing to be band-pass filtered. The less processing that is required of the raw data the more efficient the analysis, the templates can be pre-computed for whichever frame is convenient, but if the analysis were to be done in another frame taking FFTs of the TBs worth of raw data in real-time would be very computationally expensive.

Once the raw data is filtered to the same frequency range as the template, 10 kHz to 3 MHz, a GP is used to construct the marginalized likelihood for the signal. The GP works by fitting multiple distributions to a data set using a joint Gaussian distribution. A covariance matrix, referred to as a kernel in GP terminology, is chosen as an input to the GP to define the relationship the data and the joint distribution. We want to chose a kernel that will closely model the background and will not fit to the signal at all. As seen in Figure 6-8, our background is mostly Gaussian with an enveloping period of 13 kHz. To model this background, we choose the exponential sine-squared kernel,

$$K(\mathbf{x}_i, \mathbf{x}_j) = \exp\left(-\Gamma \sin^2\left[\frac{\pi}{P}|\mathbf{x}_i - \mathbf{x}_j|\right]\right) \tag{6.21}$$

for correlated input coordinates $\mathbf{x}_i$ and $\mathbf{x}_j$, the scale of the correlations Γ and constant period P. The constant period of the exponential sine-squared kernel would not fit to the template which contains higher frequencies than the periodic background and does not have a constant frequency. We used the python package George [127] to compute our GPs.

The GP analyzer is given the detector data ($\mathbf{s}(t, A)$ for signal amplitude A) and the signal template ($\mathbf{h}(t, A)$). The joint distribution is fit to the background and the marginalized log-likelihood is constructed for the residuals, where the residual is the detector data minus the signal, $\mathbf{r}(t, A) = \mathbf{s}(t, A) - \mathbf{h}(t, A)$. For the GP, we marginalize over the GP joint Gaussian distribution to from the marginalized likelihood,

$$p(\mathbf{r}|t, A) = N(m(t), K) \tag{6.22}$$

where K is the kernel and $m(t) = E[\mathbf{r}]$ is the mean of the residual. The marginalized log-likelihood is,

$$\log(p(\mathbf{r}|t, A)) - \frac{1}{2}\mathbf{r}^T K^{-1}\mathbf{r} - \frac{1}{2}\log(\det|K|) - \frac{n}{2}\log(2\pi) \tag{6.23}$$

with n as the number of correlated variables. The maximum likelihood for an amplitude is found from maximizing the log marginalized likelihood, or minimizing the TS defined as

$$\mathrm{TS} = -2\log\left(p(\mathbf{r}|t, A)\right). \tag{6.24}$$

We assume the from the Bayesian marginalized log-likelihood that the TS is chi-squared distributed as was done in [128], but this assumption will be verified in future work. Figure 6-13 shows the GP analysis and TS minimization on one segment of data.

The iminuit package was used for minimizing the TS to find the best-fit amplitude for the given data segment and the Hesse error on the fit [129]. The best-fit amplitude and the Hesse error are used to find a 95% confidence level exclusion for amplitude above the found value, 1σ and 2σ upper limits and 1σ lower limits on that confidence level post-processing. The 95% confidence level exclusion can be interpreted as 95% confidence that a signal could not be present with an amplitude greater than that value. The lower limit is only given to 1σ as to not over-estimate our limit.

6.4.6 Signal injection recovery

As a test of the data-processing pipeline's ability to recover an existing signal and provide reasonable limits we performed a signal injection recovery. The signal injection recovery was done by taking a segment of data the length of the signal and adding the template for the merger to that segment. By varying the amplitude and running the Gaussian process, best fit and statistical analysis we compared the injected value of the amplitude to the best-fit recovered value and 95% exclusion limit. For the same segment of data, the relationship between the injected amplitude and recovered amplitude is linear with a constant offset. The linear relationship is a result of the GP formation of the likelihood, which will fit a distribution to the consistently periodic background and not to the dynamic signal to form the null hypothesis and therefore stay relatively constant in its estimate of the null. This linearity servers as proof to

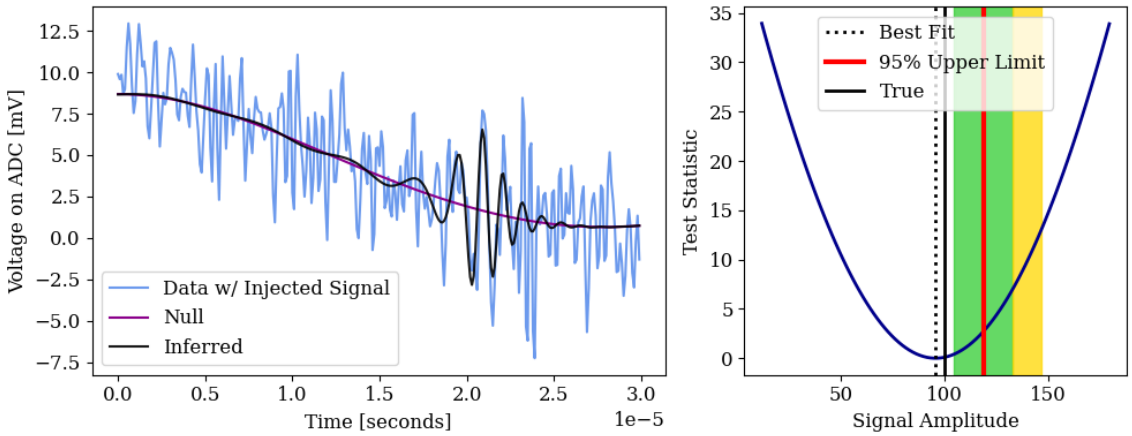

Figure 6-13: Gaussian Process regression run on a single segment of data. Left: the "Null" line was produced by the GP fit to the background and the "Inferred" line is that background plus the signal with the best-fit amplitude found from the regression. Right: The profile likelihood is shown in dark-blue with a minimum at the best-fit amplitude value. 95% confidence with one-sigma bounds (green) and two-sigma bound (yellow).

the validity that the GP is indeed only modeling the background for the null. The 95 % exclusion is also linear and constantly offset from the best-fit value as is expected since it is constructed from the best-fit value and the Hesse error. The results for 100 amplitudes ranging from 1 to 100 are shown in Figure 6-13 (a).

As an additional test of the signal injection recovery, we injected a constant amplitude into different time segments of data spaced over 100 seconds and observed the spread in best fit and 95% confidence amplitude exclusions, as shown in Figure 6-13 (b). We found that varying the size of the amplitude injected on the same set of segments had very little effect on the spread of values, as is expected based on the results from the varying amplitude injection search in Figure 6-13 (a). For an injected signal of amplitude 50, 100 test segments had a mean best-fit of 48.3 with a standard deviation of 14.45, and a mean 95% confidence on exclusion of 71.2 with a standard deviation of 14.6. For no injected signal, 100 test segments had a mean best-fit of -1.57 with a standard deviation of 14.6, and a mean 95% confidence on exclusion of 21.3 with a standard deviation of 14.7. An amplitude of 21.3 corresponds to a merger about 0.047 meters away.

For the 100 test segments used, 27 segments excluded the existing 50 amplitude signal, if we increase the amplitude to 100 that number drops to 8. The iminuit minuit function requires a guess for the best-fit amplitude, the pipeline cycles through a few amplitude guesses starting with zero, and usually proceeds with zero, however if the first guess is made to be 100 (the same as the input) the number of unjust exclusions is still 8. Obviously during an exclusion search the expected amplitude should indeed

be zero, as we do not observe mergers in the lab visually.

The signal injection search we verified that our GP has a consistent characterization of the null hypothesis from the varying amplitude test, and the pipeline has an ability to provide reasonable exclusions for multiple different data segments.

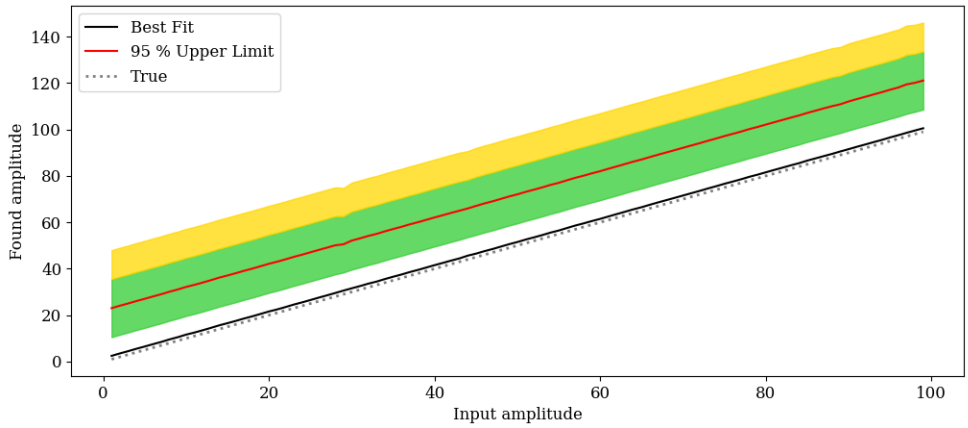

(a)

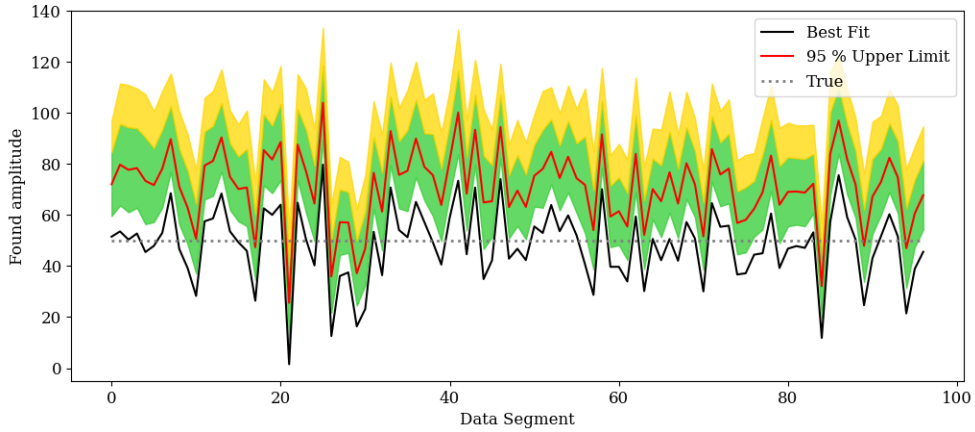

(b)

Figure 6-14: Green bands indicate the 1 σ upper and lower limits on the 95% upper limit confidence level on the amplitude, and gold indicates the 2 σ confidence upper limit. The injected amplitude is marked by the dotted gray line label "True". (a) the signal injection recovery for a single segment of data over injection amplitudes between 1 and 100. (b) the signal injection recovery for many different data segments with a constant amplitude of 50.

6.4.7 Merger Search

To search for a merger, we first take a data segment the length of the template then the processing pipeline is run to find the amplitude of the signal which can be excluded for that individual segment of data. The search is two-sided, meaning the amplitude is permitted to take negative values. In the case of the merger template, a negative amplitude is the signal interacting with the detector at a π difference in direction. The template is created for a specific incoming direction of the GW, however a change in angular direction only has an effect on the amplitude of the signal, and not the shape. Therefore an amplitude can be fit to a distance and set of incoming angles without having to rerun the analysis.

The time step Δt between segments of data processes was determined by running the analysis on a segment with a signal injected at a shifted time. Once the time shift was small enough that the signal was significantly recoverable, that time shift was tested on other segments of data, doubled, and accepted as Δt. We tested this shifting method for two different scenarios, the first for a fixed signal location in the GP, and the second for a floating location. The idea of having the floating location was to have a larger Δt, and therefore less overall segments to process, however floating the location was only more efficient if it did not use more resources floating the location than it saved by having larger time steps. The amount of times the analysis had to be run to process the entire data set was

$$N_{\text{process}} = T/\Delta t - (t_{\text{template}}/\Delta t + 1), \tag{6.25}$$

where T is the total length of the data in time. For 50 segments with an injection of a signal with amplitude 50 we ran the analysis for 4 different signal locations, we fixed the data segment and shifted the template with respect to the segment, the parts of the template that no longer overlapped with the segment were cut. Recall the templates are a total of 30 μs long, and therefore each tested segment is also 30 μs long.

To add the ability to float the location we fix the data segment and allow the fitting function to shift the template with respect to the segment. The location fitting parameters had to be constrained, if the template was allowed to be fit such that the chirp was no longer overlapping and only the in-spiral or ring-down remained those partial templates would create much stronger fits. With these constraints in place, the analysis still had to now fit two free parameters. This new degree of freedom caused multiple failures to converge, and many data segments could not be analyzed. The segments that were analyzed failed to find reasonable fits to an injected signal. In addition, for a signal injection with an amplitude of 50 able to use up to 8 GB memory with 4 CPU it took 237.12 seconds to analyze 10 segments with convergence on all segments without the floating location and it took 283.38 seconds to analyze with the floating location on the same 10 segments, with only 4 successful convergences. From these tests we concluded that the search without the ability to shift location

was proficient for our analysis, and more work in a later analysis would have to be done for the floating location analysis to produce reasonable results.

Parameter	No injection	No shift	0.1 μs	0.2 μs	0.5 μs
Average best fit amplitude	-1.57	48.3	43.03	27.3	-32.2
$\sigma_{\text{best fit}}$	14.61	14.44	14.37	14.5	14.38
Average 95% C.L	21.29	71.19	66.07	50.57	-9
$\sigma_{95\%}$	14.69	14.55	14.5	14.67	14.52
# failed convergences	0	0	3	1	1

Table 6.2: Shifting the signal injection with respect to the data segment without allowing the location to float in the best-fit analysis and testing the signal recovery. The first column with values was ran without a signal injection, the following columns had an injection which was shifted by the listed time. During the testing, a few of the segments failed to converge, the number of segments which failed to converge are listed in the bottom row.

As can be seen in Table 6.2, with a time step of $5\,\mu$s the signal is not only not recovered, it is misinterpreted to have a negative value. The 0.1 μs step provides reasonable 95% confidence level exclusions which were greater than the injected value. As a signal 0.1 μs shifted from the template would recover a signal, we concluded to use $\Delta t = 0.2\,\mu$s without the floating location was a reasonable choice for both recovery ability and computational cost. This time step results in $T = 518459.1\,\text{s} = 144\,\text{hours}$, $N_{\text{process}} = 2.59 \times 10^{12}$ segments to process. This amount of data is not reasonable to process with the GP analysis, which has to construct a new marginalized log-likelihood for each segment processed. Instead we use a sliding window with the same time step ($\Delta t = 0.2\,\mu$s) to find the variance over each minute of data. If a minute-long portion of the data has a variance three sigma away from the norm it is flagged. Results from the GP analysis of the flagged minutes are saved in an array of the best-fit amplitude and Hesse error. We tested the variance over an hour of the full data set, and found one minute with a three-sigma fluctuation away from the mean variance. However this trigger can only be used to find noisy periods of data, and the binary signal would likely average to zero in a variance calculation, so the trigger could only be used to find signals which have a less periodic nature than the binary in the time domain. If we switch to the frequency domain, a high variance could be a signal of signal with increased frequency values, however now the computational costs have once again risen as each window of data would have to be FFT'd.

We presented a pathfinder for the first lumped-element search for HFGW, and were able to show high stability in the data and a sensitivity to both GWs and axions that match theoretical expectations. In future searches at high-frequency it would

be beneficial to have a low-level trigger during the data collection which would only save the segments of data with some signal signature without running the full GP analysis. Additionally, allowing the location of the signal to float in the GP analysis could reduce the number of computations needed, as even one minute of data requires the processing of $\sim 2 \times 10^8$ segments of data.

Chapter 7

Conclusion: GW searches beyond ABRA-GW

Future lumped-element searches can greatly increase their sensitivity to GWs by two methods: changing their pickup geometry as was done with ABRA-GW, or by using a coincidence search with multiple detectors. The multi-detector method requires the detectors to be spaced far enough from each other that their noise is uncorrelated. With correlated signals and uncorrelated noise, the veto power of the analysis will not only increase sensitivity to the axion signal, but also achieve sensitivity to stochastic signals which have never before been detected.

Stochastic signals cannot be searched for with a template, because of their random and fluctuating nature, mimicking a standard noise we expect to see in our detector backgrounds. However, with two detectors positioned sufficiently far apart such that noise correlation is statistically extremely unlikely these stochastic signals can be search for with correlations from the different detectors. The expected normalized energy-density from a stochastic signal is

$$h_0^2 \Omega_{\rm gw}(f) \simeq 3.6 \left(\frac{n_f}{10^{37}}\right) \left(\frac{f}{1{\rm kHz}}\right)^4, \tag{7.1}$$

where h_0 is the normalized Hubble expansion rate, with $\rho_{\rm c} \simeq 1.688 \times 10^{-8} h_0^2$ erg cm^{-3} for the critical density described in Chapter 3, $\Omega_{\rm gw} = \rho_{\rm GW}/\rho_{\rm c}$ is the energy-density of GWs normalized by the critical density, f is the frequency of the wave and n_f is the number of gravitons per cell of phase space. The minimum detectable strain for one detector is

$$[\Omega_{\rm GW}(f)]_{\rm min} = \frac{4\pi^2}{3H_0^2} f^3 S_n(f) \frac{(S/N)^2}{F}, \tag{7.2}$$

for noise spectral density $S_n(f)$, signal-to-noise ratio S/N, angular average of the detector F and f now as the central frequency of the detector bandwidth Δf. For

two detectors taking data simultaneously,

$$[\Omega_{\rm GW}(f)]_{\rm min} \sim \frac{4\pi^2}{3H_0^2}\frac{f^3 S_n(f)}{\sqrt{2T\Delta f}}\frac{(S/N)^2}{F}, \tag{7.3}$$

with integration time T and

$$\frac{1}{\sqrt{2T\Delta f}} \simeq 1\times 10^{-5}\left(\frac{150\text{Hz}}{\Delta f}\right)^{1/2}\left(\frac{1\text{yr}}{T}\right)^{1/2}. \tag{7.4}$$

From one detector to two we gain a factor of $\frac{1}{\sqrt{2T\Delta f}}$, and for two detectors with a bandwidth $\Delta f = 150$ Hz, the sensitivity to the stochastic signal is increase by five orders of magnitude as compared to one detector [84].

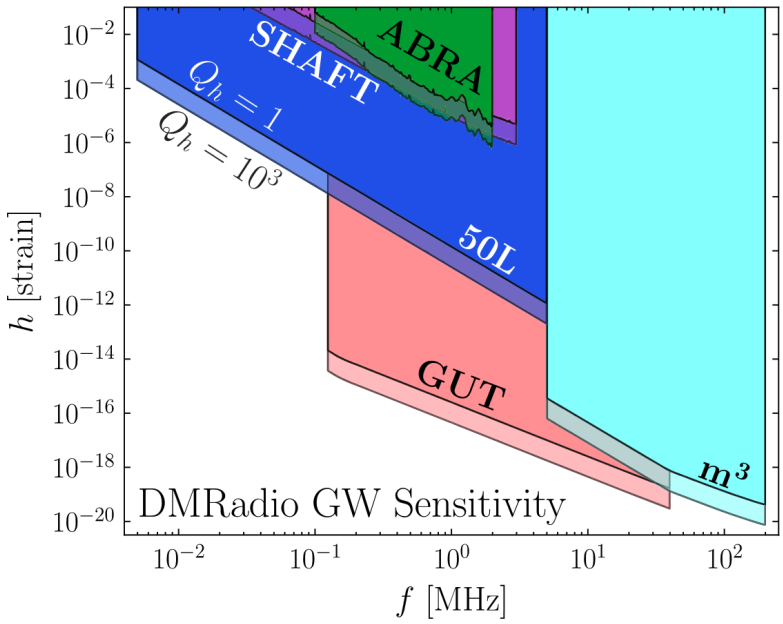

Figure 7-1: Reproduced from [124].

DMR-50L could be converted to search for GWs once it finishes it's axion science run, but the sheath configuration is difficult to geometrically convert for GW detection. However, the data collected in the axion configuration can be used to conduct a search with sensitivity up to ω^3. Considering 50L is a resonant experiment, the sensitivity to the strain is also increased by the quality factor Q, the sensitivity of 50-L in axion configuration is comparable to ABRA-GW. Figure 6-14 shows the theoretical projections of GW sensitivity for DMR-50L. ABRA-GW and DMR-50L have a large overlap in frequency space and similar strain sensitivity, with DMR-50L and ABRA-GW running simultaneously on opposite coasts of the USA, the chances of coincidence noise decrease dramatically, and the experiments are ideal for a stochastic

search.

We have demonstrated the first conversion of a lumped-element axion detector to a GW detector without a decrease in sensitivity to axions. The GW results matched theoretical expectation, and we now have the infrastructure to build more sensitive experiments, and to preform cross-correlation searches with multiple detectors. In the next few decades as axion experiments reach new sensitivities, they can be converted or projected to GW searches and as a community we can broaden our searches for beyond the SM physics.

Appendix A

COMSOL simulations

COMSOL was used simulate both the axion and gravitational wave (GW) signals, since both signals are current densities in the magnet volume, they prove challenging to compute analytically. The main results we derive are for the response of the pickup to one of these signals, either by measuring the current induced in the pickup, or the flux induced within the area of the pickup.

A.1 $\mathcal{G}_V$ COMSOL setup for Run 1

The following sections are named after the associated tabs in the COMSOL simulation, Geometry, Materials, Physics and Mesh. There is also a definitions tab but here only constants and functions are defined so a full section was not necessary.

A.1.1 Geometry

For run 6, a 3D COMSOL simulation is needed to account for the non-symmetric nature of GW loops, which inspired the re-calculation of the Run1 results. In Runs 1-3 a COMSOL 2D axi-symmetric model was used. The 3D geometry is created by simplifying a cross section of the full ABRA cad of the shield and magnet, then revolving the resulting structures. The simplification is necessary to enable the simulation to run, the geometry is too complex to properly mesh otherwise. Figure A.1 shows the simplified cross-section and revolution of the magnet and shield. The use of an air bubble is optional depending on the setup. For the 3D simplified setup, the shield is closed and can be used to define the outer boundary of the simulation. However, for the 2D axi-symmetric simulation, the shield is less simplified and modeled to have a very narrow gap between the two halves, therefore needing an air bubble to define the outer boundary of the simulation. COMSOL will place the mesh points in different places depending on the outer boundary, so in some cases even if the shield can act as the outer boundary, adding the air bubble helped the simulation to run more smoothly.

The default coordinates of the 3D simulation are Cartesian; to use cylindrical coordinates a new coordinate system must be defined under the "Definitions" tab of the Component. To use the cylindrical coordinates "sysm4.–" has to be used, for r and phi. We renamed the coordinates since the default was t1 and t2 for r and phi. This redefinition of the coordinates greatly simplified the inputs of the currents in the Physics section, as the magnet contains azimuthal symmetry.

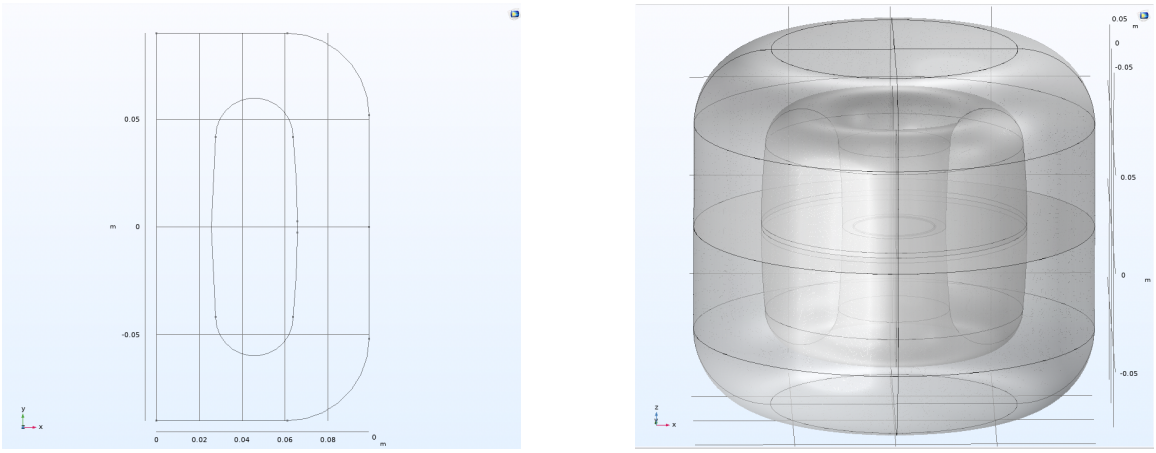

(a) (b)

Figure A-1: (a) shows the simplified cross section from the original ABRA CAD. (b) shows the final geometry, with the revolutions of (a) and the addition of the Run 1 axion pickup loop.

For finding the flux in the pickup, the area of the pickup was defined as a cross-section of a cylinder of the radius of the pickup and the x-y plane. For a pickup current simulation, the Run 1 pickup was modeled as a toroid with the proper dimensions.

A.1.2 Materials

Most of the objects in the 3D geometry were set to be COMSOL-defined air, with the exception of the pickup when the pickup current needed to be found. Since the axion current is an effective current over the volume, the material of the magnet volume is best defined by either the mandrel material (Delrin) which was used in the axi-symmetric model, or air which was used in the 3D models. The boundary of the shield and magnet were not material-defined for the 3D simulations. For the axi-symmetric the shield was set to be standard copper.

If the current on the pickup was needed, the pickup was modeled as superconducting by increasing the conductivity from 5.998e7[S/m] to 5.998e25[S/m]. For the 3D model the only the outside boundary of the pickup was set to be superconducting, otherwise the simulation would not compute. The axi-symmetric simulation did not

have the same issues so both the boundary and the volume of the pickup were set to be superconducting.

A.1.3 Physics

The physics module used for both the 3D and axi-symmetric models was the Magnetic Fields module. The shield is superconducting, which means it stop magnetic fields and sets the outer boundary of the simulation. The COMSOL option of "magnetic insulation" is used to stop the magnet field and simulate the superconducting properties. The magnetic insulation option is the default for the boundary of the simulation, so if an air bubble was used it also had that boundary condition.

The external current is set using the "external current density" option and the cylindrical coordinate system. The axion current is defined in terms of cylindrical coordinates. Depending on the method used, the equation for J_{eff} differs, see section 5.1.1 in the main text for details.

A.1.4 Mesh

The method for meshing the 3D model was developed for the GW simulation, see the next section for details. The 3D mesh was made in an 8-part symmetry using the "fine" size as defined by COMSOL. Since the pickup was in the center of the magnet, the top and bottom were identically meshed. The axi-symmetric mesh was able to use a physic defined mesh of "normal" size as defined by COMSOL.

A.2 COMSOL geometry for Run 6

The purpose of the COMSOL simulations is discussed in detail in the main text Chapter 3.5.1, the abridged version is that we are modeling the GW effective current and finding the pickup response. Figure A.2 shows the output of simulation, plotting the z-component of the magnetic field over two cross-sections. Many of the details of the setup are the same as were used for the $\mathcal{G}_v$ simulations, the main differences being the equations effective current and the shape of the pickup area. Different volumes of the magnet were not tested, for Run 6 we consistently used the mid-winding volume. The physical copper pickup could not be properly meshed as a result of the thin lines and sharp corners and was unnecessary for the purpose of finding the flux on the pickup.

The GW signal is directional, breaking the azimuthal symmetry that existed for the axion signal and necessitating a non-symmetric pickup and therefore a non-symmetric simulation. We can utilize some of the symmetry of our system with the figure-8 pickup loop for the GW at z = 1 cm by modeling the signal over a quarter of the volume, θ_h from 0 to π, and ϕ_h from 0 to $\pi/2$. The other four-thirds of the volume

can be projected from the modeled fourth. A 3D model is needed in COMSOL to recreate the GW setup.

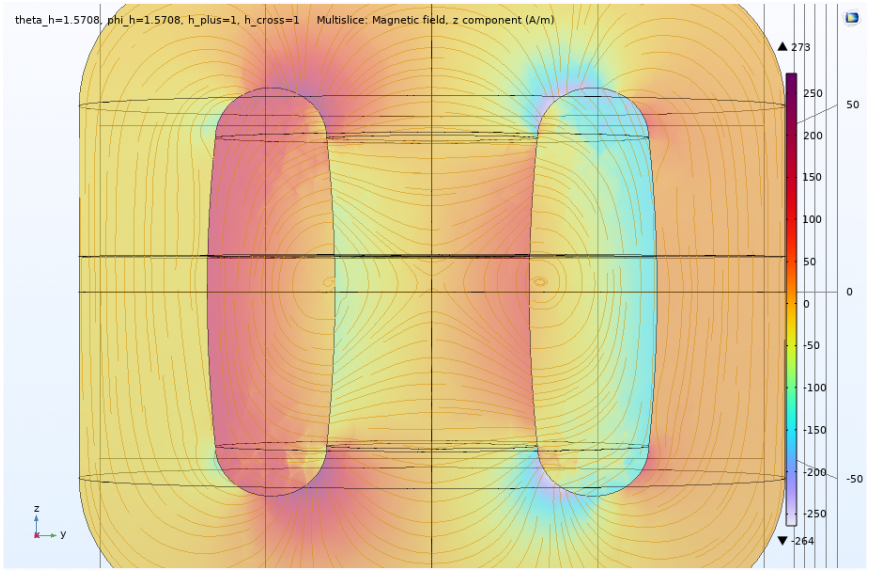

(a)

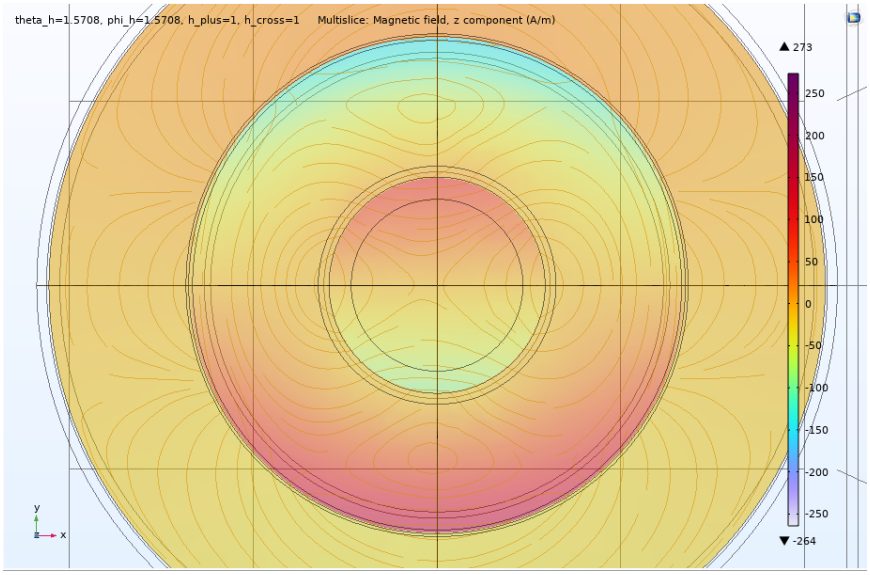

(b)

Figure A-2: Z-component of the magnetic field plotted with COMSOL for an incoming angle of $\theta_h = \pi/2$ and $\theta_h = \pi/2$.(a) Plotted over a cross-section of the x-axis. (b) Plotted over a cross-section of the z-axis.

The difficulty of the GW simulation came primarily from symmetrizing the system. As a result of using terms only up to ω^2 in equation (3.2), the resulting flux in a

circular area should be zero. Testing this assumption, we found it was not zero in COMSOL. We verified the equations were correctly inputted by copying them to tex and comparing the original equations, and we verified the magnet symmetry across the x-y plane. The issue turns out to be a finite element issue and is slightly helped by symmetrizing the mesh. The issue arises from the exact location of each mesh point, we tested the symmetrization on a much simpler system with absolute geometric symmetry and found the error could be reduced only to a point. To determine the value of that error for ABRA-GW setup, we simulated the signal over the figure-8 and circular error and compared the results.

The following results are from a simulation the used the area in the middle of the magnet for the pickup location, i.e. a circle at z = 0, which is not the actual experimental placement for the figure-8. With this geometry, we were able to make an 8-part symmetric mesh. This mesh is built by meshing one eighth of the volume, the copying that mesh onto the neighboring eighth, then that fourth is copied onto the neighboring fourth, and finally the meshed half is copied on the un-meshed half. In addition, a refine level of 2 is placed on the circular area surface and the magnet volume.

The effective current used in the simulation was inflated with h_x and h_x of equal value of 1000 to avoid small-number errors. Small-number errors seem to occur in COMSOL for values on the order of 1e-15. To define the area of the different pickups, the circular area was divided into North and South components which were added for the circular area and subtracted for the figure-8. For a parametric sweep of θ_h and ϕ_h over the half circle, the flux over the area of the figure 8 and the circular were calculated. Figure A.3 shows the results of the magnitude of flux in the z direction for a given pair of angles, it is clear from these plots that the flux in the circle is much smaller than the flux in the figure-8. Before symmetrization efforts, the flux in the circle was only about a factor of two smaller than the flux in the figure-8.

To find the error, we started with the assumption that there should be no cumulative flux in the circular area. We calculated the standard deviation with respect to zero for the circular area over the parametric sweep of incoming wave angles, since the expectation value of the flux is zero. We did the same for the figure-8 to see how far the results differed from zero and took the standard deviation of the circle with respect to zero over standard deviation of the figure-8 with respect to zero to get the errors listed in Table A.1. This method of error estimation is very conservative, since it assumes that none of the flux values for the figure-8 would be zero, which isn't the case. We found that an eight-part mesh greatly reduced the error over the four-part mesh (where the geometry was only split into four identically meshed parts), but the sixteen-part mesh did not show a significant improvement.

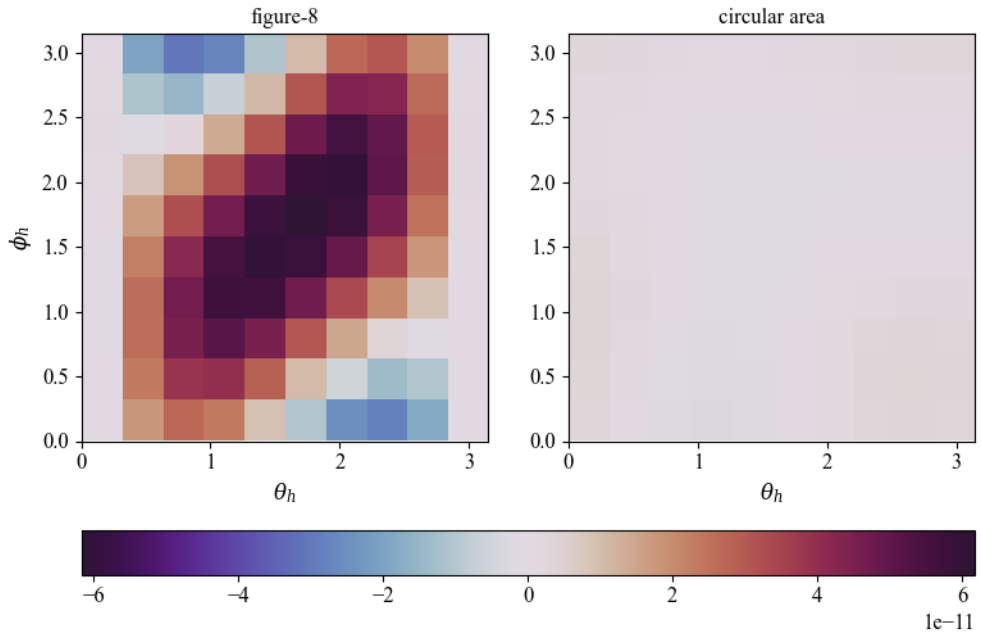

Figure A-3: Each square in the plots is the magnitude of flux in the z-direction for a given pair of angles. The flux values are calculated over the half-sphere. Left: flux calculated over the figure-8 area. Right: flux calculated over the circular area

# of symmetric parts	σ_{circle}	$\sigma_{figure-8}$	$\sigma_{circle}/\sigma_{figure-8}$
Four parts	4.12*1e-12	3.54*1e-11	11.6 %
Eight parts	1.78*1e-12	3.31*1e-11	5.4 %
Sixteen parts	1.84*1e-12	3.49*1e-11	5.3 %

Table A.1: Results for different symmetries of the mesh for the circular area placed at z = 0. σ is the standard deviation calculated with respect to zero for the pickup area over the parametric sweep of incoming wave angles.

To more accurately model the experiment, the circular area representing the figure-8 was moved down to z = -1 cm (the magnet is upside-down). This move decreases the symmetry of the system, now the top and bottom of the magnet must be symmetrized separately. The mesh is still in eight parts, but only four of each are identical. The refinement of the pickup area and magnet volume remains the same.

As discussed in the text, the h_x and h_+ components were simulated separately for the purpose of transforming the templates. The h_x component has over-all larger

magnitudes of flux. We calculated the addition of the two polarizations (see Figure A.3 left) and there are few areas where the h_x and h_+ components add constructively. The points with the greatest overall value for flux maximize h_x and minimizes h_+. As seen in Figure 6-6, these maximum points are around $\phi_h = \theta_h = \pi/2$.

Appendix B

DMRadio

The DMRadio collaboration is searching for low-mass axions with tunable LC resonators. The DMRadio suite of experiments includes 50 L, m^3 and GUT, and will search for axions in the mass range of 20 peV $\lesssim m_a c^2 \lesssim$ 800 neV, reaching the QCD axion band from 0.4 neV to 800 neV.

DMRadio 50 L will cover a frequency range of 5 kHz to 5 MHz (20 peV $\lesssim m_a c^2 \lesssim$ 20 neV) and is in the construction phase at the time of this thesis. The basic design of 50 L includes a toroidal magnet with a 50 L magnetic volume, a superconducting sheath to screen the axion current and a resonant circuit to detect the axion signal. The sheath serves to shield the resonant circuit from the lossy materials of the magnet and allow us to achieve a higher Q value for the circuit. As seen in Figure B-1, 50 L will cover a frequency range that encapsulates the ABRA frequency range, but with a much greater sensitivity that will be achieved with the high-Q resonator and the experiment will additionally serve as a testbed for novel quantum sensors [130].

The DMRadio m^3 experiment is in the design phase, similarly to 50 L, the name of m^3 is in reference to the magnetic volume, but unlike 50 L, m^3 will have a solenoidal magnet. The choice of the solenoid for m^3 is directly related to the frequency range of 5 MHz to 200 MHz (20 neV $\lesssim m_a c^2 \lesssim$ 800 neV), which is higher than 50 L and the magnetoquasistatic approximation mentioned in Chapter 2 starts to fail. DMRadio m^3 will use a series of differently sized cavities to couple to the axion signal, with each cavity corresponding to a different frequency regime. In the high-frequency portion of the m^3 range we are expected to reach the QCD axion band for both KSVZ axions in a mass range of about 40 neV to 800 neV, and DFSZ axions from about 120 neV to 800 neV [131, 130, 132].

DMRadio GUT is still in the conceptual phase, but as the name suggests it will look for GUT-scale axions in a frequency range of around 100 kHz to 30 MHz (0.4 neV $\lesssim m_a c^2 \lesssim$ 120 neV) and will reach the QCD axion band in the full frequency range. As GUT covers a similar frequency band to ABRA and 50 L and does not go as high in frequency as m^3, the plan is to use a toroidal magnet with a 10 m^3 volume. A magnetic volume of this size is difficult to construct with cold superconducting

material, the plan is to use high-temperature superconductors to achieve such a high volume [133].

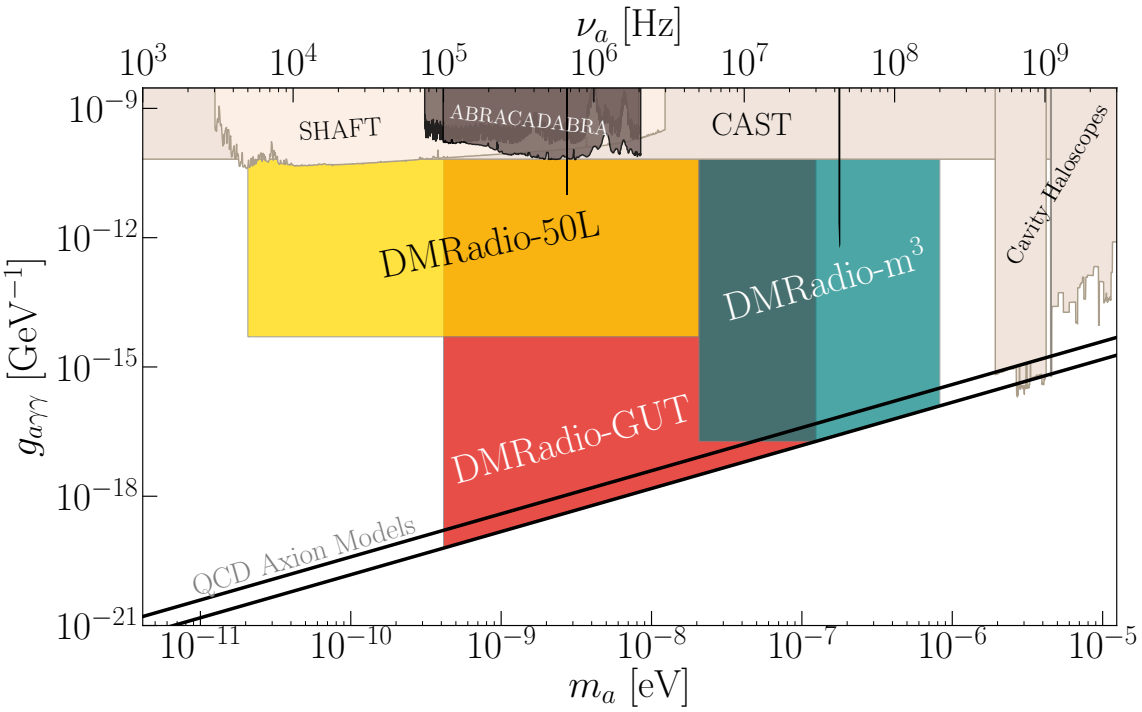

Figure B-1: Projected limits for the DMRadio suite of experiments

Appendix C

Design parameters of ABRA-GW

Specific design parameters used in the final configuration of Run 6, including self and mutual inductances found through simulation in COMSOL.

Detector Design Parameters for ABRA-GW	
Figure-8 Pickup Radius	2.2225 cm
Figure-8 Pickup Height	-1 cm
Circular Pickup Radius	2.2225 cm
Circular Pickup Height	0 cm
Pickups Wire Diameter	170 μm
Figure-8 Calibration Radius	2.2225 cm
Figure-8 Calibration Height	-2 cm
Figure-8 Calibration Wire Diameter	170 μm
Circular Calibration Radius	4.5 cm
Circular Calibration Height	0 cm
Circular Calibration Wire Diameter	500 μm
Figure-8 Self-Inductance	261.64 nH
Circular Pickup Self-Inductance	158 nH
Circular Calibration Self-Inductance	298 nH
Circle to Figure-8 Pickup Mutual-Inductance	2e-5 nH
Circle to Figure-8 Calibration Mutual-Inductance	2.8e-4 nH
Circular Pickup to Figure-8 Calibration Mutual-Inductance	1.4e-4 nH
Figure-8 Pickup to Circular Calibration Mutual-Inductance	- 2.5e-5 nH
Circular Pickup to Circular Calibration Mutual-Inductance	21 nH
Figure-8 Pickup to Figure-8 Calibration Mutual-Inductance	- 28 nH
SQUID Input Inductance	150 nH
SQUID Inductive Coupling	2.5 nH

Table C.1: Design parameters for ABRACADABRA-10cm Run 6 configuration 2, with an axion pickup loop and a GW pickup loop.

Appendix D

Effective Current in Toroidal Magnet

Equations for the effective gravitational wave current in a toroidal volume. Equations are originally from appendix E of [125] and modified with additional terms up to ω^2 for the top and bottom of the magnet, provided by Sung Mook Lee. The results are divided into three parts: one proportional to $\Theta(R+a-\rho)-\Theta(R-\rho)$ describing the volume current, one proportional to $\delta(R+a-\rho)-\delta(R-\rho)$ describing the current on the inside and outside of the volume and one proportional to $\delta(H-2z)-\delta(H+2z)$ describing the top and bottom of the magnet. In the following equations B_{max} is the maximum magnetic field (1 T), H is the height of the magnet (120 [mm]), R is the inner radius of the magnet (30 [mm]), a is the minor diameter of the magnet (30 [mm]) and ω is the angular frequency of the incoming wave. "sin(θ)" and "cos(θ)" have been shortened to "s_θ" and "c_θ" respectively. These equations take $\phi_h = 0$, but ϕ_h can be added back by taking $\phi \to \phi - \phi_h$, which was done when inputting the equations into COMSOL.

$$
\begin{aligned}
j_\rho e^{i\omega t} = & \frac{B_{\max} R}{\rho} \left[\Theta(R+a-\rho) - \Theta(R-\rho)\right] \qquad \text{(D.1)} \\
& \times \Bigg[\frac{1}{12\sqrt{2}} h^+ \omega^2 \left\{ 2z(3+c_{2\theta_h})c_{2\phi} + 6z s_{\theta_h}^2 - \rho c_\phi s_{2\theta_h} \right\} + \frac{1}{6\sqrt{2}} h^\times \omega^2 \left(8z c_{\theta_h} c_\phi - \rho s_{\theta_h} \right) s_\phi \\
& \quad + \frac{i}{192\sqrt{2}} h^+ \omega^3 \Big\{ z\rho \left(-9c_\phi(-11 s_{\theta_h} + s_{3\theta_h}) + 5c_{3\phi}(5 s_{\theta_h} + s_{3\theta_h}) \right) \\
& \qquad\qquad + 2c_{\theta_h} \left((30z^2 - 21\rho^2 + (10z^2+\rho^2)c_{2\theta_h})c_{2\phi} + (24z^2 - 2\rho^2)s_{\theta_h}^2 \right) \Big\} \\
& \quad + \frac{i}{48\sqrt{2}} h^\times \omega^3 \left\{ 2\left(5z^2 - 4\rho^2 + (5z^2-\rho^2)c_{2\theta_h}\right) s_{2\phi} + z\rho s_{2\theta_h}(9 s_\phi + 5 s_{3\phi}) \right\} \Bigg] \\
& + B_{\max} R \left[\delta(H-2z) - \delta(H+2z) \right] \\
& \times \Bigg[\frac{1}{12\sqrt{2}\rho} \omega^2 \Big\{ h^+ ((z^2+2\rho^2)(3+c_{2\theta_h})c_{2\phi} + 2z s_{\theta_h}(-4\rho c_{\theta_h} c_\phi + 3z s_{\theta_h})) \\
& \qquad\qquad + h^\times 4(-2z\rho s_{\theta_h} s_\phi + (z^2+2\rho^2)c_{\theta_h} s_{2\phi}) \Big\} \Bigg]
\end{aligned}
$$

$$
\begin{aligned}
j_\phi e^{i\omega t} = & \frac{B_{\max} R}{\rho} \left[\Theta(R+a-\rho) - \Theta(R-\rho)\right] \\
& \times \Bigg[\frac{-1}{6\sqrt{2}} h^+ \omega^2 \left\{ z(3+c_{2\theta_h}) c_\phi + \rho s_{2\theta_h} \right\} s_\phi + \frac{1}{3\sqrt{2}} h^\times \omega^2 \left(z c_{\theta_h} c_{2\phi} + \rho c_\phi s_{\theta_h} \right) \\
& \quad - \frac{i}{64\sqrt{2}} h^+ \omega^3 \Big\{ 4 c_{\theta_h} \left(3z^2 + \rho^2 + (z^2 - \rho^2) c_{2\theta_h} \right) s_{2\phi} + z\rho s_{3\theta_h} (5 s_\phi + s_{3\phi}) \\
& \qquad\qquad + z\rho s_{\theta_h} (9 s_\phi + 5 s_{3\phi}) \Big\} \\
& \quad + \frac{i}{16\sqrt{2}} h^\times \omega^3 \left\{ (2z^2 + \rho^2) c_{2\phi} - c_{2\theta_h} \left(\rho^2 + (-2z^2 + \rho^2) c_{2\phi} \right) + \rho(\rho + 4 z c_\phi^3 s_{2\theta_h}) \right\} \Bigg] \\
& + B_{\max} R \left[\delta(R+a-\rho) - \delta(R-\rho) \right] \\
& \times \Bigg[\frac{-1}{12\sqrt{2}} h^+ \omega^2 \left\{ z(3+c_{2\theta_h}) c_\phi + \rho s_{2\theta_h} \right\} s_\phi - \frac{1}{6\sqrt{2}} h^\times \omega^2 \left(z c_{\theta_h} c_{2\phi} + \rho c_\phi s_{\theta_h} \right) \\
& \quad - \frac{i}{48\sqrt{2}} h^+ \omega^3 \left(z c_{\theta_h} + \rho c_\phi s_{\theta_h} \right) \left(2\rho s_{2\theta_h} s_\phi + z(3 + c_{2\theta_h}) s_{2\phi} \right) \\
& \quad - \frac{i}{12\sqrt{2}} h^\times \omega^3 \left(z c_{\theta_h} + \rho c_\phi s_{\theta_h} \right) \left(z c_{\theta_h} c_{2\phi} + \rho c_\phi s_{\theta_h} \right) \Bigg], \\
& + B_{\max} R \left[\delta(H - 2z) - \delta(H + 2z) \right] \\
& \times \Bigg[\frac{1}{12\sqrt{2}\rho} z \omega^2 \Big\{ h^+ (2\rho s_{2\theta_h} s_\phi + z(3 + c_{2\theta_h}) s_{2\phi})) - h^\times 4 (z c_{\theta_h} c_{2\phi} + \rho c_\phi s_{\theta_h}) \Big\} \Bigg]
\end{aligned}
\tag{D.2}
$$

$$
\begin{aligned}
j_z e^{i\omega t} = & \frac{B_{\max} R}{\rho^2}\left[\Theta(R+a-\rho)-\Theta(R-\rho)\right] \\
& \times\Bigg[\frac{1}{12\sqrt{2}}h^{+}\omega^2\left\{(z^2-2\rho^2)(3+c_{2\theta_h})c_{2\phi}+3z\rho c_\phi s_{2\theta_h}\right\} \\
& +\frac{1}{6\sqrt{2}}h^{\times}\omega^2\left\{4(z^2-2\rho^2)c_{\theta_h}c_\phi+3z\rho s_{\theta_h}\right\}s_\phi \\
& -\frac{i}{192\sqrt{2}}h^{+}\omega^3\Big\{2z(2z^2-7\rho^2)(7c_{\theta_h}+c_{3\theta_h})c_{2\phi}+8z\rho^2 c_{\theta_h}s_{\theta_h}^2 \\
& \qquad +\rho c_\phi\big[(50z^2-9\rho^2+5(4z^2-9\rho^2)c_{2\phi})s_{\theta_h} \\
& \qquad\quad +(10z^2+3\rho^2+(4z^2-9\rho^2)c_{2\phi})s_{3\theta_h}\big]\Big\} \\
& +\frac{i}{48\sqrt{2}}h^{\times}\omega^3\left\{\rho\left(14z^2-9\rho^2+(4z^2-9\rho^2)c_{2\phi}\right)s_{2\theta_h}s_\phi+4z(2z^2-7\rho^2)c_{\theta_h}^2 s_{2\phi}\right\}\Bigg] \\
& +\frac{B_{\max}R}{\rho}\left[\delta(R+a-\rho)-\delta(R-\rho)\right] \\
& \times\Bigg[\frac{1}{24\sqrt{2}}h^{+}\omega^2\left\{(z^2+2\rho^2)(3+c_{2\theta_h})c_{2\phi}+2zs_{\theta_h}(-4\rho c_{\theta_h}c_\phi+3zs_{\theta_h})\right\} \\
& +\frac{1}{3\sqrt{2}}h^{\times}\omega^2\left[(z^2+2\rho^2)c_{\theta_h}c_\phi-z\rho s_{\theta_h}\right]s_\phi \\
& -\frac{i}{192\sqrt{2}}h^{+}\omega^3\Big\{\rho c_\phi\left[(8z^2+3\rho^2+5(2z^2+3\rho^2)c_{2\phi})s_{\theta_h}\right. \\
& \qquad\qquad \left.+(-8z^2-\rho^2+(2z^2+3\rho^2)c_{2\phi})s_{3\theta_h}\right] \\
& \qquad +2zc_{\theta_h}\left((6z^2+7\rho^2+(2z^2+5\rho^2)c_{2\theta_h})c_{2\phi}+(8z^2-2\rho^2)s_{\theta_h}^2\right)\Big\} \\
& -\frac{i}{48\sqrt{2}}h^{\times}\omega^3\left\{\rho(3\rho^2+(2z^2+3\rho^2)c_{2\phi})s_{2\theta_h}s_\phi+2z(z^2+\rho^2+(z^2+2\rho^2)c_{2\theta_h})s_{2\phi}\right\}\Bigg]
\end{aligned}
\tag{D.3}
$$

Bibliography

[1] Markus Kuster. *Axions - Theory, Cosmology and Experimental Searches*, volume 741. 12 2007.

[2] C. Abel et al. Measurement of the permanent electric dipole moment of the neutron. *Physical Review Letters*, 124(8), February 2020.

[3] R. D. Peccei and Helen R. Quinn. CP conservation in the presence of pseudoparticles. *Phys. Rev. Lett.*, 38:1440–1443, Jun 1977.

[4] Michael S. Turner Edward W. Kolb. *The Early Universe (1st ed.): Axions*, volume 1st Edition. 12 1990.

[5] Steven Weinberg. A new light boson? *Phys. Rev. Lett.*, 40:223–226, Jan 1978.

[6] F. Wilczek. Problem of strong p and t invariance in the presence of instantons. *Phys. Rev. Lett.*, 40:279–282, Jan 1978.

[7] John Preskill, Mark B. Wise, and Frank Wilczek. Cosmology of the invisible axion. *Physics Letters B*, 120(1):127–132, 1983.

[8] Jihn E. Kim. Weak-interaction singlet and strong CP invariance. *Phys. Rev. Lett.*, 43:103–107, Jul 1979.

[9] M.A. Shifman, A.I. Vainshtein, and V.I. Zakharov. Can confinement ensure natural cp invariance of strong interactions? *Nuclear Physics B*, 166(3):493–506, 1980.

[10] Michael Dine, Willy Fischler, and Mark Srednicki. A simple solution to the strong cp problem with a harmless axion. *Physics Letters B*, 104(3):199–202, 1981.

[11] A P Zhitnitskii. Possible suppression of axion-hadron interactions. *Sov. J. Nucl. Phys. (Engl. Transl.); (United States)*, 312, 2 1980.

[12] L. Baudis and S. Profumo. 26. dark matter. *Particle Data Group*, 100, 2019.

[13] Jonathan Ouellet and Zachary Bogorad. Solutions to axion electrodynamics in various geometries. *Phys. Rev. D*, 99:055010, Mar 2019.

[14] Ciaran O'Hare. cajohare/axionlimits: Axionlimits. https://cajohare.github.io/AxionLimits/, July 2020.

[15] P. Sikivie. Experimental tests of the "invisible" axion. *Phys. Rev. Lett.*, 51:1415–1417, Oct 1983.

[16] Pierre Sikivie. Invisible axion search methods. *Reviews of Modern Physics*, 93(1), February 2021.

[17] P. Sikivie. Detection rates for "invisible"-axion searches. *Phys. Rev. D*, 32:2988–2991, Dec 1985.

[18] Lawrence Krauss, John Moody, Frank Wilczek, and Donald E. Morris. Calculations for cosmic axion detection. *Phys. Rev. Lett.*, 55:1797–1800, Oct 1985.

[19] DICKE R. H. The measurement of thermal radiation at microwave frequencies. *The Review of scientific instruments*, 17:268–275, Jul 1946.

[20] T. Braine et al. Extended search for the invisible axion with the axion dark matter experiment. *Physical Review Letters*, 124(10), March 2020.

[21] Paolo Gondolo and Georg G. Raffelt. Solar neutrino limit on axions and kev-mass bosons. *Physical Review D*, 79(10), May 2009.

[22] Georg G. Raffelt. *Astrophysical Axion Bounds*, page 51–71. Springer Berlin Heidelberg.

[23] E Arik, S Aune, D Autiero, K Barth, A Belov, B Beltrán, S Borghi, G Bourlis, F.S Boydag, H Bräuninger, J.M Carmona, S Cebrián, S.A Cetin, J.I Collar, T Dafni, M Davenport, L. Di Lella, O.B Dogan, C Eleftheriadis, N Elias, G Fanourakis, E Ferrer-Ribas, H Fischer, P Friedrich, J Franz, J Galán, T Geralis, I Giomataris, S Gninenko, H Gómez, R Hartmann, M Hasinoff, F.H Heinsius, I Hikmet, D.H.H Hoffmann, I.G Irastorza, J Jacoby, K Jakovčić, D Kang, K Königsmann, R Kotthaus, M Krčmar, K Kousouris, M Kuster, B Lakić, C Lasseur, A Liolios, A Ljubičić, G Lutz, G Luzón, D Miller, J Morales, T Niinikoski, A Nordt, A Ortiz, T Papaevangelou, M.J Pivovaroff, A Placci, G Raffelt, H Riege, A Rodríguez, J Ruz, I Savvidis, Y Semertzidis, P Serpico, R Soufli, L Stewart, K. van Bibber, J Villar, J Vogel, L Walckiers, and K Zioutas. Probing ev-scale axions with cast. *Journal of Cosmology and Astroparticle Physics*, 2009(02):008–008, February 2009.

[24] New cast limit on the axion–photon interaction. *Nature Physics*, 13(6):584–590, May 2017.

[25] E Armengaud, F T Avignone, M Betz, P Brax, P Brun, G Cantatore, J M Carmona, G P Carosi, F Caspers, S Caspi, S A Cetin, D Chelouche, F E Christensen, A Dael, T Dafni, M Davenport, A V Derbin, K Desch, A Diago, B Döbrich, I Dratchnev, A Dudarev, C Eleftheriadis, G Fanourakis, E Ferrer-Ribas, J Galán, J A García, J G Garza, T Geralis, B Gimeno, I Giomataris, S Gninenko, H Gómez, D González-Díaz, E Guendelman, C J Hailey, T Hiramatsu, D H H Hoffmann, D Horns, F J Iguaz, I G Irastorza, J Isern, K Imai, A C Jakobsen, J Jaeckel, K Jakovčić, J Kaminski, M Kawasaki, M Karuza, M Krčmar, K Kousouris, C Krieger, B Lakić, O Limousin, A Lindner, A Liolios, G Luzón, S Matsuki, V N Muratova, C Nones, I Ortega, T Papaevangelou, M J Pivovaroff, G Raffelt, J Redondo, A Ringwald, S Russenschuck, J Ruz, K Saikawa, I Savvidis, T Sekiguchi, Y K Semertzidis, I Shilon, P Sikivie, H Silva, H ten Kate, A Tomas, S Troitsky, T Vafeiadis, K van Bibber, P Vedrine, J A Villar, J K Vogel, L Walckiers, A Weltman, W Wester, S C Yildiz, and K Zioutas. Conceptual design of the international axion observatory (iaxo). *Journal of Instrumentation*, 9(05):T05002–T05002, May 2014.

[26] K. Van Bibber, N. R. Dagdeviren, S. E. Koonin, A. K. Kerman, and H. N. Nelson. Proposed experiment to produce and detect light pseudoscalars. *Phys. Rev. Lett.*, 59:759–762, Aug 1987.

[27] P. Sikivie, D. B. Tanner, and Karl van Bibber. Resonantly enhanced axion-photon regeneration. *Physical Review Letters*, 98(17), April 2007.

[28] Guido Mueller, Pierre Sikivie, D. B. Tanner, and Karl van Bibber. Detailed design of a resonantly enhanced axion-photon regeneration experiment. *Physical Review D*, 80(7), October 2009.

[29] Yukio Fukuda, Toshiro Kohmoto, Shin ichi Nakajima, and Masakuzu Kunitomo. Production and detection of axions by using optical resonators. *Progress in Crystal Growth and Characterization of Materials*, 33(1):363–366, 1996.

[30] P. Sikivie, D. B. Tanner, and Karl van Bibber. Resonantly enhanced axion-photon regeneration. *Phys. Rev. Lett.*, 98:172002, Apr 2007.

[31] M. Diaz Ortiz, J. Gleason, H. Grote, A. Hallal, M.T. Hartman, H. Hollis, K.-S. Isleif, A. James, K. Karan, T. Kozlowski, A. Lindner, G. Messineo, G. Mueller, J.H. Põld, R.C.G. Smith, A.D. Spector, D.B. Tanner, L.-W. Wei, and B. Willke. Design of the alps ii optical system. *Physics of the Dark Universe*, 35:100968, 2022.

[32] Jonathan L. Ouellet, Chiara P. Salemi, Joshua W. Foster, Reyco Henning, Zachary Bogorad, Janet M. Conrad, Joseph A. Formaggio, Yonatan Kahn, Joe Minervini, Alexey Radovinsky, Nicholas L. Rodd, Benjamin R. Safdi, Jesse Thaler, Daniel Winklehner, and Lindley Winslow. Design and implementation

of the ABRACADABRA-10 cm axion dark matter search. *Physical Review D*, 99(5), mar 2019.

[33] Jonathan L. Ouellet, Chiara P. Salemi, Joshua W. Foster, Reyco Henning, Zachary Bogorad, Janet M. Conrad, Joseph A. Formaggio, Yonatan Kahn, Joe Minervini, Alexey Radovinsky, Nicholas L. Rodd, Benjamin R. Safdi, Jesse Thaler, Daniel Winklehner, and Lindley Winslow. First results from abracadabra-10 cm: A search for sub-μeV axion dark matter. *Phys. Rev. Lett.*, 122:121802, Mar 2019.

[34] Alexander V. Gramolin, Deniz Aybas, Dorian Johnson, Janos Adam, and Alexander O. Sushkov. Search for axion-like dark matter with ferromagnets. *Nature Physics*, 17(1):79–84, August 2020.

[35] Yonatan Kahn, Benjamin R. Safdi, and Jesse Thaler. Broadband and resonant approaches to axion dark matter detection. *Physical Review Letters*, 117(14), sep 2016.

[36] Jesse Liu, Kristin Dona, Gabe Hoshino, Stefan Knirck, Noah Kurinsky, Matthew Malaker, David W. Miller, Andrew Sonnenschein, Mohamed H. Awida, Peter S. Barry, Karl K. Berggren, Daniel Bowring, Gianpaolo Carosi, Clarence Chang, Aaron Chou, Rakshya Khatiwada, Samantha Lewis, Juliang Li, Sae Woo Nam, Omid Noroozian, and Tony X. Zhou. Broadband solenoidal haloscope for terahertz axion detection. *Phys. Rev. Lett.*, 128:131801, Mar 2022.

[37] F. Zwicky. Republication of: The redshift of extragalactic nebulae. *General Relativity and Gravitation*, 41(1):207–224, January 2009.

[38] V. C. Rubin, Jr. Ford, W. K., and N. Thonnard. Rotational properties of 21 SC galaxies with a large range of luminosities and radii, from NGC 4605 (R=4kpc) to UGC 2885 (R=122kpc). *apj*, 238:471–487, June 1980.

[39] J. Anthony Tyson, Greg P. Kochanski, and Ian P. Dell'Antonio. Detailed mass map of cl 0024+1654 from strong lensing. *The Astrophysical Journal*, 498(2):L107, apr 1998.

[40] Aaron D. Lewis, David A. Buote, and John T. Stocke. Chandra observations of a2029: The dark matter profile down to below 0.01rvir in an unusually relaxed cluster. *The Astrophysical Journal*, 586(1):135, mar 2003.

[41] E. Komatsu, K. M. Smith, J. Dunkley, C. L. Bennett, B. Gold, G. Hinshaw, N. Jarosik, D. Larson, M. R. Nolta, L. Page, D. N. Spergel, M. Halpern, R. S. Hill, A. Kogut, M. Limon, S. S. Meyer, N. Odegard, G. S. Tucker, J. L. Weiland, E. Wollack, and E. L. Wright. Seven-year wilkinson microwave anisotropy probe (wmap) observations: Cosmological interpretation. *The Astrophysical Journal Supplement Series*, 192(2):18, January 2011.

[42] Daniel J. Eisenstein et al. Detection of the baryon acoustic peak in the large-scale correlation function of sdss luminous red galaxies. *The Astrophysical Journal*, 633(2):560–574, November 2005.

[43] Bing-Lin Young. A survey of dark matter and related topics in cosmology. *Fronteirs of Physics*, 12(121201), 2017.

[44] Raul E. Angulo and Oliver Hahn. Large-scale dark matter simulations. *Living Reviews in Computational Astrophysics*, 8(1), February 2022.

[45] N. Aghanim et al. Planck2018 results: Vi. cosmological parameters. *Astronomy & Astrophysics*, 641:A6, September 2020.

[46] Alan H. Guth. Inflationary universe: A possible solution to the horizon and flatness problems. *Phys. Rev. D*, 23:347–356, Jan 1981.

[47] Matthias Bartelmann and Peter Schneider. Weak gravitational lensing. *Physics Reports*, 340(4–5):291–472, January 2001.

[48] Douglas Clowe, Maruša Bradač, Anthony H. Gonzalez, Maxim Markevitch, Scott W. Randall, Christine Jones, and Dennis Zaritsky. A direct empirical proof of the existence of dark matter. *The Astrophysical Journal*, 648(2):L109–L113, August 2006.

[49] B.P. Abbott and others. Observation of gravitational waves from a binary black hole merger. *Physical Review Letters*, 116(6), February 2016.

[50] Matts Roos. Dark matter: The evidence from astronomy, astrophysics and cosmology, 2010.

[51] Leszek Roszkowski, Enrico Maria Sessolo, and Sebastian Trojanowski. WIMP dark matter candidates and searches—current status and future prospects. 81(6):066201, may 2018.

[52] Marc Schumann. Direct detection of WIMP dark matter: concepts and status. 46(10):103003, aug 2019.

[53] Rebecca K. Leane, Tracy R. Slatyer, John F. Beacom, and Kenny C. Y. Ng. Gev-scale thermal wimps: Not even slightly ruled out. *Phys. Rev. D*, 98:023016, Jul 2018.

[54] D. S. Akerib, P. B. Cushman, C. E. Dahl, R. Ebadi, A. Fan, R. J. Gaitskell, C. Galbiati, G. K. Giovanetti, Graciela B. Gelmini, L. Grandi, S. J. Haselschwardt, C. M. Jackson, R. F. Lang, B. Loer, D. Loomba, M. C. Marshall, A. F. Mills, C. A. J. OHare, C. Savarese, J. Schueler, M. Szydagis, Volodymyr Takhistov, Tim M. P. Tait, Y. D. Tsai, S. E. Vahsen, R. L. Walsworth, and

S. Westerdale. Snowmass2021 cosmic frontier dark matter direct detection to the neutrino fog, 2022.

[55] K. Hirata, T. Kajita, M. Koshiba, M. Nakahata, Y. Oyama, N. Sato, A. Suzuki, M. Takita, Y. Totsuka, T. Kifune, T. Suda, K. Takahashi, T. Tanimori, K. Miyano, M. Yamada, E. W. Beier, L. R. Feldscher, S. B. Kim, A. K. Mann, F. M. Newcomer, R. Van, W. Zhang, and B. G. Cortez. Observation of a neutrino burst from the supernova sn1987a. *Phys. Rev. Lett.*, 58:1490–1493, Apr 1987.

[56] R. M. Bionta, G. Blewitt, C. B. Bratton, D. Casper, A. Ciocio, R. Claus, B. Cortez, M. Crouch, S. T. Dye, S. Errede, G. W. Foster, W. Gajewski, K. S. Ganezer, M. Goldhaber, T. J. Haines, T. W. Jones, D. Kielczewska, W. R. Kropp, J. G. Learned, J. M. LoSecco, J. Matthews, R. Miller, M. S. Mudan, H. S. Park, L. R. Price, F. Reines, J. Schultz, S. Seidel, E. Shumard, D. Sinclair, H. W. Sobel, J. L. Stone, L. R. Sulak, R. Svoboda, G. Thornton, J. C. van der Velde, and C. Wuest. Observation of a neutrino burst in coincidence with supernova 1987a in the large magellanic cloud. *Phys. Rev. Lett.*, 58:1494–1496, Apr 1987.

[57] G. G. Raffelt. *Stars as laboratories for fundamental physics: The astrophysics of neutrinos, axions, and other weakly interacting particles*. 5 1996.

[58] Alexandre Payez, Carmelo Evoli, Tobias Fischer, Maurizio Giannotti, Alessandro Mirizzi, and Andreas Ringwald. Revisiting the sn1987a gamma-ray limit on ultralight axion-like particles. *Journal of Cosmology and Astroparticle Physics*, 2015(02):006–006, February 2015.

[59] Manuel Meyer and Tanja Petrushevska. Search for axionlike-particle-induced prompt x-ray emission from extragalactic core-collapse supernovae with the fermi large area telescope. *Physical Review Letters*, 124(23), June 2020.

[60] Francesca Calore, Pierluca Carenza, Maurizio Giannotti, Joerg Jaeckel, and Alessandro Mirizzi. Bounds on axionlike particles from the diffuse supernova flux. *Physical Review D*, 102(12), December 2020.

[61] Georg G. Raffelt, Javier Redondo, and Nicolas Viaux Maira. The mev mass frontier of axion physics. *Physical Review D*, 84(10), November 2011.

[62] Adrian Ayala, Inma Domínguez, Maurizio Giannotti, Alessandro Mirizzi, and Oscar Straniero. Revisiting the bound on axion-photon coupling from globular clusters. *Physical Review Letters*, 113(19), November 2014.

[63] Matthew J. Dolan, Frederick J. Hiskens, and Raymond R. Volkas. Advancing globular cluster constraints on the axion-photon coupling. *Journal of Cosmology and Astroparticle Physics*, 2022(10):096, October 2022.

[64] Thomas Constantino, Simon W. Campbell, John C. Lattanzio, and Adam van Duijneveldt. The treatment of mixing in core helium burning models – ii. constraints from cluster star counts. *Monthly Notices of the Royal Astronomical Society*, 456(4):3866–3885, January 2016.

[65] A. H. Córsico, L. G. Althaus, M. M. Miller Bertolami, A. D. Romero, E. García-Berro, J. Isern, and S. O. Kepler. The rate of cooling of the pulsating white dwarf star g117 b15a: a new asteroseismological inference of the axion mass: A new inference of the axion mass. *Monthly Notices of the Royal Astronomical Society*, 424(4):2792–2799, July 2012.

[66] A. Bischoff-Kim, M. H. Montgomery, and D. E. Winget. Strong limits on the dfsz axion mass with g117-b15a. *The Astrophysical Journal*, 675(2):1512–1517, March 2008.

[67] A.H Córsico, L.G Althaus, A.D Romero, A.S Mukadam, E García-Berro, J Isern, S.O Kepler, and M.A Corti. An independent limit on the axion mass from the variable white dwarf star r548. *Journal of Cosmology and Astroparticle Physics*, 2012(12):010–010, December 2012.

[68] Maurizio Giannotti. Alp hints from cooling anomalies, 2015.

[69] Maurizio Giannotti, Igor G. Irastorza, Javier Redondo, Andreas Ringwald, and Ken'ichi Saikawa. Stellar recipes for axion hunters. *Journal of Cosmology and Astroparticle Physics*, 2017(10):010–010, October 2017.

[70] Christopher Dessert, Andrew J. Long, and Benjamin R. Safdi. X-ray signatures of axion conversion in magnetic white dwarf stars. *Phys. Rev. Lett.*, 123:061104, Aug 2019.

[71] Christopher Dessert, Andrew J. Long, and Benjamin R. Safdi. No evidence for axions from chandra observation of the magnetic white dwarf re j0317-853. *Physical Review Letters*, 128(7), February 2022.

[72] B. P. Abbott et al. Observation of gravitational waves from a binary black hole merger. *Phys. Rev. Lett.*, 116:061102, Feb 2016.

[73] Anne M Green and Bradley J Kavanagh. Primordial black holes as a dark matter candidate. *Journal of Physics G: Nuclear and Particle Physics*, 48(4):043001, Feb 2021.

[74] Ilia Musco. Threshold for primordial black holes: Dependence on the shape of the cosmological perturbations. *Phys. Rev. D*, 100:123524, Dec 2019.

[75] Maximiliano Isi. Recent ligo-virgo discoveries. *Modern Physics Letters A*, 36(11):2130010, March 2021.

[76] Pablo Villanueva-Domingo, Olga Mena, and Sergio Palomares-Ruiz. A brief review on primordial black holes as dark matter. *Frontiers in Astronomy and Space Sciences*, 8, May 2021.

[77] Nanograv Collaboration. The NANOGrav 15 yr Data Set: Constraints on Supermassive Black Hole Binaries from the Gravitational-wave Background. *apjl*, 952(2):L37, August 2023.

[78] Zhi-Chao Zhao and Sai Wang. Bayesian implications for the primordial black holes from nanograv's pulsar-timing data using the scalar-induced gravitational waves. *Universe*, 9(4):157, March 2023.

[79] Denys Malyshev, Emmanuel Moulin, and Andrea Santangelo. Limits on the primordial black holes dark matter with current and future missions, 2023.

[80] Bradley J. Kavanagh. bradkav/pbhbounds: Release version. 2019.

[81] S. et al. Chatrchyan. Observation of a new boson at a mass of 125 gev with the cms experiment at the lhc. *Physics Letters B*, 716(1):30–61, September 2012.

[82] G. et al. Aad. Observation of a new particle in the search for the standard model higgs boson with the atlas detector at the lhc. *Physics Letters B*, 716(1):1–29, September 2012.

[83] B. P. Abbott et al. Prospects for observing and localizing gravitational-wave transients with advanced ligo, advanced virgo and kagra. *Living Reviews in Relativity*, 23(1), September 2020.

[84] Michele Maggiore. 3357 Data analysis techniques. In *Gravitational Waves: Volume 1: Theory and Experiments*. Oxford University Press, 10 2007.

[85] Michele Maggiore. 1674 Applications. In *Gravitational Waves: Volume 1: Theory and Experiments*. Oxford University Press, 10 2007.

[86] Erika M. Holmbeck, Anna Frebel, G. C. McLaughlin, Rebecca Surman, Rodrigo Fernández, Brian D. Metzger, Matthew R. Mumpower, and T. M. Sprouse. Reconstructing masses of merging neutron stars from stellar r-process abundance signatures. *The Astrophysical Journal*, 909(1):21, March 2021.

[87] Michele Maggiore. 644Stochastic backgrounds of cosmological origin. In *Gravitational Waves: Volume 2: Astrophysics and Cosmology*. Oxford University Press, 03 2018.

[88] Wayne Hu and Martin White. A cmb polarization primer. *New Astronomy*, 2(4):323–344, October 1997.

[89] Arthur Kosowsky. Cosmic microwave background polarization. *Annals of Physics*, 246(1):49–85, February 1996.

[90] P.A.R. Ade et al. Detection of<mml:math xmlns:mml="http://www.w3.org/1998/math/mathml" display="inline"><mml:mi>b</mml:mi></mml:math>-mode polarization at degree angular scales by bicep2. *Physical Review Letters*, 112(24), June 2014.

[91] P.A.R. Ade et al. Joint analysis of bicep2/keck arrayandplanckdata. *Physical Review Letters*, 114(10), March 2015.

[92] Nicola Bartolo, Chiara Caprini, Valerie Domcke, Daniel G. Figueroa, Juan Garcia-Bellido, Maria Chiara Guzzetti, Michele Liguori, Sabino Matarrese, Marco Peloso, Antoine Petiteau, Angelo Ricciardone, Mairi Sakellariadou, Lorenzo Sorbo, and Gianmassimo Tasinato. Science with the space-based interferometer lisa. iv: probing inflation with gravitational waves. *Journal of Cosmology and Astroparticle Physics*, 2016(12):026–026, December 2016.

[93] Neil Barnaby and Marco Peloso. Large non-gaussianity in axion inflation. *Physical Review Letters*, 106(18), May 2011.

[94] Asimina Arvanitaki, Savas Dimopoulos, Sergei Dubovsky, Nemanja Kaloper, and John March-Russell. String axiverse. *Physical Review D*, 81(12), June 2010.

[95] Hua Zhai, Si-Yu Li, Mingzhe Li, and Xinmin Zhang. Joint constraint on primordial gravitational waves and polarization rotation angle with current cmb polarization data. *Physics Letters B*, 802:135240, 2020.

[96] Ken K. Y. Ng, Salvatore Vitale, Will M. Farr, and Carl L. Rodriguez. Probing multiple populations of compact binaries with third-generation gravitational-wave detectors. *The Astrophysical Journal Letters*, 913(1):L5, May 2021.

[97] Marica Branchesi et al. Science with the einstein telescope: a comparison of different designs. *Journal of Cosmology and Astroparticle Physics*, 2023(07):068, July 2023.

[98] Nancy Aggarwal, Odylio D. Aguiar, Andreas Bauswein, Giancarlo Cella, Sebastian Clesse, Adrian Michael Cruise, Valerie Domcke, Daniel G. Figueroa, Andrew Geraci, Maxim Goryachev, Hartmut Grote, Mark Hindmarsh, Francesco Muia, Nikhil Mukund, David Ottaway, Marco Peloso, Fernando Quevedo, Angelo Ricciardone, Jessica Steinlechner, Sebastian Steinlechner, Sichun Sun, Michael E. Tobar, Francisco Torrenti, Caner Ünal, and Graham White. Challenges and opportunities of gravitational-wave searches at mhz to ghz frequencies. *Living Reviews in Relativity*, 24(1), December 2021.

[99] Richard H. Cyburt, Brian D. Fields, Keith A. Olive, and Tsung-Han Yeh. Big bang nucleosynthesis: Present status. *Rev. Mod. Phys.*, 88:015004, Feb 2016.

[100] A. A. Starobinsky. Amplification of waves reflected from a rotating "black hole". *Sov. Phys. JETP*, 37(1):28–32, 1973.

[101] Ya. B. Zel'Dovich. Generation of Waves by a Rotating Body. *Soviet Journal of Experimental and Theoretical Physics Letters*, 14:180, August 1971.

[102] C. W. Misner. Interpretation of gravitational-wave observations. *Phys. Rev. Lett.*, 28:994–997, Apr 1972.

[103] Demetrios Christodoulou. Reversible and irreversible transformations in black-hole physics. *Phys. Rev. Lett.*, 25:1596–1597, Nov 1970.

[104] Asimina Arvanitaki and Sergei Dubovsky. Exploring the string axiverse with precision black hole physics. *Phys. Rev. D*, 83:044026, Feb 2011.

[105] Daiske Yoshida and Jiro Soda. Exploring the string axiverse and parity violation in gravity with gravitational waves. *International Journal of Modern Physics D*, 27(09):1850096, July 2018.

[106] Sichun Sun and Yun-Long Zhang. Fast gravitational wave bursts from axion clumps. *Physical Review D*, 104(10), November 2021.

[107] Tomotada Akutsu, Seiji Kawamura, Atsushi Nishizawa, Koji Arai, Kazuhiro Yamamoto, Daisuke Tatsumi, Shigeo Nagano, Erina Nishida, Takeshi Chiba, Ryuichi Takahashi, Naoshi Sugiyama, Mitsuhiro Fukushima, Toshitaka Yamazaki, and Masa-Katsu Fujimoto. Search for a stochastic background of 100-mhz gravitational waves with laser interferometers. *Phys. Rev. Lett.*, 101:101101, Sep 2008.

[108] K. Ackley et al. Neutron Star Extreme Matter Observatory: A kilohertz-band gravitational-wave detector in the global network. *pasa*, 37:e047, November 2020.

[109] Serge Galliou, Maxim Goryachev, Roger Bourquin, Philippe Abbé, Jean Pierre Aubry, and Michael E. Tobar. Extremely low loss phonon-trapping cryogenic acoustic cavities for future physical experiments. *Scientific Reports*, 3(1), July 2013.

[110] Maxim Goryachev, Daniel L. Creedon, Serge Galliou, and Michael E. Tobar. Observation of rayleigh phonon scattering through excitation of extremely high overtones in low-loss cryogenic acoustic cavities for hybrid quantum systems. *Physical Review Letters*, 111(8), August 2013.

[111] William Campbell, Serge Galliou, Michael E. Tobar, and Maxim Goryachev. Electro-mechanical tuning of high-q bulk acoustic phonon modes at cryogenic temperatures. *Applied Physics Letters*, 122(3), January 2023.

[112] William Campbell and Michael E. Goryachev, Maximand Tobar. The multi-mode acoustic gravitational wave experiment: Mage. *Scientific Reports*, 13(1), 2023.

[113] M. E Gertsenshtein. Wave resonance of light and gravitational waves. *Sov. Phys. JETP, 14:84*, 1962.

[114] D. Boccaletti, V. De Sabbata, P. Fortini, and C. Gualdi. Conversion of photons into gravitons and vice versa in a static electromagnetic field. *Il Nuovo Cimento B (1965-1970)*, 70(129), 1970.

[115] A. Ejlli, D. Ejlli, A. M. Cruise, G. Pisano, and H. Grote. Upper limits on the amplitude of ultra-high-frequency gravitational waves from graviton to photon conversion. *The European Physical Journal C*, 79(12), December 2019.

[116] Asher Berlin, Diego Blas, Raffaele Tito D'Agnolo, Sebastian A. R. Ellis, Roni Harnik, Yonatan Kahn, and Jan Schütte-Engel. Detecting high-frequency gravitational waves with microwave cavities. *Phys. Rev. D*, 105:116011, Jun 2022.

[117] J. Weber. Gravitational radiation. *Phys. Rev. Lett.*, 18:498–501, Mar 1967.

[118] Asher Berlin, Diego Blas, Raffaele Tito D'Agnolo, Sebastian A. R. Ellis, Roni Harnik, Yonatan Kahn, Jan Schütte-Engel, and Michael Wentzel. Mago 2.0: Electromagnetic cavities as mechanical bars for gravitational waves, 2023.

[119] C. B. Adams et al. Axion dark matter, 2023.

[120] Chiara P. Salemi, Joshua W. Foster, Jonathan L. Ouellet, Andrew Gavin, Kaliroë M. W. Pappas, Sabrina Cheng, Kate A. Richardson, Reyco Henning, Yonatan Kahn, Rachel Nguyen, Nicholas L. Rodd, Benjamin R. Safdi, and Lindley Winslow. Search for low-mass axion dark matter with abracadabra-10 cm. *Phys. Rev. Lett.*, 127:081801, Aug 2021.

[121] Dmitry Budker, Peter W. Graham, Micah Ledbetter, Surjeet Rajendran, and Alexander O. Sushkov. Proposal for a cosmic axion spin precession experiment (casper). *Phys. Rev. X*, 4:021030, May 2014.

[122] John Clark and Alex L. Barginski. *The SQUID Handbook Vol. I Fundamentals and Technology of SQUIDsand SQUID Systems*. WILEY-VCH Verlag GmbH & Co, KGaA, 2004.

[123] Joshua W. Foster, Nicholas L. Rodd, and Benjamin R. Safdi. Revealing the dark matter halo with axion direct detection. *Phys. Rev. D*, 97:123006, Jun 2018.

[124] Valerie Domcke, Camilo Garcia-Cely, and Nicholas L. Rodd. Novel search for high-frequency gravitational waves with low-mass axion haloscopes. *Physical Review Letters*, 129(4), July 2022.

[125] Valerie Domcke, Camilo Garcia-Cely, Sung Mook Lee, and Nicholas L. Rodd. Symmetries and selection rules: Optimising axion haloscopes for gravitational wave searches, 2024.

[126] Thomas D. P. Edwards, Kaze W. K. Wong, Kelvin K. H. Lam, Adam Coogan, Daniel Foreman-Mackey, Maximiliano Isi, and Aaron Zimmerman. ripple: Differentiable and hardware-accelerated waveforms for gravitational wave data analysis, 2023.

[127] Sivaram Ambikasaran, Daniel Foreman-Mackey, Leslie Greengard, David W. Hogg, and Michael O'Neil. Fast Direct Methods for Gaussian Processes. *IEEE Transactions on Pattern Analysis and Machine Intelligence*, 38:252, June 2015.

[128] Joshua W. Foster, Marius Kongsore, Christopher Dessert, Yujin Park, Nicholas L. Rodd, Kyle Cranmer, and Benjamin R. Safdi. Deep search for decaying dark matter with xmm-newton blank-sky observations. *Physical Review Letters*, 127(5), July 2021.

[129] Hans Dembinski and Piti Ongmongkolkul et al. scikit-hep/iminuit. Dec 2020.

[130] Nicholas M. Rapidis. Status of dmradio-50l and dmradio-m^3, 2022.

[131] L. Brouwer, S. Chaudhuri, H.-M. Cho, J. Corbin, W. Craddock, C.S. Dawson, A. Droster, J.W. Foster, J.T. Fry, P.W. Graham, R. Henning, K.D. Irwin, F. Kadribasic, Y. Kahn, A. Keller, R. Kolevatov, S. Kuenstner, A.F. Leder, D. Li, J.L. Ouellet, K.M.W. Pappas, A. Phipps, N.M. Rapidis, B.R. Safdi, C.P. Salemi, M. Simanovskaia, J. Singh, E.C. van Assendelft, K. van Bibber, K. Wells, L. Winslow, W.J. Wisniewski, and B.A. Young. Projected sensitivity of dmradio-m3: A search for the qcd axion below 1 uev. *Physical Review D*, 106(10), November 2022.

[132] DMRadio Collaboration, A. AlShirawi, C. Bartram, J. N. Benabou, L. Brouwer, S. Chaudhuri, H. M. Cho, J. Corbin, W. Craddock, A. Droster, J. W. Foster, J. T. Fry, P. W. Graham, R. Henning, K. D. Irwin, F. Kadribasic, Y. Kahn, A. Keller, R. Kolevatov, S. Kuenstner, N. Kurita, A. F. Leder, D. Li, J. L. Ouellet, K. M. W. Pappas, A. Phipps, N. M. Rapidis, B. R. Safdi, C. P. Salemi, M. Simanovskaia, J. Singh, E. C. van Assendelft, K. van Bibber, K. Wells,

L. Winslow, W. J. Wisniewski, and B. A. Young. Electromagnetic modeling and science reach of dmradio-m^3, 2023.

[133] L. Brouwer, S. Chaudhuri, H.-M. Cho, J. Corbin, C.S. Dawson, A. Droster, J.W. Foster, J.T. Fry, P.W. Graham, R. Henning, K.D. Irwin, F. Kadribasic, Y. Kahn, A. Keller, R. Kolevatov, S. Kuenstner, A.F. Leder, D. Li, J.L. Ouellet, K.M.W. Pappas, A. Phipps, N.M. Rapidis, B.R. Safdi, C.P. Salemi, M. Simanovskaia, J. Singh, E.C. van Assendelft, K. van Bibber, K. Wells, L. Winslow, W.J. Wisniewski, and B.A. Young. Proposal for a definitive search for gut-scale qcd axions. *Physical Review D*, 106(11), December 2022.